Doctoral Dissertation

Bottom-up optical three-dimensional nanofabrication of metamaterials

Natsuo Taguchi

December 2017

Graduate School of Engineering

Osaka University

Introduction

The diameters of red blood cells and hairs of human are around 10 μm and 100 μm respectively. With these sizes, about ten blood cells can make a line along the diameter of the hairs. Arbitrary 3D structures with the size of the blood cells can be fabricated with light. When I was an undergraduate, I was majoring electrical and electronic engineering. However, I was interested in state-of-the-art technologies such as nanoscience. The optical fabrication technology was attractive for me enough to change my major. Needless to say, nano/micro fabrication is essential in science and technology at present. Various fabrication methods have been invented: photo/electron-beam/ion-beam lithography, nanoimprinting etc. All of these methods, however, are 2D nano/micro fabrication and limited to surface processing. I have been engaged in 3D nano/micro fabrication in top-down and bottom-up approaches with light during this five years. In this thesis, I summarized a series of research outcomes regarding this theme.

The optical fabrication technology mentioned at the beginning is called as two-photon fabrication (TPF). Two-photon process of materials is the core principle. Lasers with high power are applied to light curing resins, and the resins are cured only at the center of focus spot via two-photon absorption. By scanning the focus spot in 3D, nano/micro structures are fabricated. TPF is, so to speak, a nano/micro version of 3D printer. Arbitrary 3D nano/micro structural fabrication with spatial resolution beyond diffraction limit is realized by TPF. Metals also can be applied as materials of TPF.

TPF has been used in various fields where 3D nano/micro fabrication is needed. Metamaterials are one of the examples. Metamaterials are subwavelength 3D structures mainly made with metals interacting with electromagnetic field of light. Arbitrary control of permittivity, permeability, and refractive index is expected with the metamaterials. Control of electromagnetic wave is incomparably freer than so far by the metamaterials.

However, realization of the metamaterials is not easy. Difficulty in mass fabrication of the 3D structures interacting with light is one of the big problems. Mainstream of metamaterial fabrication is top-down approaches such as photolithography. By artificially fabricating materials toward intended designs, the structures are obtained. TPF also is one of top-down approaches. The top-down approaches are unsuitable for mass fabrication. This is because it takes a long time to fabricate a structure, and the number of the structures per one fabrication period is limited. Even if the metamaterials are prepared with the top-down approaches, the scale of them will be small. Practical application is hence difficult.

How can we prepare such a subwavelength 3D metal structures in bulk? Bottom-up approaches are one of the answers. Not artificially but naturally, the 3D metal structures can be formed by inherent forces of atoms and molecules such as Coulomb force and Van der Waals force. Here, let us imagine snow crystals. There are indeed various shapes in the snow crystals. We can see branches grew from edges of a hexagonal crystal, and additional narrow branches grew from these branches. The whole picture of the snow crystal will represent tree-like shape. However, this complicated geometry is created completely by nature, not by human. Bottom-up approaches easily realize mass creation of such a complicated 3D nano/micro structures.

The problem is how 3D metal structures acting as metamaterials can be made with bottom-up approaches. In this term, I focus on tree-like silver nanostructures; silver nanodendrites. Dendrites are one of the crystals whose shape is like trees with trunks and many branches. Several branches grow from a trunk with a certain gap between two neighboring branches in one dendrites. It is one of the most essential point to act as metamaterials that the silver nanodendrites can have electromagnetic induction with magnetic field. Here, I consider that parts of the dendrites composed by two neighboring branches may act as ring resonators. If these parts can have electromagnetic induction, the nanodendrites may behave as metamaterials. If the trunks and the branches are silver in nanoscale, interaction of the dendrites with electromagnetic wave around visible range may be realized.

Based on the background described above, in this thesis, I aimed my research theme to bottom-up metamaterial fabrication with silver nanostructures. I explain a method of bottom-up optical fabrication of silver nanodendrites. I discuss shape differences of silver nanocrystals among experimental parameters such as temperature and laser power. I also discuss electromagnetic field responses of the silver nanodendrites to evaluate potentials as metamaterials. Finite-difference time-domain method was utilized to analyze the electromagnetic field responses.

In addition, I show elasticity and molecular orientation of polymer 3D nanostructures formed by TPF. Size dependent elasticity of the polymer nanosprings along wire radii was evaluated with spring constants measured by an atomic force microscope. Size dependent molecular orientation of polymer nanowires along wire radii also was evaluated by polarized micro-Raman spectroscopy. I then discuss correlations of the size dependent characteristics between the elasticity and the molecular orientation.

Table of contents

Introduction **1**

Chapter 1. Metamaterials **6**

1.1 Electromagnetic responses of metamaterials 6

1.2 Applications with refractive index control 13

1.3 Top-down and bottom-up fabrications of metamaterials 14

1.4 Silver nanodendrites as metamaterials 16

1.5 Fractal on metamaterials and optics 20

Chapter 2. Optical three-dimensional growth of silver nanodendrites **27**

2.1 Growth of dendritic structure 27

2.2 Plasmonic heating of silver nanoparticles 38

2.3 Nondestructive extraction of silver nanodendrites with supercritical fluid 41

2.4 Parameter optimization for silver nanodendrite growth 45

2.5 Growth of silver nanodendrites in agarose gel 51

2.6 Fractal characteristic of silver nanodendrites 53

2.7 Absorption of silver nanostructures 54

Chapter 3. Finite-difference time-domain analysis **61**

3.1 Scattering spectra of silver nanodendrite model 61

3.2 Magnetic response of silver nanodendrite model 64

3.3 Permittivity, permeability, and refractive index of silver nanodendrite model 66

3.4 Scattering characteristics among geometrical parameters 72

3.5 Scattering and oscillation behaviors with different incident direction 73

Chapter 4. Three-dimensional nanofabrication via two-photon absorption **81**

4.1 Principle of three-dimensional nanofabrication 81

4.2 Spatial resolution beyond diffraction limit 84

4.3 Applications of three-dimensional nanofabrication via two-photon absorption 85

Chapter 5. Three-dimensional polymer nanostructures formed by two-photon polymerization **89**

5.1 Size dependent elasticity of polymer nanosprings 89

5.2 Raman analysis of polymer nanowires 94
5.3 Molecular orientation analysis of polymer nanowires 97

Conclusion **109**

List of publications **112**

Abstract **114**

Acknowledgement **116**

Chapter 1.
Metamaterials

Metamaterials, which are one of trends of science and technology, are artificial materials composed of subwavelength structures interacting both electric and magnetic fields. In this chapter, I briefly introduce the physics, the history, and applications of metamaterials especially as negative refractive index materials. I discuss bottom-up production approaches of the metamaterials. The bottom-up approaches are necessary for the metamaterials to be applied widely. I focus tree-like silver nanocrystals as a bottom-up metamaterial. I discuss fractal which is one of important characteristics of the tree-like silver nanocrystals.

1.1 Electromagnetic responses of metamaterials

The word *metamaterials* was generated to depict artificially designed materials with physical properties not in nature [1,2]. The definition of the metamaterials, however, seems not to have been distinct. On many contexts of not only electromagnetics but also other fields dealing with waves, *metamaterials* have been used. Here, at first in this research, I define *a metamaterial* as *an assembly of intendedly produced subwavelength structures which simultaneously respond with both electric and magnetic fields*.

According to electromagnetics, refractive index n of materials is defined with relative permittivity ε and relative permeability μ as the equation below,

$$n = \sqrt{\varepsilon}\sqrt{\mu}\,. \tag{1.1}$$

These quantities are basically inherent in the materials. If a material does not change to another material, the permittivity, the permeability, and the refractive index of the material then

does not change. This is a premise of electromagnetics established by J. C. Maxwell, and treated as so for a long time.

A movement to arbitrarily control the permittivity, the permeability, and the refractive index was emerged on the latter of 1990s [3,4]. Metal structures with finite size which is about one tenth of wavelength of electromagnetic wave are the key points to control these quantities. In other words, these are the metal structures interacting with electromagnetic field. This is the dawn of metamaterials. At present, over 2000 papers regarding metamaterials have been published per year. The field of metamaterials has been one of trends of science and technology.

If the metal structures are satisfyingly smaller than the wavelength of electromagnetic wave, these metal structures can be the same as atoms and molecules for the electromagnetic wave. That is to say, the electromagnetic wave does not diffract and scatter with the metal structures. If there are a number of such subwavelength metal structures in a system, the effective permittivity and the effective permeability which are derived from interactions between the metal structures and the electromagnetic wave will appear.

Then, what kind of the structures does it which can interact with electromagnetic wave? For electric field, the metals can easily react with their free electrons. The shape of the structures can be simple rods as shown in upper left of Fig. 1.1. The effective permittivity $\varepsilon_{\mathrm{eff}}$ derived from the rods still obeys the Drude model as follow,

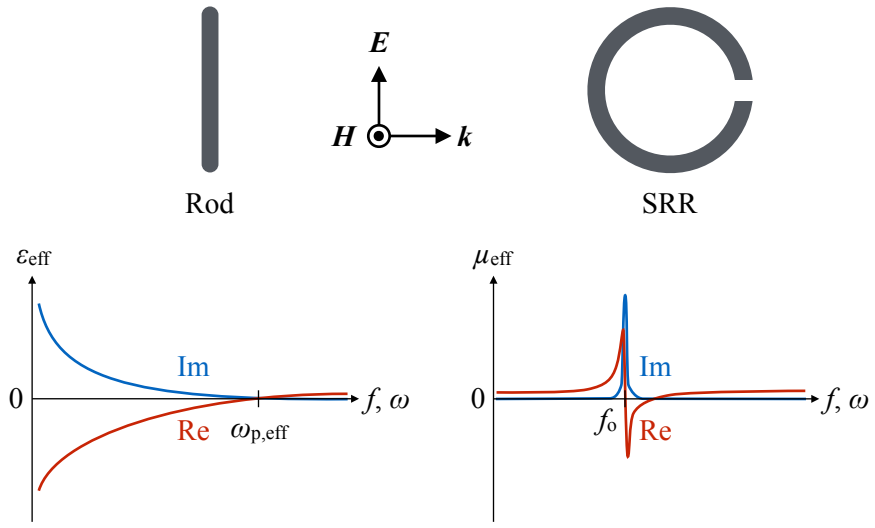

Figure 1.1| Schematics of a metal rod and an SRR which interact with electric and magnetic fields respectively. Effective permittivity and permeability vary along the frequency due to interactions of the rod and the SRR.

$$\varepsilon_{\mathrm{eff}}(\omega) = 1 - \frac{{\omega_{\mathrm{p,eff}}}^2}{\omega^2 + i\Gamma_{\mathrm{eff}}\omega}, \tag{1.2}$$

where ω, $\omega_{\mathrm{p,eff}}$, and Γ_{eff} are angular frequency of the electromagnetic wave, effective plasma frequency, and effective dumping coefficient of the metals [5]. The frequency characteristics of the permittivity $\varepsilon_{\mathrm{eff}}$ is shown in lower left of Fig. 1.1. An effect of interband transition needs to be considered around optical frequency region. Hence, the actual permittivity is the sum of the permittivity from Drude model and the one from interband transition. In contrast, interaction with magnetic field requires a contrive; structures which can have electromagnetic induction can realize the interaction. Actually, this is the charm of the metamaterials. Split ring resonators (SRRs) as described in upper right of Fig. 1.1, which are ring structures with a cut, are the most basic example. The SRRs can have a coil on the ring part and a capacitor at the cut. The SRRs thus can behave as an LC resonance circuit. The LC circuit has the resonant frequency f_{o} determined by the inductance L and the capacitance C,

$$f_{\mathrm{o}} = \frac{1}{2\pi\sqrt{LC}}. \tag{1.3}$$

The electromagnetic wave of the resonant frequency is absorbed by the SRRs. This phenomenon corresponds to change of the magnitude on the imaginary part of the effective permeability around the resonant frequency. The real part and the imaginary part of the permeability (and the permittivity) relate with each other by Kramers-Kronig relation [6]. Hence, the real part also changes when the imaginary part changes as shown in lower right of Fig. 1.1. By utilizing the rods and SRRs of the metals, the effective permittivity and the effective permeability can be controlled.

Negative refractive index

On the frequency region slightly above the resonance, the real part of the permeability largely changes. If the resonance has high Q factor, the amount of change on the real part of the permeability will also be large. Consequently, negative real part of the permeability can be available. If both the permittivity and the permeability are negative, the refractive index also is negative. The negative refractive index is the most typical property to characterize the metamaterials.

In the negative refractive index materials (NIMs), the electromagnetic wave shows strange behavior. Here, let us assume a plane electromagnetic wave $\boldsymbol{E}$ and $\boldsymbol{H}$ in a vacuum. The wavenumber k can be written as dispersion relation as follows,

$$k^2 = \frac{\omega^2}{c^2} n^2 = \frac{\omega^2}{c^2} \varepsilon \mu \,, \tag{1.4}$$

where c is the speed of light. When the refractive index is negative, then the wavenumber is also negative. On the other hand, the energy direction of the electromagnetic wave corresponds to poynting vector $\boldsymbol{S}$

$$\boldsymbol{S} = \boldsymbol{E} \times \boldsymbol{H} \,. \tag{1.5}$$

Therefore, the wavenumber and the energy of the electromagnetic wave are opposite with each other in the NIMs. When the electromagnetic wave incident onto the NIMs, the wave refracts to a direction which is different compared to positive refractive index materials a s described in Fig. 1.2. The direction of refraction is determined by the interface condition of electromagnetic wave between the vacuum and the NIMs, namely the conservation of the wavevector.

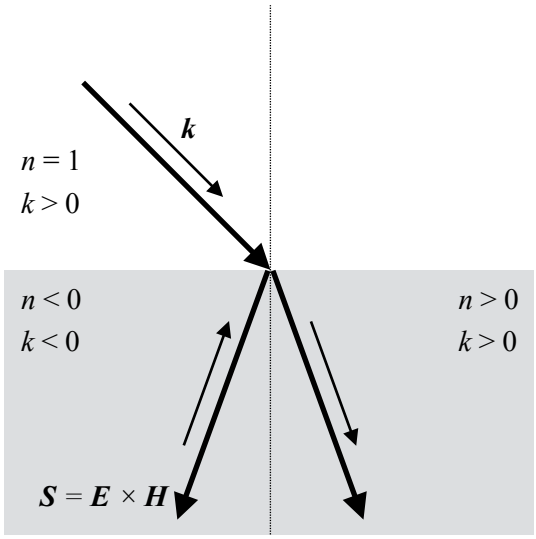

Figure 1.2| Directions of refraction, Poynting vector, and wavevector among positive and negative refractive index materials.

Any materials in nature are categorized in four areas by taking the permittivity and permeability x and y axes respectively as shown in Fig. 1.3 [7]. Materials with both positive permittivity and permeability like dielectrics are located on the first quadrant. The permeability of the materials in optical region is regarded as unity. Materials with negative permittivity and positive permeability in optical and other wide frequency regions such as metals are located on the second quadrant. Materials with positive permittivity and negative permeability like diamagnetic are located on the forth quadrant. The NIMs with both negative permittivity and permeability are then located on the third quadrant. It should be noted that the electromagnetic wave cannot penetrate the material of the second and the fourth quadrants. This is because the wavevector in these materials is imaginary, which means the electromagnetic wave exists as evanescent wave. In contrast, the electromagnetic wave can penetrate in the materials of the first and third quadrants as the wavevector is real. Then, the electromagnetic wave propagates to backward in the NIMs as the wavevector is negative. However, the NIMs have never been discovered in nature yet.

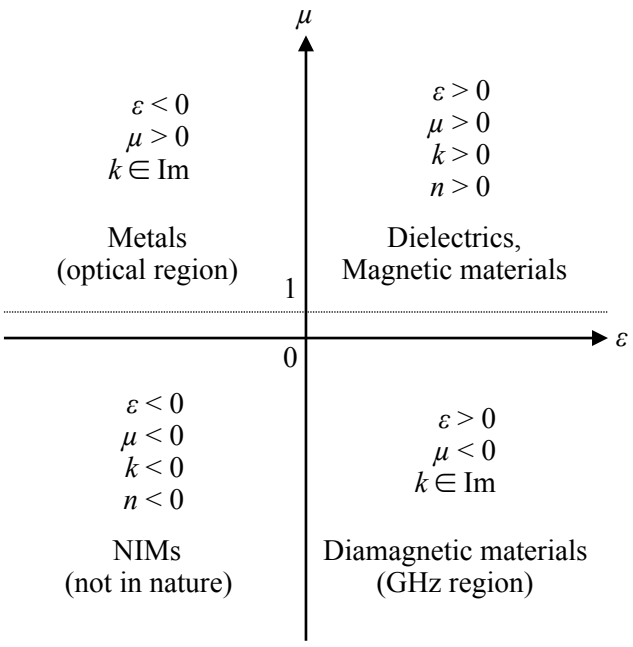

Figure 1.3| A classification of natural materials with the value of permittivity and permeability.

Optimization to high frequency region

Actually, Veselago first considered the physics of the NIMs in 1960s [8]. Although he looked for existence of the NIMs in nature, he could not find the NIMs. After that, his work had been left behind until around 2000s. Pendry got an idea to control the permittivity and the permeability with periodic alignment of the metal rods and SRRs. He then theoretically proved that the negative index can be available with the system around the latter of 1990s [3,4]. Based on a series of his works, Smith and coworkers experimentally realized the metamaterials as NIMs with the same system (rods and SRRs) on microwave region at the first of 2000s [9,10]. Since there are huge attractions for control of the refractive index, as I describe in the next section, researches regarding the metamaterials were immediately accelerated.

Pendry and Smith's works were achieved in microwave region. Then, a competition to make the metamaterials on higher frequency region than microwave was emerged [11]. Optimizing the metamaterials to the high frequency corresponds to simplification and miniaturization of the unit structures. Tanaka and coworkers studied possibilities of permeability control in optical region [12]. They considered a system with a periodic series of a nanosize silver SRR with multiple splits as shown in Fig. 1.4 (a). They theoretically confirmed that the system can realize negative permeability between optical region to ultra violet (Fig. 1.4

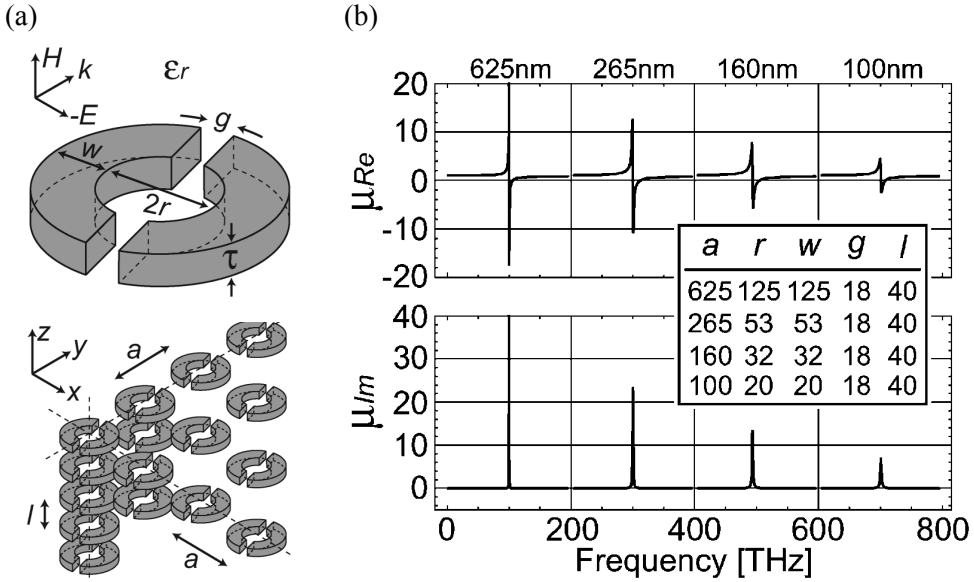

Figure 1.4| (a) A schematic and a configuration of a miniaturized SRR with multiple splits optimized for around optical region, and (b) magnetic resonances at different wavelengths among the dimensional differences. Figure referred from [12].

(b)). In addition, there are many theoretical and experimental studies for high frequency optimization as summarized in Fig. 1.5. Shalaev and coworkers developed gold nanorod pairs as an abstract of the SRRs as described in lower left of Fig. 1.5, and theoretically and experimentally confirmed negative refractive index around near infrared region [13-15]. Zhang and coworkers developed fishnet structures which can make both the permittivity and permeability negative as shown in lower right of Fig. 1.5 [16-20]. As far as I know, the fishnet geometries have been the most successful for the metamaterials as the NIMs around optical region.

Recent trends of the metamaterials are entirely on a context of surface engineering. Many nanostructures which interact with the electromagnetic wave have been developed. The surface nanostructures are so-called metasurfaces [21]. The functions of the metasurfaces have been diverged from refractive index control: chiral engineering [22,23], Fano resonance [24-26], electromagnetic induced transparency [27,28] etc.

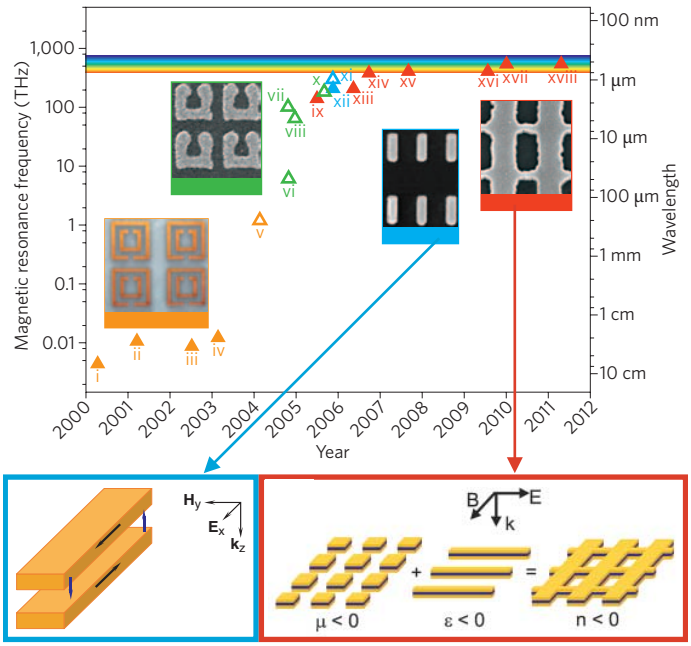

Figure 1.5| Transitions of SRR structures along the year toward high frequency region. A metal rod pair and a fishnet model are indicated by blue and red respectively. Figure referred from [11,14,20].

1.2 Applications with refractive index control

Arbitral control of permittivity, permeability, and refractive index realizes freer control of electromagnetic wave than ever. Here, let us assume a NIM with the value -1 of the permittivity and the permeability in a vacuum. The refractive index is also -1. In this case, the electromagnetic wave from a point light source has a pass as shown in Fig. 1.6 (a). The electromagnetic wave from the point source is focused again after penetrating the NIM. Hence, a plane lens is realized by the NIMs. The impedance of the NIM is the same as that of the vacuum. Hence, there is no reflection at the interface between the NIM and the vacuum. The important is evanescent wave is enhanced in the NIM [29]. When the electromagnetic wave hit to objects, scattered wave and transmitted wave which reflect information such as the structures of the objects are generated. The evanescent wave is also generated with these electromagnetic waves as propagating wave. The evanescent wave has larger wavevector than the propagating wave. This means the evanescent wave have more finite information than the propagating wave. On the other hand, the amplitude of the evanescent wave decay exponentially, making propagation of the evanescent wave difficult. Hence, the resolution of images is basically limited to the magnitude of the wavelength of the incident electromagnetic wave. If the evanescent wave is able to propagate, infinitely small objects such as atoms and

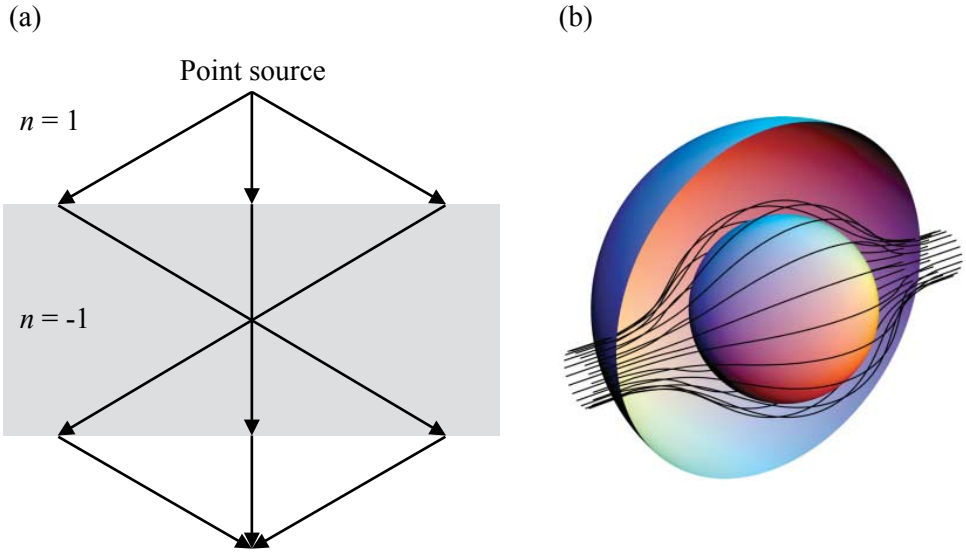

Figure 1.6| (a) A NIM refracts electromagnetic wave from a point source with different manner compared to positive refractive index materials, making transmitted wave refocus. (b) Electromagnetic wave indicated by black line circumvents something at the center due to distribution of refractive index around it. Figures referred from [29,30].

molecules can be imaged. Such a perfect lens can be realized when the refractive index of the NIMs is -1.

Active camouflage is also realized by the metamaterials [30,31]. If we are able to arbitrarily make a distribution of refractive index in a space, this means we are able to arbitrarily control the pass of the electromagnetic wave. If an object is surrounded by the refractive index distribution and the electromagnetic wave circumvents the object, there is no scattered and transmitted wave from the object as shown in Fig. 1.6 (b). We are thus not able to detect the object, realizing cloaking.

There can be also a number of other applications of the refractive index control. The metamaterials have potentials to evolve science and technology.

1.3 Top-down and bottom-up fabrications of metamaterials

Metamaterials have been successfully fabricated via top-down approaches: light-beam lithography, electron-beam lithography, laser direct writing via two-photon process [32,33] etc. By artificially fabricating materials toward intended designs, the structures are obtained by the top-down approaches. Indeed, the intended structures can easily be made by the top-down approaches. However, mass fabrication and 3D structure fabrication are difficult with the top-down approaches. Hence, applications of the metamaterials as described in the last section have still been hard to be realized. This is because 3D bulks with numerous structures interacting with electromagnetic wave.

Bottom-up approaches such as crystal growth and self-assembly of atoms or molecules are the contrast to the top-down approaches. Not artificially but naturally, the 3D structures are formed by the bottom-up approaches. The 3D structures are formed by inherent forces of atoms or molecules such as intermolecular force Coulomb force. The bottom-up approaches realize mass production of finite and complicated 3D structures at once, which is at present impossible by the top-down approaches. On the other hand, duplication of the same structures is more difficult with the bottom-up approaches than with the top-down approaches. We are forced to indirectly control the geometry of the structures via several parameters: temperature, concentration, time etc.

There are some works of bottom-up metamaterial production [34,35]. Fan *et al.* considered a core-shell nanoparticle with gold and silica [36]. Each silica shell behaves as a spacer, making capacitors between the nanoparticles (Fig. 1.7 (a)). They theoretically and experimentally confirmed that a trimer of the gold-silica core-shell nanoparticles had a magnetic dipole with an incident light polarized in the plane of the trimer as shown in Fig. 1.7 (b). Metal film-dielectric layer-metal nanoparticle systems may also act as the metamaterials [37,38]. A magnetic response can occur between the film and the nanoparticle with the dielectric layer as a spacer as shown in Fig. 1.8 (a). This system can also react with electric field with the film and the nanoparticle. Hence, this system shows absorptions due to simultaneous responses of electric and magnetic fields (Fig. 1.8 (b)). It was reported that a core-shell cluster which consist of a dielectric core sphere decorated by a number of gold nanoparticles forming a shell could also act as a metamaterial [39-41]. By illuminating this core-shell cluster by a plane wave, all the nanoparticles at the shell oscillate in-phase around the core sphere in a particular frequency, causing an effective current. This system has a large permittivity due to permittivity dispersion of dielectrics near plasmon resonance of the nanoparticles. At the high

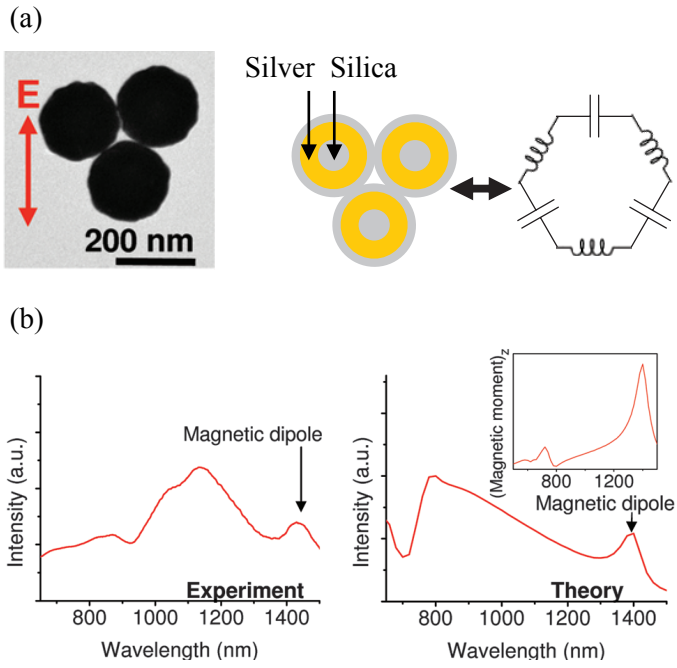

Figure 1.7| (a) A trimer of core-shell nanoparticles with silver and silica and corresponding equivalent resonant circuit. (b) Experimental and theoretical scattering spectra of the trimer. A magnetic dipole is indicated. Figure referred from [36].

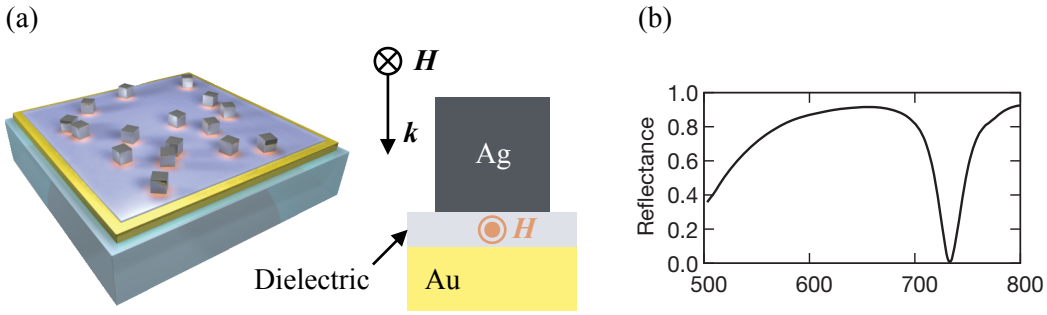

Figure 1.8| (a) Silver nanocubes dispersed on a gold film with a dielectric spacer. This system can have a magnetic resonance between the nanocubes and the film. (b) A calculated reflection spectrum for cubes that are 70 nm in size, distributed with periodicity (350 nm) and separated from the gold film by an 8 nm thick dielectric layer. Figure referred from [37].

permittivity area, the 1st order Mie resonance which has a magnetic dipole can be excited. Control of permittivity and permeability using Mie resonance inside dielectric structures has been reported recently [42,43]. Use of nanostructures existing in nature as metamaterials also is interesting. Ebihara *et al.* reported that a lotus leaf coated with gold film showed reflectance near zero on optical frequency [44]. This characteristic originates from complicated nanostructure at the surface the leaf coated with gold, where light is confined and hardly emitted.

1.4 Silver nanodendrites as metamaterials

There is a kind of crystal shapes called *dendrites*. The dendrites are tree like silver crystals made of orderly assembled numerous branches. Such complicated structures are self-grown, and formed with every material including metals. Then, the shape of the dendrites varies diversely by conditions of crystal growth. Snowflakes are one of the most familiar examples of the dendrites (Fig. 1.9 (a)) [45]. It can be clearly observed that a number of snow crystals with various shapes and sizes are bound up in order and form tree like shapes around apexes of the snowflakes. Moreover, snowflakes with the same shape never exist in nature. This is because the shape of the snowflakes is determined by parameters of the air such as temperature and humidity which change constantly, and the same condition never happen in the past and the future. “Snowflakes are letters sent from heaven.” Ukichiro Nakaya, who made the first artificial snowflakes, expressed diversity of snowflake growth as so [46].

Fractal also is an intrinsic and important characteristic of the dendrites. Fractal is a concept of mathematics and integrates everything which has self-similarity between part and whole of it. Benoît B. Mandelbrot gave rise to fractal in the middle of 1970s [47]. Nowadays, fractal has become popular and is used in various fields and situations. Everywhere of nature, fractal emerges: lightning, patterns of river network, cloud etc. Based on the law of self-similarity even in randomness, those patterns are created. The dendrites are also formed by repeated ramification of branches begun from trunks. Parts and the whole of the dendrite can

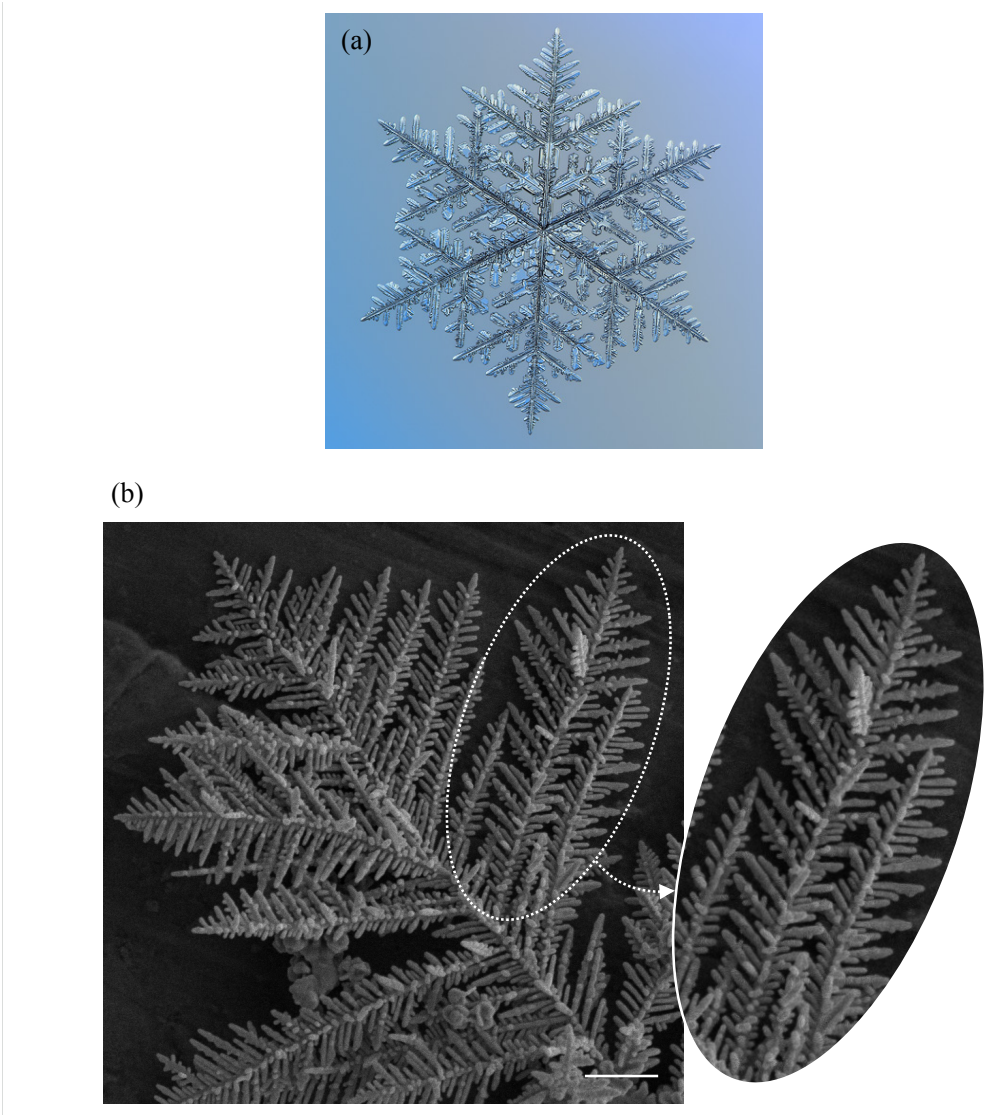

Figure 1.9| Dendrites with fractal (self-similarity). (a) A snowflake. (b) A silver nanodendrite grown on a glass substrate. The right-side image is a magnification of the dotted area on the left-side image. The scale bar is 1 μm. Figure (a) referred from [45].

be found as self-similarity with each other. The detail of fractal is described in the next section of this chapter.

In nanoscale, moreover, the dendrites exist. From here, I call such nanosize dendritic structures as *nanodendrites*. The nanodendrites consist of numerous nanosize branches, and configure fractal geometries in nanoscale. Here, nanodendrites of silver are shown in Fig. 1.9 (b). Such silver nanodendrites show optical properties in wide areas of visible region. This is because the silver nanocrystals have plasmon resonance in the visible range and the resonance frequency vary with the size and the shape of the nanocrystals. The detail appears in section 2.5 of the next chapter.

The silver nanodendrite may be utilized as metamaterials. Zhao and coworkers have tried to utilize dendritic structures as the metamaterials [48-55]. They confirmed that a metal dendritic structure with millimeter scale as shown in Fig. 1.10 (a) could interact with both electric and magnetic fields. Trunks of the dendritic structure could interact with the electric field (Fig. 1.10 (b)), and loops between adjacent branches could interact with the magnetic field (Fig. 1.10 (c)). A Refractive index calculation indicated that an optimized dendritic

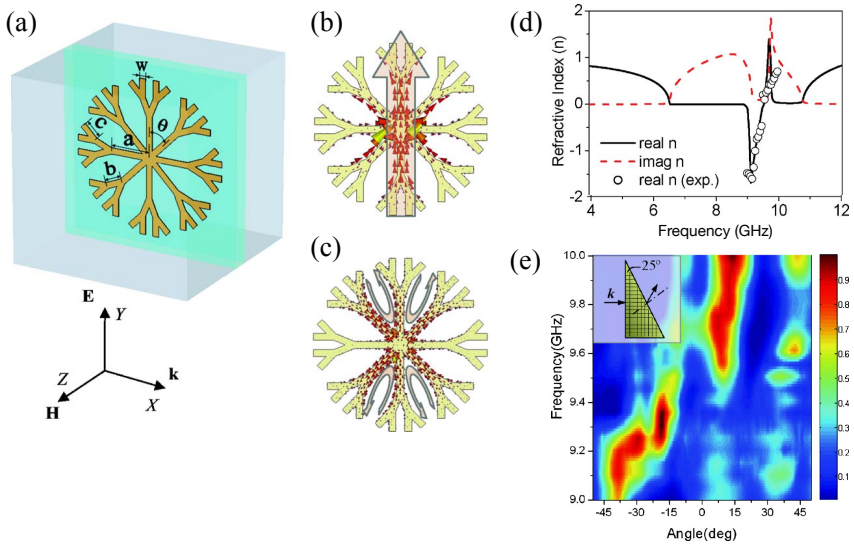

Figure 1.10| (a) A metal dendritic structure model with geometry parameters. The structure can interact with electric and magnetic fields as shown in (b) and (c) respectively. Small red arrows indicate current direction induced by the electromagnetic field. (d) An optimized structure can have negative refractive index around 9.3 GHz. (e) A prism made with periodic arrangement of the optimized structure has negative refraction around 9.3 GHz. Figure referred from [53].

structure could have negative refractive index around 9.3 GHz as shown in Fig. 1.10 (d). They also made a prism with periodic arrangement of the metal dendritic structures. Then, they experimentally confirmed that the prism had a negative refraction of an incident wave around 9.3 GHz as shown in Fig. 1.10 (e). They have also made a fishnet metamaterial with silver nanodendrites. They grew the nanodendrites on conductive glass substrates, and made a sandwich-like structure of them with polyvinyl alcohol (PVA) layers as spacer as shown in Fig. 1.11 (a). A transmission spectrum of the sandwich-like structure showed several peaks (Fig. 1. 11 (b)). Since the nanodendrites were fractal, multiple transmissions can be allowed. They conducted a point source focusing experiment of the sandwich-like structure with wavelengths corresponding to the peaks as described in Fig. 1.11 (c). The point source was set normal to the sandwich-like structure, and transmitted light was collected with an acceptor set normal to the sandwich-like structure. They have given a result that the transmitted light with the wavelength corresponding to the peaks of the transmission spectrum focused again as shown in Fig. 1.11 (d). In contrast, the transmitted light with the other wavelength out of

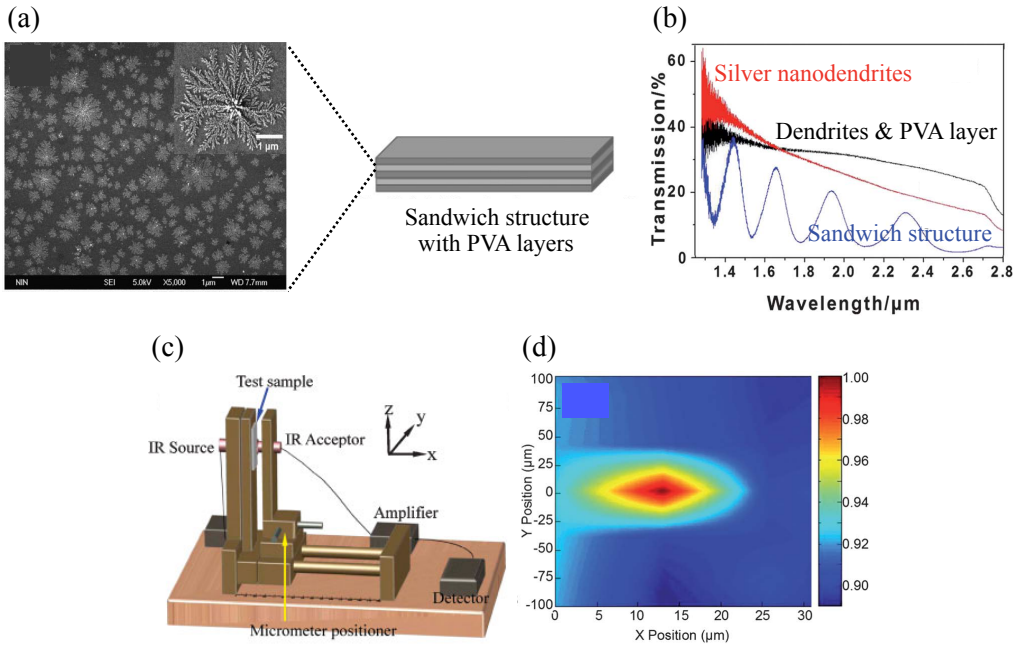

Figure 1.11| (a) Silver nanodendrites grew on a conductive glass substrate, and a sandwich structure of the nanodendrites with PVA layers as spacers. (b) Transmission spectra of the silver nanodendrites, the nanodendrites with a PVA layer, and a sandwich structure. (c) The setup for point source focusing experiment. (d) An intensity distribution of transmitted electromagnetic wave detected by the IR acceptor along an $x-y$ plane of (c). The transmitted wave refocuses. Figure referred from [48,51,52].

the transmission peaks did not focus. This result indicated that the sandwich-like structure acted as a NIM at the wavelength corresponding to the transmission peaks. If their studies are correct, the silver nanodendrites can be utilized for bottom-up making of the metamaterials.

Since the silver nanodendrites are fractal, the silver nanodendrites have also recently been studied as substrates surface enhanced Raman spectroscopy (SERS) [56-61]. The nanodendrites possess a large surface area which is one of characteristics of fractal, allowing themselves to absorb an amount of probe molecules for SERS. The silver nanodendrites also possess a number of neighboring parts, thus exerting a high electric field enhancement due to plasmon coupling between the neighboring parts [62,63].

In view of these backgrounds, I aim to fabricate a bottom-up 3D metamaterial with silver nanodendrites. I anticipate that parts composed of adjacent branches of the nanodendrites act as SRRs. Because of the geometry of the silver nanodendrite, the metamaterial with the nanodendrites have potential for operating in multiple and wide frequency areas around optical region. The silver nanodendrites approaches two important problems of the metamaterials: mass production and broadband operation.

1.5 Fractal on metamaterials and optics

When you see a coast in a map and expand an area of the coast, one will find that the shape of the coast in the expanded area is similar to the shape of the original one. When you buy a bunch of broccoli, pluck a part of that and compare the part and the origin, one will find that the shape of the part is similar to the origin. These shapes look like random at a glance. However, one may not be able to distinguish the shape of the part from the origin because they are close with each other. This means that these shapes actually have common regularities. The world of nature is full of such a structure which consists of parts similar to the whole: a pattern of river network, lightning, crack of the earth, tree, cloud, etc. Nowadays such a characteristic is called as self-similarity [47,64].

Mandelbrot recognized that many patterns in nature (not only in nature, but in price fluctuations of the market) had self-similarity on early stage of his life. He had claimed that simple and beautiful self-similarity often existed in patterns which seemed to be random and ordinary at a glance. In the middle of 1970s, he advocated the new concept *fractal* and described the patterns which had self-similarity uniformly. The etymology of fractal is said to be a Latin word *fractus* which is similar to *fraction* or *fracture*.

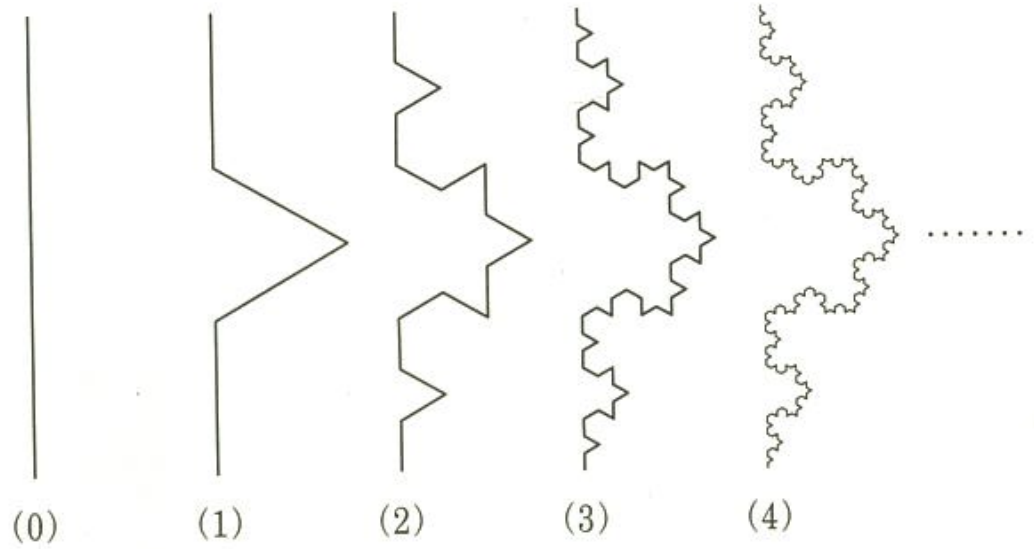

Figure 1.12| Koch curve. The number on the bottom of each curve describes each level. Figure referred from [47].

Here I introduce a simple example of fractal structures: it is called Koch curve (Fig. 1.12). The Koch curve was invented by a Swedish mathematician Helge von Koch on the beginning of twenty centuries. In every level, one can divide each line segment of the former level into three segments of equal length, and replace the middle segment with an equilateral triangle that has the middle segment as its base. By removing the line segment that is the base of the triangle, the Koch curve is finally created. Here, the length of the line segment on 0th level is defined as 1. Hence the total length of the line segments on 1st level is 4/3. Similarly, the total length of those on second level is 16/9 (= $(4/3)^2$). Namely, the length of each line segment becomes 1/3 of that of the former level and the number of line segments is also four times more than the former level. The length of total line segment on nth level is $(4/3)^n$. When n goes to infinity, the total length is also infinity. Namely, the Koch curve is such a mysterious curve which does not have length. This is one of big features of fractal that characteristic length cannot be defined, so the Koch curve is not defined as one dimension. Therefore, fractal dimension described in the next subsection is employed to understand density and complexity of such a fractal structure.

Fractal dimension

Here a line segment with length L is defined. When one measures this line segment with a ruler of length ε and the length of the line segment becomes L', the relation between L and L' is described as below

$$L' = \frac{L}{\varepsilon}. \tag{1.6}$$

Similarly, cases of the area of a square A and the volume of a cube V can also be defined as below

$$A' = \frac{A}{\varepsilon^2}, \quad V' = \frac{V}{\varepsilon^3}. \tag{1.7}$$

Note that the dimension of the patterns is appeared on the exponent of ε. If the ruler ε is tiny enough, the Eqs. (1.6) and (1.7) can always be executed.

Actually, the quantities (length, area, volume, etc.) of every fractal structures can also be evaluated with the tiny ruler even if the fractal structures are extremely dense. Here one measures the quantity V_d of a pattern in dth dimension with a ruler ε. If the quantity V_d transforms to V_d' following the next equation

$$V_d' = \frac{V_d}{\varepsilon^{D_f}}, \tag{1.8}$$

the constant D_f is defined as below

$$D_f = \frac{\log \frac{V_d'}{V_d}}{\log \frac{1}{\varepsilon}}. \tag{1.9}$$

This constant D_f is defined as *fractal dimension*. This is also the generalized definition of dimension itself. In the case of the Koch curve shown in the previous section, the fractal dimension is calculated as below

$$D_f = \frac{\log \frac{4^3}{4^2}}{\log \frac{1}{1/3}} = 1.26\cdots. \tag{1.10}$$

Broadband optical characteristics due to fractal

Fractal has been used to metamaterials. A fractal structure contains multiple self-similar structures with various sizes smaller than itself. If the size of the self-similar structures is subwavelength, the fractal structure interacts with various wavelengths of light. Narrow operating range is one of the big problems of metamaterials other than fabrication. An SRR basically interacts only with single wavelength light. Fractal structures have potential to solve the problem of narrow range operation. As a fractal metamaterial, an "H"-shaped fractal structure was reported [65]. The structure is shown in Fig. 1.13. Figure 1.13 also shows spectra of absorption and phase shift obtained by terahertz time-domain spectroscopy. Plane pulse wave was induced with the direction normal to $x-y$ plane of the structure. There are multiple stop bands and corresponding phase shifts, which originates in fractal. Other fractal structures, such as Cayley tree structure and Sierpinski structure, have also been reported showing multi and broad frequency operation [66,67].

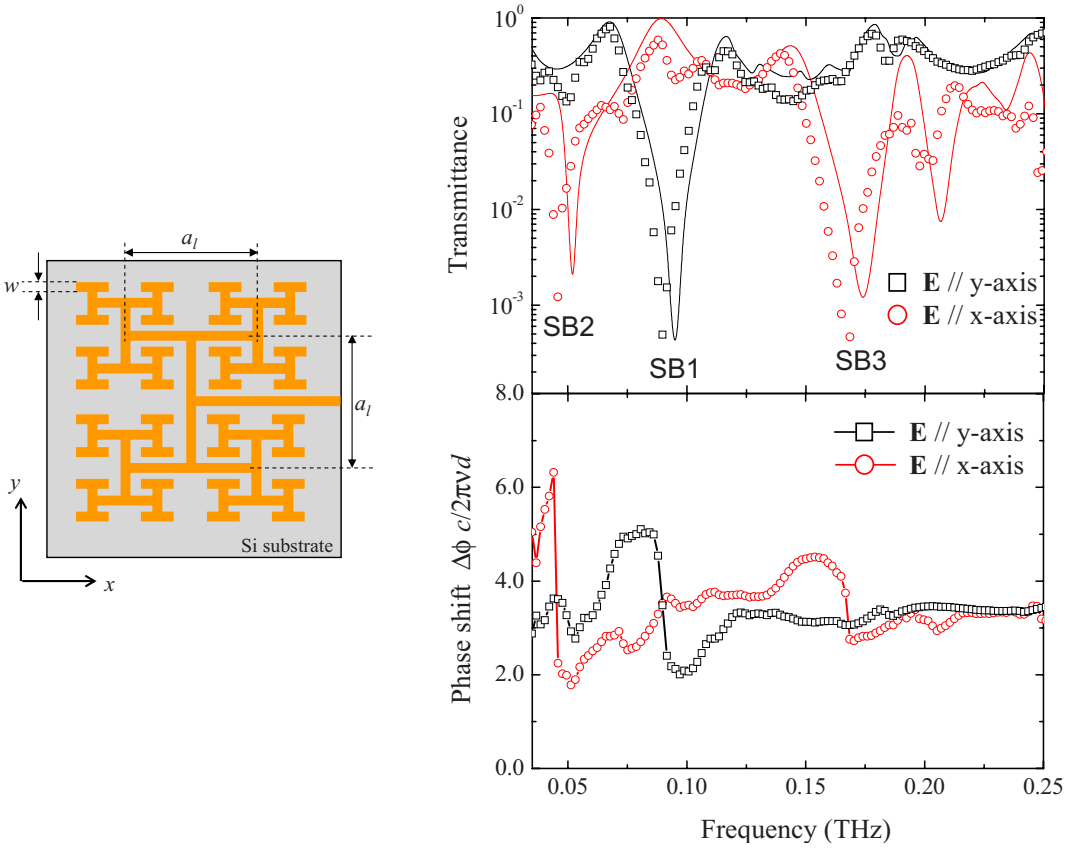

Figure 1.13| Schematic of fractal metal structure (left), and obtained transmittance and phase shift (right) by terahertz time-domain spectroscopy. Multi absorption dips originated from the fractal geometry are observed in the transmission spectra. Figure referred from [65].

Summary

In this chapter, I first defined *metamaterials* and explained fundamentals. With metal rods and SRRs with subwavelength sizes, one can control permittivity, permeability, and refractive index. Negative refractive index is also available. By simplification and miniaturization of unit size of the metamaterial, optimization to high frequency region is achievable. A perfect lens, cloaking, and many other applications are considerable by the metamaterials. Bottom-up productions of the metamaterials are important. This is because a number of units of the metamaterials are needed for the application, and top-down approaches is hard to realize the mass production. Silver nanodendrites, which consist of numerous nanosize branches and configure fractal geometries in nanoscale, may act as a metamaterial. Adjacent branches of the nanodendrites may behave as SRRs. If the silver nanodendrites can be a metamaterial, the nanodendrites approaches two important problems of the metamaterials: mass production and broadband operation.

References

[1] T. J. Cui, R. Liu, and D. R. Smith, editors, *Metamaterials* (Springer, Berlin, 2010).
[2] T. Ishihara, editor, *Technology and Applications of Metamaterial* (CMC Publishing, Tokyo, 2011).
[3] J. B. Pendry, A. J. Holden, D. J. Robbins, and W. J. Stewart, IEEE Trans. Microwave Theory Techn. **47**, 2075 (1999).
[4] J. B. Pendry, A. J. Holden, W. J. Stewart, and I. Youngs, Phys. Rev. Lett. **76**, 4773 (1996).
[5] T. Okamoto and K. Kajikawa, *Plasmonics* (Kodansha, Tokyo, 2010).
[6] 櫛田孝司, 光物性物理学 (朝倉書店, 東京, 2009), pp. 21–51.
[7] A. Ishikawa, Plasmonic Metamaterials and Their Magnetic Properties, 2006.
[8] V. G. Veselago, Sov. Phys. Usp. **10**, 509 (1968).
[9] R. A. Shelby, D. R. Smith, S. C. Nemat-Nasser, and S. Schultz, Appl. Phys. Lett. **78**, 489 (2001).
[10] D. R. Smith, W. J. Padilla, D. C. Vier, S. C. Nemat-Nasser, and S. Schultz, Phys. Rev. Lett. **84**, 4184 (2000).
[11] C. M. Soukoulis and M. Wegener, Nature Photonics (2011).
[12] A. Ishikawa, T. Tanaka, and S. Kawata, Phys. Rev. Lett. **95**, 237401 (2005).
[13] V. P. Drachev, W. Cai, U. Chettiar, H.-K. Yuan, A. K. Sarychev, A. V. Kildishev, G. Klimeck, and V. M. Shalaev, Laser Phys. Lett. **3**, 49 (2013).
[14] V. M. Shalaev, W. S. Cai, U. K. Chettiar, H.-K. Yuan, A. K. Sarychev, V. P. Drachev, and A. V. Kildishev, Opt. Lett. **30**, 3356 (2005).
[15] V. A. Podolskiy, A. K. Sarychev, and V. M. Shalaev, J. Nonlinear Opt. Phys. & Mat. **11**, 65 (2002).
[16] J. G. Valentine, S. Zhang, T. Zentgraf, E. Ulin-Avila, D. A. Genov, G. Bartal, and X. Zhang, Nature **455**, 376 (2008).

[17] S. Zhang, W. Fan, N. C. Panoiu, K. J. Malloy, R. M. Osgood, and S. R. J. Brueck, Phys. Rev. Lett. **95**, 137404 (2005).
[18] S. Zhang, W. Fan, B. K. Minhas, A. Frauenglass, K. J. Malloy, and S. R. J. Brueck, Phys. Rev. Lett. **94**, 509 (2005).
[19] S. Zhang, W. Fan, K. J. Malloy, S. R. J. Brueck, N. C. Panoiu, and R. M. Osgood, Opt. Express **13**, 4922 (2005).
[20] G. Dolling, C. Enkrich, M. Wegener, C. M. Soukoulis, and S. Linden, Science **312**, 892 (2006).
[21] A. V. Kildishev, A. Boltasseva, and V. M. Shalaev, Science **339**, (2013).
[22] Y. Liu and X. Zhang, Chem. Soc. Rev. **40**, 2494 (2011).
[23] J. K. Gansel, M. Thiel, M. S. Rill, M. Decker, K. Bade, V. Saile, G. von Freymann, S. Linden, and M. Wegener, Science **325**, 1513 (2009).
[24] V. Giannini, Y. Francescato, H. Amrania, C. C. Phillips, and S. A. Maier, Nano Lett. **11**, 2835 (2011).
[25] B. luk'yanchuk, N. I. Zheludev, S. A. Maier, N. J. Halas, P. Nordlander, H. Giessen, and C. T. Chong, Nat Mater **9**, 707 (2010).
[26] N. Verellen, Y. Sonnefraud, H. Sobhani, F. Hao, V. V. Moshchalkov, P. V. Dorpe, P. Nordlander, and S. A. Maier, Nano Lett. **9**, 1663 (2009).
[27] S. Biswas, J. Duan, D. Nepal, K. Park, R. Pachter, and R. A. Vaia, Nano Lett. **13**, 6287 (2013).
[28] N. Papasimakis, V. A. Fedotov, N. I. Zheludev, and S. L. Prosvirnin, Phys. Rev. Lett. **101**, (2008).
[29] J. B. Pendry, Phys. Rev. Lett. **85**, 3966 (2000).
[30] J. B. Pendry, D. Schurig, and D. R. Smith, Science **312**, 1780 (2006).
[31] W. Cai, U. K. Chettiar, A. V. Kildishev, and V. M. Shalaev, Nature Photonics **1**, 224 (2007).
[32] T. Tanaka, J. Laser Micro Nanoen. **3**, 152 (2008).
[33] A. Ishikawa and T. Tanaka, IEEE J. Select. Topics Quantum Electron. **19**, (2013).
[34] S. Yang, X. Ni, X. Yin, B. Kante, P. Zhang, J. Zhu, Y. Wang, and X. Zhang, Nature Nanotech **9**, 1002 (2014).
[35] D. A. Pawlak, S. Turczynski, M. Gajc, K. Kolodziejak, R. Diduszko, K. Rozniatowski, J. Smalc, and I. Vendik, Adv. Funct. Mater. **20**, 1116 (2010).
[36] J. A. Fan, C. Wu, K. Bao, J. Bao, R. Bardhan, N. J. Halas, V. N. Manoharan, P. Nordlander, G. Shvets, and F. Capasso, Science **328**, 1135 (2010).
[37] A. Moreau, C. Ciracì, J. J. Mock, R. T. Hill, Q. Wang, B. J. Wiley, A. Chilkoti, and D. R. Smith, Nature **492**, 86 (2012).
[38] M. J. Rozin, D. A. Rosen, T. J. Dill, and A. R. Tao, Nature Communications **6**, 7325 (2015).
[39] M. Fruhnert, S. Muehlig, F. Lederer, and C. Rockstuhl, Phys. Rev. B **89**, (2014).
[40] S. Mühlig, A. Cunningham, J. Dintinger, T. Scharf, T. Bürgi, F. Lederer, and C. Rockstuhl, Nanophotonics **2**, 1 (2013).
[41] J. Dintinger, S. Muehlig, C. Rockstuhl, and T. Scharf, Opt. Mater. Express **2**, 269 (2012).
[42] A. I. Kuznetsov, A. E. Miroshnichenko, M. L. Brongersma, Y. S. Kivshar, and B. luk'yanchuk, Science **354**, aag2472 (2016).
[43] S. Jahani and Z. Jacob, Nature Publishing Group **11**, 23 (2016).
[44] Y. Ebihara, R. Ota, T. Noriki, M. Shimojo, and K. Kajikawa, Nature Publishing Group **5**, (2015).
[45] A. Kljatov, https://chaoticmind75.blogspot.jp/2016/08/collection-of-fernlike-dendrites.html (2018).
[46] 菊池勝弘, 梶川正弘, 雪の結晶図鑑 (北海道新聞社, 北海道, 2011).
[47] M. Matsushita, *Physics of Fractals (I)* (Shokabo, Tokyo, 2002).

[48] X. Zhao, J. Mater. Chem. **22**, 9439 (2012).
[49] W. Zhao, X. Zhao, K. Song, and Y. Zhou, Photonics and Nanostructures - Fundamentals and Applications **9**, 49 (2011).
[50] W. Zhao and X. Zhao, Optical Materials **32**, 422 (2010).
[51] B. Liu, X. Zhao, W. Zhu, W. Luo, and X. Cheng, Adv. Funct. Mater. **18**, 3523 (2008).
[52] H. Liu, X. Zhao, Y. Yang, Q. Li, and J. Lv, Adv. Mater. **20**, 2050 (2008).
[53] W. Zhu, X. Zhao, and J. Guo, Appl. Phys. Lett. **92**, 241116 (2008).
[54] X. Zhou, Q. Fu, Q. H. Fu, J. Zhao, Y. Yang, and X. Zhao, Opt. Express **14**, 7188 (2006).
[55] X. Zhou and X. Zhao, Appl. Phys. Lett. **91**, 181908 (2007).
[56] Y. Fei Chan, C. Xing Zhang, Z. Long Wu, D. Mei Zhao, W. Wang, H. Jun Xu, and X. M. Sun, Appl. Phys. Lett. **102**, 183118 (2013).
[57] Z. Yi, S. Chen, Y. Chen, J. Luo, W. Wu, Y. Yi, and Y. Tang, Thin Solid Films **520**, 2701 (2012).
[58] H. Xu, M. Shao, T. Chen, Y. Zhao, and S.-T. Lee, J. Raman Spectrosc. **43**, 396 (2011).
[59] S. Xie, X. Zhang, D. Xiao, M. C. Paau, J. Huang, and M. M. F. Choi, J. Phys. Chem. C **115**, 9943 (2011).
[60] L. Wang, H. Li, J. Tian, and X. Sun, ACS Appl. Mater. Interfaces **2**, 2987 (2010).
[61] W. Ye, C. Shen, J. Tian, C. Wang, C. Hui, and H. Gao, Solid State Sciences **11**, 1088 (2009).
[62] A. Campion and P. Kambhampati, Chem. Soc. Rev. **27**, 241 (1998).
[63] M. I. Stockman, V. M. Shalaev, M. Moskovits, R. Botet, and T. F. George, Phys. Rev. B **46**, 2821 (1992).
[64] B. B. Mandelbrot, Science **156**, 636 (1967).
[65] F. Miyamaru, Y. Saito, M. W. Takeda, B. Hou, L. Liu, W. Wen, and P. Sheng, Phys. Rev. B **77**, 145124 (2008).
[66] S. Gottheim, H. Zhang, A. O. Govorov, and N. J. Halas, ACS Nano **9**, 3284 (2015).
[67] C. Puente-Baliarda, J. Romeu, R. Pous, and A. Cardama, Ieee Transactions on Antennas and Propagation **46**, 517 (1998).

Chapter 2.
Optical three-dimensional growth of silver nanodendrites

Potentials of silver nanodendrites as metamaterials were discussed in the previous chapter. In this chapter, I describe the mechanism of the silver nanodendrite growth based on statistical thermodynamics. I also explain a method of silver nanodendrite growth from substrates with exploitation of plasmon resonance excitation by UV light. I discuss parameter optimizations of the experimental system for the growth of the silver nanodendrites. I discuss fractal characteristics of the silver nanodendrites. I finally explain nondestructive extraction of the silver nanodendrites via supercritical fluid.

2.1 Growth of dendritic structure

Here, I explain some fundamentals to understand mechanisms of dendrite growth [1-4]. The base of crystal growth is statistical thermodynamics. Crystallization means phase transition to crystal phase from the other phases such as liquid and gas. Explanations of the crystal growth are slightly different among the cases in solution, melt, and gas. However, the essence is the same. In this term, I focus on the crystal growth from the solution.

Chemical potential: driving force of crystal growth

Now, assume a solution with a solute and a solvent. With regard to the solute, crystal is a phase of low energy where particles such as atoms and molecules are arrayed with regularity and make bonds with each other. In contrast, dissolution is a phase of high energy where the regularity of the particles is disordered. Every material tends to have low energy phases with order, whereas it also try to have high energy phases with disorder due to thermal motion.

The higher the temperature is, the more active the thermal motion. Disordered states with higher entropy is preferred at higher temperature. As a consequence of a competition between these two tendencies conflict with each other, stable states of the material are decided. This is the state where free energy G defined as the following equation goes the minimum

$$G = E - TS \,, \tag{2.1}$$

where E, T, and S are internal energy, temperature, and entropy of the material. At low temperature, the free energy is the minimum when the internal energy is low. Hence, crystallization tends to be occurred. At high temperature, in contrast, the second term $-TS$ is effective for minimizing the free energy, meaning that the material tends to have disordered state.

In a situation of minimum free energy, crystal phase and dissolution phase of the solute often coexist in the solution. The coexist means two phase transitions, crystallization and dissolution, is in equilibrium with each other. Now, free energy of crystal phase and dissolution phase is defined as G_c and G_d respectively. Amount of change on free energy of crystal phase and dissolution phase when a particle of the solute goes in and out between these two phases is then described in the followings

$$\mu_c = \frac{\partial G_c}{\partial N} \,, \tag{2.2}$$

$$\mu_d = \frac{\partial G_d}{\partial N} \,, \tag{2.3}$$

where N is the number of the particle. μ_c and μ_d are referred to as chemical potential of crystal phase and dissolution phase. In the equilibrium of crystal phase and dissolution phase, these chemical potentials are equivalent with each other. This condition means the total free energy $G = G_c + G_d$ is minimum. Magnitude correlation of these chemical potentials decides direction of phase transition. From phases of higher chemical potentials to phases of lower chemical potentials, the phase transition occurs. Difference of magnitude between these chemical potentials corresponds to driving force of phase transition.

In supersaturated solutions, the chemical potential of dissolution phase of the solute is higher than that of crystal phase. If phase transition from dissolution phase to crystal phase occurs, then the free energy of the whole system decreases in

$$\Delta\mu = \mu_d - \mu_c > 0 \,, \tag{2.4}$$

per particle. Hence, crystallization occurs in the supersaturated solutions. Driving force of the crystallization is described as the following

$$\begin{aligned}\Delta\mu &= \frac{d\mu}{dc}\delta_c \\ &= k_B T \ln\frac{c}{c_e} \\ &= k_B T \ln\left(1+\frac{c-c_e}{c_e}\right) \\ &\approx k_B T\sigma\ ,\end{aligned} \tag{2.5}$$

where k_B, c, c_e, and $\sigma = (c - c_e)/c_e$ are Boltzmann constant, concentration, saturated concentration, and supersaturation of the solutes. The driving force is proportional to the supersaturation. δ_c means slight change of the concentration. In the case of crystallization in melt, the driving force is proportional to supercooling instead of the supersaturation.

Crystal nucleus formation and equilibrium shape

Crystallization occurs when the crystal phase has the chemical potential smaller than that of the dissolution phase. However, crystal growth does not occur if the difference of the chemical potentials between these phases, namely supersaturation, is small. This is because a high energy is needed to form seed of crystal, namely crystal nucleus.

The particles make chemical bonds with each other and are stable inside of the crystal. In contrast, the particles at the interface of the crystal facing the solution cannot have the bonds. Hence, the density of the bonds at the interface is smaller than that inside of the crystal. This means that the particles at the interface have higher energy than that inside of the crystal. The interface tends to reduce its area to lower the energy. If the size of the crystal is small, the interface is dominant rather than the interior. If the crystal nucleus is not large to some extent, the crystal nucleus does not grow and dissolve again. Therefore, a free energy enough to conquer the energy wall is needed to form the crystal nucleus. The redundant energy at the interface of the crystal is called as interfacial free energy, and the density of the energy is called as interfacial free energy density or simply interfacial tension.

Here, we consider concretely the above with a simple spherical crystal. Now we suppose that a crystal nucleus with radius r was formed in a supersaturated solution. The change of the total free energy of the system is then written as follows

$$\Delta G(r) = \frac{4\pi r^3}{3\upsilon}\Delta\mu + 4\pi r^2\gamma\ , \tag{2.6}$$

where v and γ are the volume of one particle and the interfacial free energy density or interfacial tension. Figure 2.1 describes ΔG of the Eq. (2.6) as a function of r. The total free energy decreases in proportional to the driving force, whereas increase in proportional to the interfacial tension. In small radius, the second term is more dominant than the first term in Eq. (2.6). The free energy thus increases as increase of the radius. At a radius called as critical radius, the total free energy has the maximum. The critical radius r^* and the maximum of the total free energy ΔG^* are described as below

$$r^* = \frac{2v\gamma}{\Delta\mu}, \tag{2.7}$$

$$\begin{aligned} \Delta G^* &= \frac{4\pi r^{*2}\gamma}{3} \\ &= \frac{16\pi\gamma^3 v^2}{3\Delta\mu^2}. \end{aligned} \tag{2.8}$$

The crystal nucleus with the critical radius is called as critical nucleus. With the radius larger than r^*, the first term is more dominant than the second term in Eq. (2.6). Hence, the crystal nucleus larger than the critical nucleus can grow father. The maximum of the total free energy and the critical radius are smaller when the driving force is larger and the interfacial tension is smaller.

As mentioned above, there is the energy wall to form the crystal nucleus. The wall is conquered by thermal fluctuation. The smaller the maximum of the free energy wall and

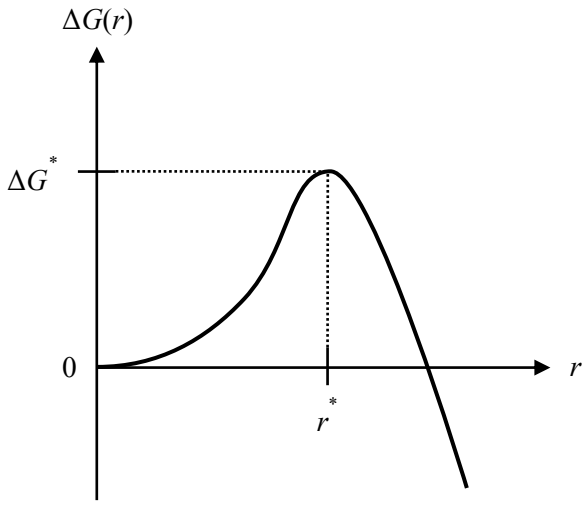

Figure 2.1| Total free energy as a function of radius of crystal nucleus.

the critical radius are, the higher the frequency of formation of the critical nucleus due to the thermal fluctuation is.

Needless to say, actual crystals tend to have polyhedrons. However, the essence described above is the same. The important is that the density of the interfacial free energy is different among orientations of the crystals. The crystals tend to decrease the orientations with high interfacial tension, and finally have a crystal shape called equilibrium shape. The equilibrium shape is the geometry whose interfacial tension is the smallest with maintaining the volume of the crystals. The maximum of the energy wall in the case of the polyhedral crystals is written by the following

$$\Delta G^* = \frac{1}{3}\sum_i A_i \gamma_i \,, \tag{2.9}$$

where A_i γ_i are the area of ith interface forming the critical nucleus and corresponding interfacial tension. Crystals which have face-centered-cubic (fcc) structure, such as silver and gold, have the equilibrium shape shown in Fig. 2.2 [5].

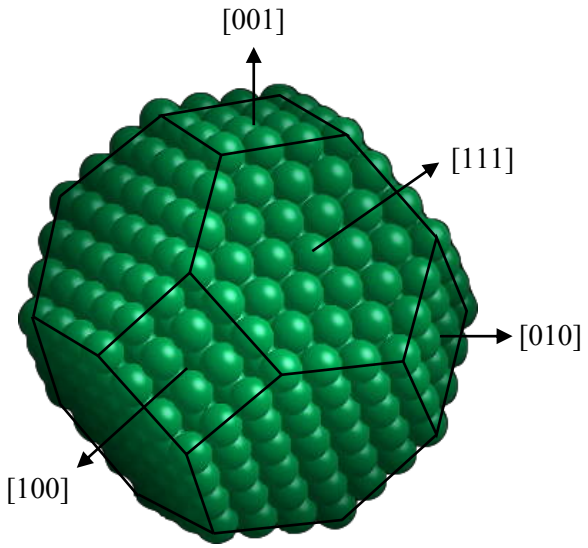

Figure 2.2| A schematic of equilibrium shape of fcc crystals. Image referred from [5].

Crystal growth in diffusion field

Crystal nuclei larger than the critical nucleus grows further. On the other hand, the number of particles of the solute needed increases with increase of crystal size. If the total amount of the particles in the solution is constant, the crystal growth sooner or later stops. Even if the amount of the particles can be increased, moreover, steady growth of the crystals maintaining their shapes is actually impossible.

It has been unveiled that the concentration of the solute far from the crystal interface need to be the same as that of crystal inside for steady growth of the crystals. However, it is clearly impossible. The case of growing spherical crystals is similar. The growth velocity of the spherical crystals is described as below

$$\begin{aligned} V &= \frac{dr}{dt} \\ &= \upsilon D \frac{c_\infty - c_e}{r + d_K}\left(1 - \frac{r^*}{r}\right), \\ D &= \frac{k_B T}{6\pi\eta a}, \quad d_K = \frac{D}{K}, \end{aligned} \tag{2.10}$$

where c_∞ is the concentration of the solute at distant place. D, η, and a are diffusion constant, the viscosity of the solvent, and the radius of the particles. d_K is called as kinetic length, and K is kinetic constant which represent growth velocity per unit supersaturation. The growth

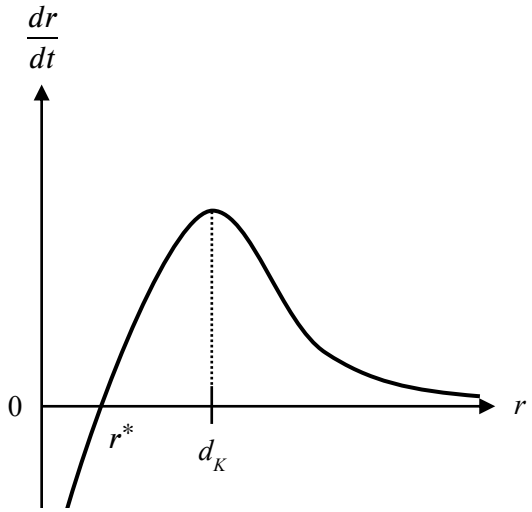

Figure 2.3| Velocity of crystal growth as a function of radius of crystals.

velocity of the spherical crystals behaves as shown in Fig. 2.3. As the radius increases and the rounded interface reaches to plane, the growth velocity becomes slow.

Regardless of plane and spherical interfaces, the growth velocity becomes slow and eventually reaches to nearly zero. The smaller the size of the crystals is, in contrast, the higher the growth velocity is. Then, how does crystal growth behave if there are tiny bumps on the interface? The bumps actually can easily grow compared to the interface around the bumps.

At the interface of the crystals, the solute is consumed by the crystals. Hence, the concentration of the solute around the interface is lower than that of a distant place. Concentration gradient can thus be formed around the interface (Fig. 2.4 (a)). The concentration gradient has thermal fluctuation, and the thermal fluctuation creates the bump on the interface (Fig. 2.4 (b)). As mentioned above, the bump can grow faster than the plane interface. In addition, the bumps protrude to areas of high concentration of the solute, stimulating growth of the bump. On the other hand, the growth of the bumps is restrained due to existence of interfacial tension. The interfacial tension is higher as the curvature of the bumps is small.

The growth of the bumps is determined by competition between the concentration gradient stimulating crystal growth and interfacial tension inhibiting the growth. Here, the two quantities, diffusion length and capillary length which characterize effect of diffusion

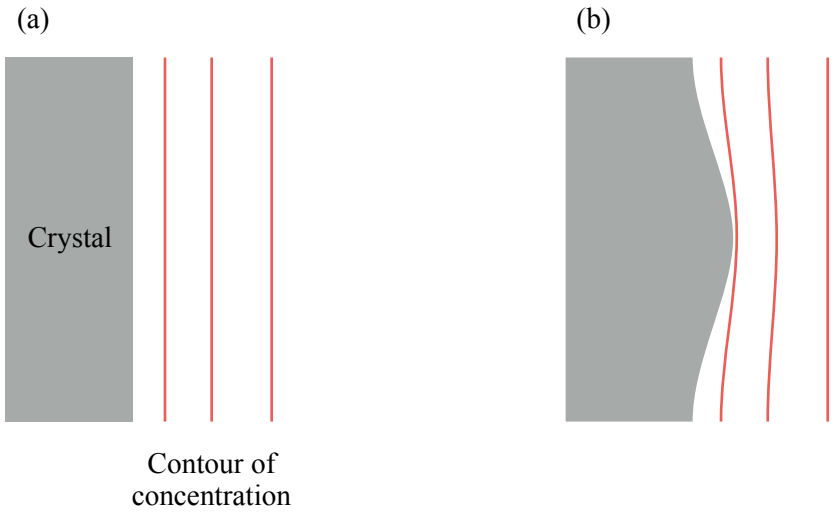

Figure 2.4| Schematics of shapes of crystal surface and solute distribution. In the case of (a), crystal surface is flat with uniform concentration gradient. When a bump is created by thermal fluctuation as shown in (b), the concentration gradient becomes large around the bump.

field and interfacial tension respectively, are defined. These quantities have the unit of length. The diffusion length l_D is defend with diffusion constant D and growth velocity V as follows

$$l_D = \frac{D}{V}. \tag{2.11}$$

The capillary length is defined by the following equation

$$l_C = \frac{\gamma v^2 c_e}{k_B T}. \tag{2.12}$$

The condition where effects of the diffusion field and the interfacial tension balance with each other is described as below

$$\lambda^* = 2\pi\sqrt{l_D l_C}, \tag{2.13}$$

and this quantity λ^* is called as critical wavelength. If the radius of curvature of the bumps is smaller than the critical wavelength, the interfacial tension is dominant. Hence, the bumps are inhibited and eventually vanished. If the radius of curvature of the bumps is larger than the critical wavelength, the diffusion field is dominant. Hence, additional bumps emerge from the interface of the bumps. Only the bumps whose radius of curvature corresponds to the critical wavelength can grow further.

For stable growth of the bumps, however, anisotropy is needed to the interface free energy. If the interface free energy is isotropy as the spherical crystals, the bumps can grow to any directions. The bumps will eventually wind and rift. Only if the interface free energy has anisotropy such as the polyhedral crystals, the bumps can steadily grow and become needle-like crystals. In the case of the anisotropic interface free energy, interfacial stiffness $\tilde{\gamma}(\theta)$ defined as below is considered instead of the interfacial free energy

$$\tilde{\gamma}(\theta) = \gamma(\theta) + \frac{d^2\gamma(\theta)}{d\theta^2}. \tag{2.14}$$

The interfacial stiffness gives strength of stability against distortion of the interfaces. Note that directional dependence of magnitude is opposite between the interfacial free energy and the interfacial stiffness. The interfacial stiffness is small when the interfacial free energy is large, meaning that the strength of stability to maintain plane interfaces against distortion is small. The needle-like crystals tend to grow along the directions of small interfacial stiffness.

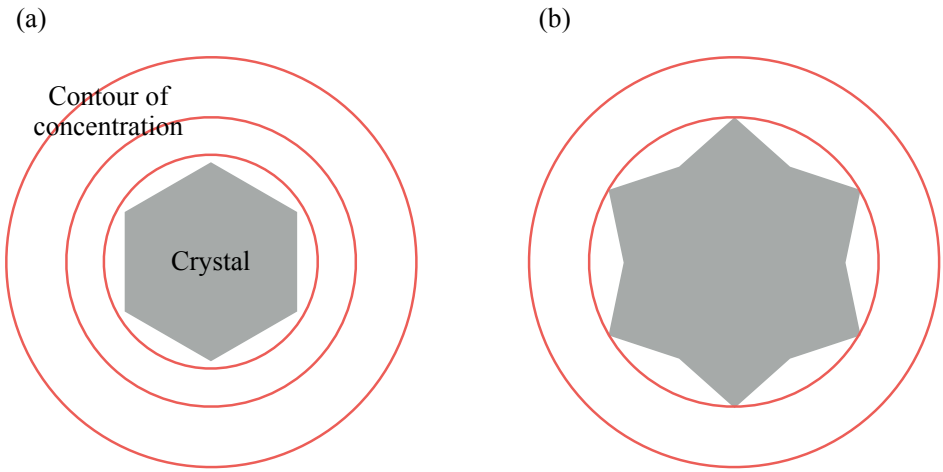

Figure 2.5| Schematics of concentration gradient around polyhedral crystal (a), and growth at apexes of polyhedral crystal (b).

The same phenomenon occurs around interfaces of the needle-like crystals, making them dendritic crystals. Branches of the dendrites grow with a regularity due to atomic arrangement of the crystals. A series of mechanisms of crystal growth described above is called as *Mullins-Sekerka instability*.

The needle-like crystals and the dendrites can grow easier at apexes of the polyhedral crystals than the other interfaces. Here, suppose an equilibrium and polyhedron crystal in a supersaturation solvent with uniform concentration. Contours of concentration around the crystals can be approximated as concentric circles when the contours are adequately far from the crystal (Fig. 2.5 (a)). Apexes of the crystals steps into areas of higher concentration compared to center of the crystal interfaces. Therefore, the crystals tend to grow faster on the apexes than on center of the interfaces (Fig. 2.5 (b)). This mechanism is called as *Berg effect*.

Experimental growth of silver nanodendrites

Oxidation-reduction reaction of silver ion with reductants has been widely applied to grow silver nanodendrites and the other silver nanostructures [6-10]. In addition, surface depositions (electrochemical method [11,12], galvanic replacement [13-19], and hydrothermal replacement [20-22]) have been frequently applied for dendrite growth onto surfaces. External microwave has been also induced for heating of solutions [23-25]. Silver nitrate has mainly used as a resource of silver ion. Surfactants have been often utilized to control the direction of growth [6,7,10,12,14,25-27]. It is known that growth of needle-like crystals and branches

of nanodendrites preferentially occurs from crystal facets with high interfacial free energy (low interfacial stiffness). In the case of fcc crystals such as silver, the magnitude of interfacial free energy of the low-index facets, {100}, {110}, and {111} has a sequence {111} < {100} < {110}. The sequence of the stiffness is {110} < {100} < {111}. Hence, the nanodendrites prefer to grow along the direction ⟨110⟩ the most. ⟨110⟩ corresponds to directions parallel to each side of hexagonal plane of {111} facet as shown in Fig. 2.2. Hence, growth of the needle-like crystals and branching occurs toward ⟨110⟩ direction the most with the angle of branches 60 degrees.

As described in the last subsection, inhomogeneity of concentration gradient of the solute around growing crystals is essential for the nanodendrite growth. The concentration gradient is formed when diffusion of the solute and crystal growth are in a balance with each other. Therefore, control of diffusion field of the solute and the velocity of crystal growth is

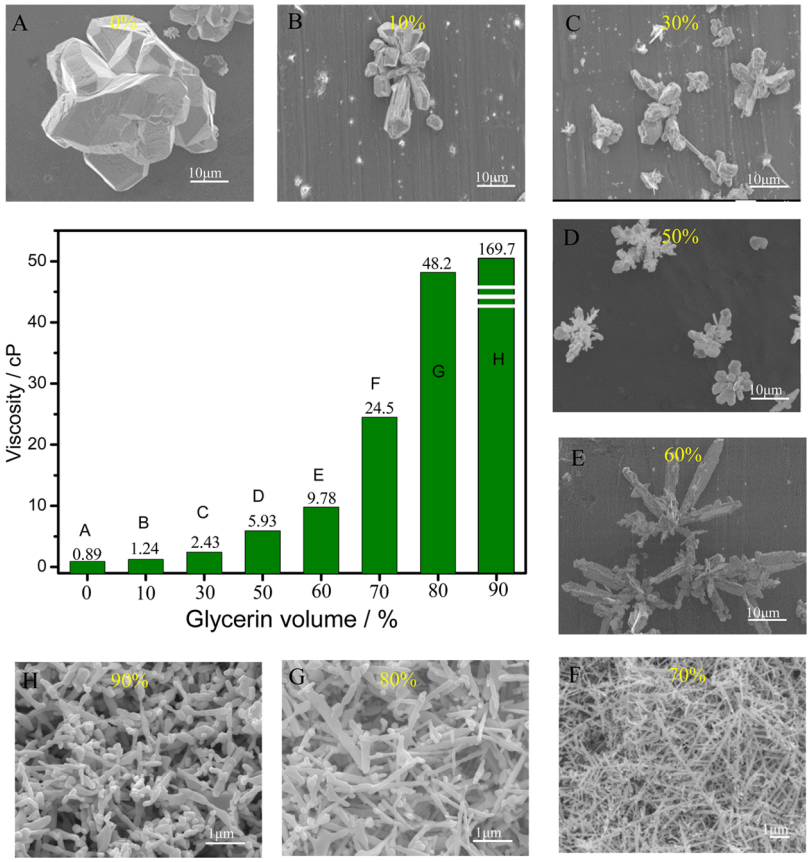

Figure 2.6| Viscosities of solvents at different volume ratios of glycerol in water (green bars). SEM images indicated by A-H show silver nanostructures grew in each solvent with current density 50 μA·cm^{-2}. Figure referred from [11].

important for stable dendrite growth. If the viscosity of the solvent is extremely high, the solute is difficult to diffuse in the solution and the concentration gradient is thus hard to be formed. If the velocity of crystal growth is extremely fast or slow, the concentration gradient is also hard to be formed.

Liu *et al.* presented changes of the shapes of silver nanostructures among differences of diffusion field and the velocity of crystal growth [11]. An electrochemical approach was applied; silver ion was reduced on the surface of an electrode where electron was supplied and the silver nanostructures grew on the surface. The viscosity of a solvent was varied by changing the ratio of water and glycerol. The velocity of crystal growth was varied by changing the intensity of induced current. Figure 2.6 shows a set of changes of silver nanostructures along the viscosity of the solvent with a constant current. In the case of low viscosity, silver ion as the solute can easily diffuse. The silver ion can reach to the surface of growing crystals

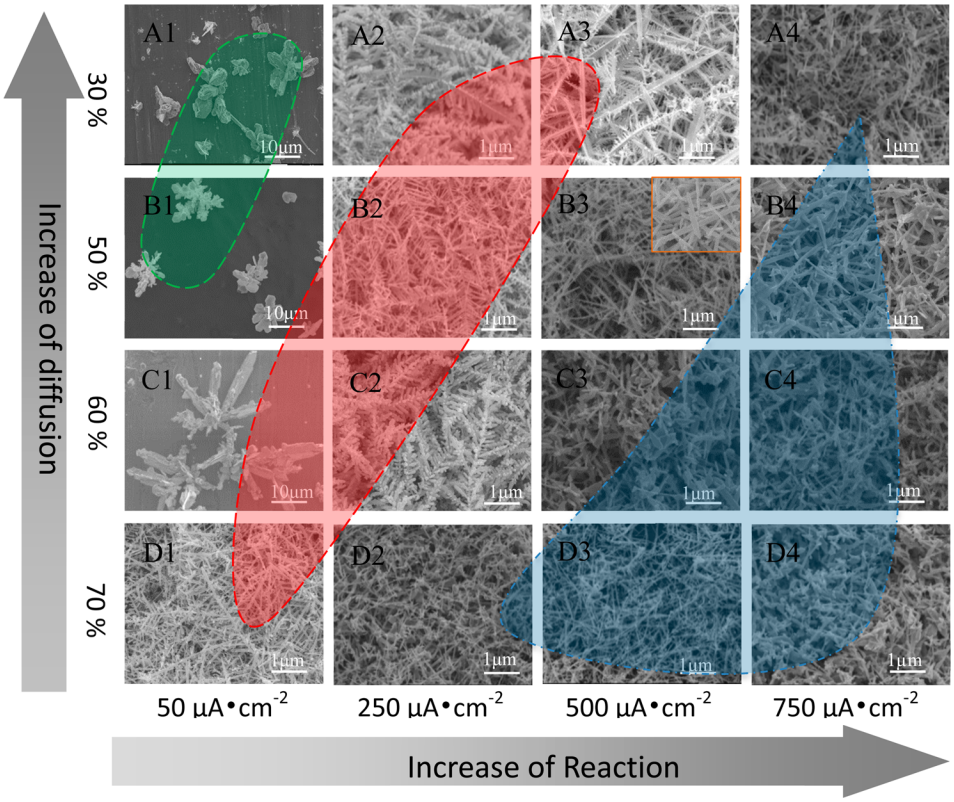

Figure 2.7| Silver nanostructures grew under different reaction and diffusion conditions. The horizontal axis shows the reaction rate by changing magnitude of the induced current. The vertical axis shows the diffusion rate by changing volume ratio of glycerol in water. The images covered by green are polyhedral silver aggregates, whereas the images covered by the red and blue are dendritic and fibroid structures, respectively. Figure referred from [11].

and be reduced. Since the solute is constantly supplied to the growing crystals, the concentration gradient of the solute is hard to be formed around the growing crystals. As the viscosity of the solvent increase, the crystals start to branch and become dendritic shapes. In the case of high viscosity, on the other hand, the silver ion is difficult to diffuse. Silver atoms reduced around the surface of the electrode can make bond with other silver atoms around them before reaching to the growing crystals. A number of new silver nanostructures can thus be formed. Figure 2.7 shows a distribution of the shape of silver nanostructures among differences of the diffusion field and the velocity of crystal growth. The nanodendrites appear in the area covered with the red shadow, indicating that the concentration gradient of the solute is formed. The balance between the diffusion field and the velocity of crystal growth is thus important for dendrite growth.

2.2 Plasmonic heating of silver nanoparticles

The silver nanodendrites grow by reduction of silver ion. As described in the end of the last section, there are some methods for the silver nanodendrite growth. In this thesis, a novel method for the silver nanodendrite growth with utilization of heating generated by surface plasmon resonance (SPR) is proposed. By this method, the silver nanodendrites can be grown with light from substrates.

Now, consider a system which silver nanoparticles with diameter less than 10 nm are on a substrate and a mixed solution droplet of silver nitrate ($AgNO_3$) and L-ascorbic acid (LAA) as a reductant as shown in Fig. 2.8. The system is wholly cooled below 273 K to restrain unwanted reduction reaction of the silver ion. When CW laser with λ = 355 nm is irradiated to the silver nanoparticles on the substrate, plasmon resonance is excited on the surface of each nanoparticle. The absorption peak of the nanoparticles is 385 nm (see Fig. A2.1 in Appendix of this chapter). The plasmon resonance is a collective oscillation of electrons, thus generating heat. Areas around the nanoparticles obtain higher temperature than other distant areas, reduction reaction thus being more active in these areas. Hence, nanodendrite growth can easily occur from the silver nanoparticles. The silver nanoparticles can be considered as *seeds* for the silver nanodendrites. The grew silver nanodendrites are obtained by washing the remained solution droplet and drying the substrate.

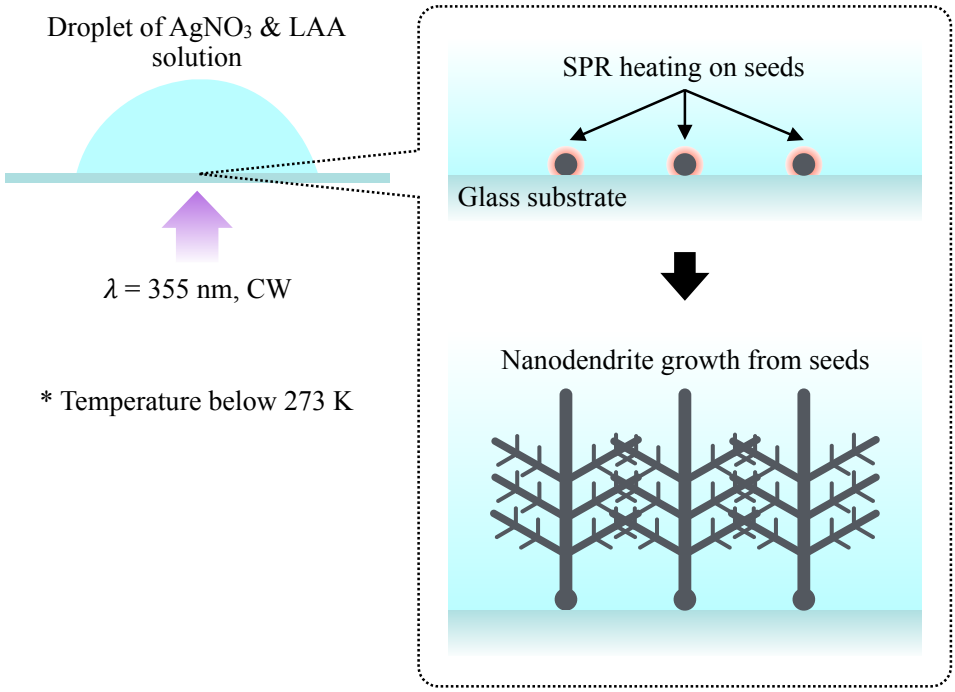

Figure 2.8| A schematic of experimental system of silver nanodendrite growth from silver seeds via SPR heating generated by UV light.

Silver nanostructure growth with SPR heating has been actively studied by Mirkin [28]. However, there is no previous study regarding silver nanodendrite growth by SPR heating.

Seed-substrate prepared via surface modifications

The seeds are chemically fixed on a glass substrate. To fix the seeds onto the substrate, silane coupling is utilized for surface modification of the substrate. Figure 2.9 describes the procedure of seed-substrate preparation via surface modifications. The glass substrate is cleaned by plasma processing, and hydroxyl groups are exposed onto the surface of the glass substrate at first. Next, amino groups are decorated onto the surface of the glass substrate by silane coupling. Molecules of a silane coupling agent with amino group and the hydroxyl groups on the surface of the glass substrate make bonds via dehydration synthesis. The seeds whose surfaces are capped with citric acid molecules are then fixed onto the surface of the substrate with coulomb bond between carboxyl group of the citric acid and the amino group.

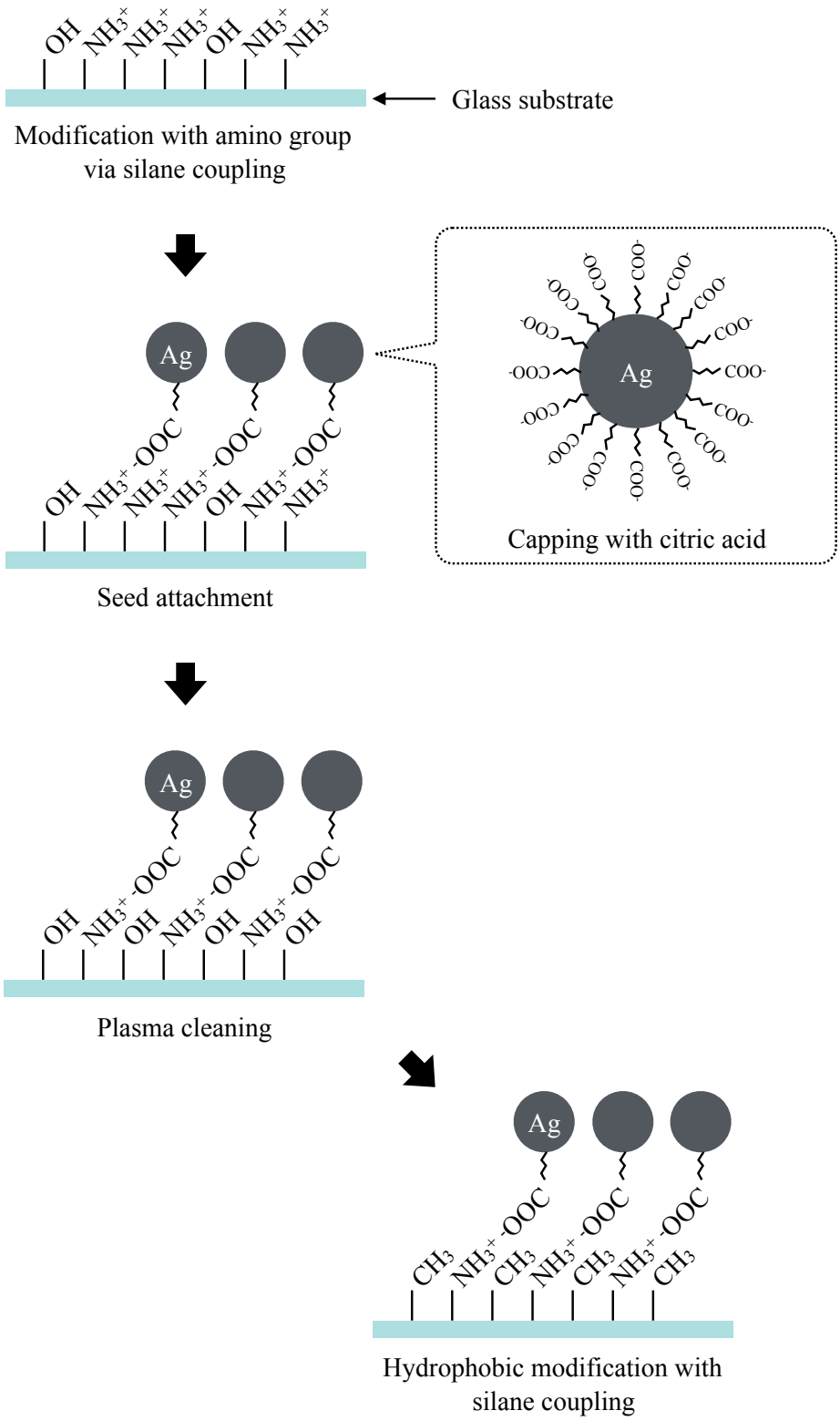

Figure 2.9| A schematic of preparation procedure of seed-substrate via surface modifications.

The amino group and the carboxyl group are polar molecules, thus hydrophilic rather than hydrophobic. Hence, it is hard to form the droplet of the solution of the silver ion and the reductant onto the surface of the substrate. If the solution diffuses on the surface without forming the droplet, the concentration of the silver ion per unit area of the surface of the substrate decreases. The silver nanodendrites are thus hard to be formed. Therefore, hydrophobic modification of the surface of substrate is needed.

As well as amino group decoration, silane coupling is utilized for hydrophobic modification. Plasma cleaning is conducted to the surface of the substrate to remove remained amino groups and expose hydroxyl groups again. Then, methyl groups, which are hydrophobic, are decorated onto the surface via silane coupling, making the surface hydrophobic.

2.3 Nondestructive extraction of silver nanodendrites with supercritical fluid

The principle of plasmonic-growth of silver nanodendrites was discussed above. From here, the nanodendrites grown experimentally are shown. The nanodendrites are fragile. They easily bend and lie down on substrates during removing of ion solution and rinsing of structures with acetone. Here, use of supercritical fluid for extracting nanostructures without damage mainly is discussed. Supercritical fluid of carbon dioxide (CO_2) has been used in the industry of semiconductor nano-devices and MEMS for rinsing [29]. Supercritical fluid does not have surface tension, which produces capillary force. The viscosity of CO_2 supercritical fluid is small not to deform or destroy the structures in the rinsing process of nano-device by the fluid. CO_2 fluid transits to CO_2 gas by decreasing the pressure. As a result, nano-devices are dried and extracted.

Figure 2.10 shows the procedure of fabrication and extraction of silver nanostructures. Acetone-water (with the ratio 34:1) solution of $AgNO_3$ (40 mM) and LAA (60 mM) is dropped on a glass substrate. Silver nano-seeds of a few to several nm in diameter are prefixed on the substrate. The temperature of the solution droplet and the substrate were maintained at 263 K to inhibit production of unnecessary silver nanoparticle reduction in solution. A CW UV laser at λ = 355 nm illuminates silver nano-seeds to excite localized surface plasmon resonance, resulting in local temperature increase at nano-seeds. The temperature increase triggers the growing of nano-rods from nano-seeds by consuming silver ions in solution through reduction. Due to the inhomogeneity of distribution of silver-ion concentration

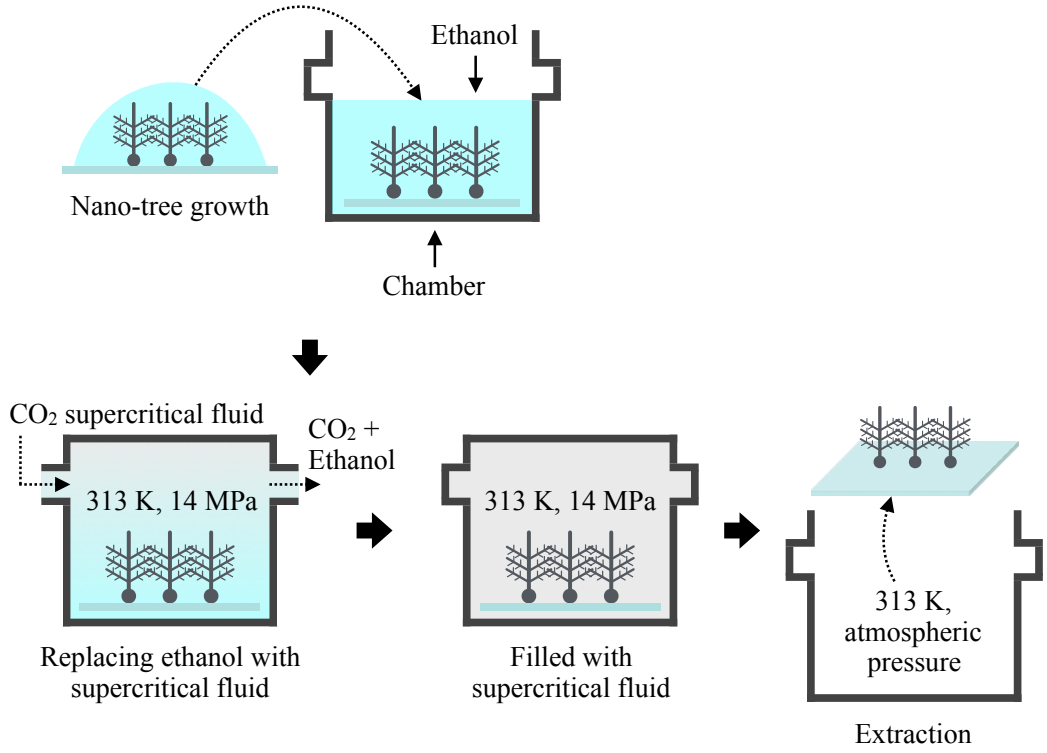

Figure 2.10| Experimental procedure for the growing and extraction of silver nanostructures. Silver nano-trees are grown from silver nano-seeds fixed on the substrate in the acetone-water solution of $AgNO_3$ and LAA, with UV laser illumination to produce local heating by localized plasmon resonance at nano-seeds. Nano-trees are grown in the solution, and the solution dissolves in ethanol in a chamber. Supercritical fluid of CO_2 is injected into the chamber, and then ethanol is replaced by supercritical fluid. The fluid of CO_2 transits to the gas phase, resulting in drying the structure without deformation and destruction.

surrounding the surface of nano-rods, protrusions are grown to produce branches. Branching repeats, forming nano-trees. The details of the procedure, such as preparations of acetone-water solvent, seeds, and seed-substrates, appear in Appendixes of this chapter.

The silver nanostructures in solution are put into a chamber filled with ethanol (100 mL). The acetone-water solution with $AgNO_3$ and LAA dissolves in ethanol. Then, super-critical fluid of carbon dioxide (CO_2) is injected from the port of the chamber, while temper-ature is maintained at 313 K. The pressure and the flow rate of the supercritical fluid are kept 14 MPa and 30 mL/sec, respectively (the critical point of CO_2 is at 304.1 K and 7.38 MPa [30]). The ethanol with the acetone-water solution dissolves in CO_2 supercritical fluid, and

exhausts out from the other port of the chamber with CO_2 gas. The flow rate of CO_2 supercritical fluid is gradually reduced, and CO_2 fluid transits to the gas phase. Finally, the nanostructures are extracted from acetone-water solution without physical damage.

I have carried out the experiment of growing and extraction of silver nanostructures. The results are shown in Fig. 2.11. Figure 2.11 (a) shows a scanning electron microscope (SEM) image of silver nanodendrites extracted with CO_2 supercritical fluid. There is no deformation of structures. The size of this picture is 14×14 μm^2 (magnification of 4,000x). Figure 2.11 (b) shows the same image as Fig. 2.11 (a) except that the viewing angle is 45 degrees tilted, demonstrating that the tree is in three dimensions. Figure 2.11 (c) shows an

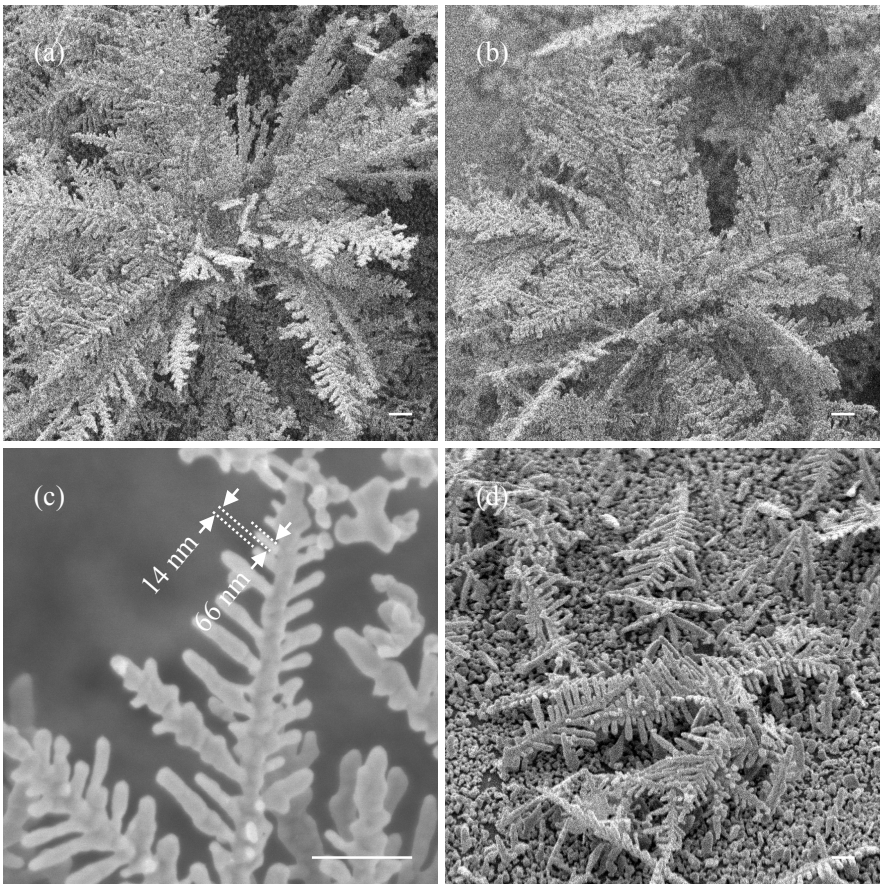

Figure 2.11| SEM images of extracted silver nanostructures grown with plasmonic heating at nano-seeds. (a) and (b) show SEM images of silver nanodendrites extracted with CO_2 supercritical fluid at different viewing angle 0 and 45 degrees, respectively, and (c) an enlarged view. (d) shows nanodendrites extracted with acetone for washing (viewing angle 45 degrees). The scale bar is 1 μm for all. The laser power for nanodendrite growth was 20 mW.

enlarged view of a part of nanodendrite with magnification of 27,000x, where the branches of trees are ~66 nm thick with gap of ~14 nm between adjacent branches. In comparison, a SEM image of nanodendrites extracted with liquid acetone but not with supercritical fluid is shown in Fig. 2.11 (d). Trees lie and overlap each other on the substrate. This is due to the much larger surface tension and viscosity of acetone (23.46 mN/m and 0.324 mPa s at 293 K and ~0.1 MPa, respectively), compared to those of CO_2 supercritical fluid (0 N/m and 0.08 mPa s at 313 K and 14 MPa, respectively) [31,32].

Shape variation of silver nanostructures along UV laser power

The characteristics of silver nanostructures (either sphere, rod, plate or cube, two-dimensional or three-dimensional, and large or small) are determined by the experimental condition. Here, we discuss the laser power dependency to the structural characteristics. The UV laser beam with linear polarization is guided to silver nano-seeds on the substrate without any lenses. The diameter of irradiation spot is 0.98 mm. If the laser power for triggering crystallization at nano-seeds is as low as 10mW, hexagonal plates are grown as crystals (Fig. 2.12 (a)). In the case of low power laser illumination, the reduction rate around nano-seeds is low, so that crystals grow slowly from nano-seeds. In such a slow reaction kinetics, prismatic shape arises from the seeds which contains planar crystallographic defects (e.g. twin planes and stacking faults) [28]. If the laser power is between 20 and 30 mW, three-dimensional crystals are grown as nano-trees (Fig. 2.12 (b) and (c)). As the power of laser increases, the temperature at a nano-seed increases due to the excitation of localized surface plasmon resonance, resulting in the inhomogeneity of silver-ion concentration in solution near the seed. The inhomogeneity triggers crystal growth only at a certain position of seed surface. As a result, a nanorod is grown. Due to the inhomogeneity, protrusions are grown on the surface of the nanorod, resulting in branching in three dimensions. When the power is higher than 35 mW, the reduction occurs not only at the seed but also in the solution due to the temperature increase. As a result, silver granules are reduced in the solution (Fig. 2.12 (d)).

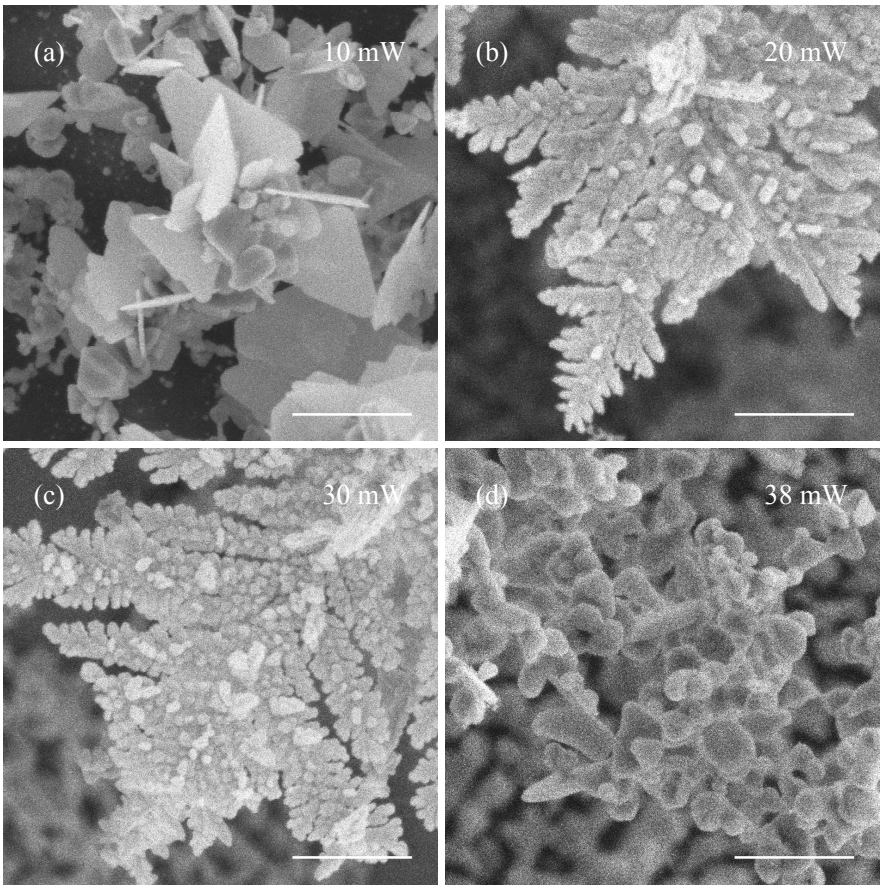

Figure 2.12| Comparison of structural character of nanostructures with different laser power for triggering crystallization. (a)-(d) are SEM images of the structures grown with the laser power of 10 mW, 20 mW, 30 mW, and 38 mW, respectively. The scale bar is 1 μm for all.

2.4 Parameter optimization for silver nanodendrite growth

Parameter control of experimental systems is very important for reproducible bottom-up synthesis of structures. In this section, shape variations of silver nanostructures among experimental parameters are discussed. The shape variations were experimentally observed among variation of the parameters.

In the previous section, the characteristics of the nanostructures along UV laser power were discussed. There, however, are many parameters in the system of light-induced growth of silver nanodendrites: interfacial tension and viscosity of solvent (kind of solvent), temperature, concentration of silver ion and a reductant, parameters of seed-substrate (size and density of seeds, thickness of hydrophobic coating etc.) etc. Here I choose three from the above

as variable parameters: kind of solvents, temperature, and concentration of silver ion and a reductant. This is because those parameters seem to directly affect to formation of concentration gradient of reduced silver atom and thermal fluctuation around the seeds which drive growth of dendrites. In this section, liquid acetone was used for washing the structures, not supercritical fluid.

Structural transition due to interfacial tension and viscosity of solvent

In this part, shape difference of grown silver nanostructures among interfacial tension and viscosity of solvent is explained. Acetone (23.30 mN/m, 0.322 mPa s at 298 K), water (72.75 mN/m, 1.01 mPa s at 298 K), and glycerol (63.40 mN/m, 1499 mPa s at 298 K) were exploited as solvents.

Interfacial tension and viscosity of solvent largely affect to crystal growth and the shape of grown silver nanostructures. By interfacial tension, the interface between the crystals and the solvent attempts to minimize their surface area to minimize surface energy. If the solvent has large interfacial tension, the grown crystals tend to have shapes close to equilibrium shape. Aggregation of the crystals also easily occurs. Therefore, dendrite is hard to be formed in solvents with high interfacial tension. Viscosity largely affects transfer of silver ions and reduced silver atoms in the solvent. High viscosity disturbs diffusion of these solutes. In the solvent with high viscosity, the silver atoms are not sufficiently supplied to the crystals under growing. By aggregating with other silver atoms, new nuclei of silver crystals are also formed. Concentration gradient of silver atom is hence hard to be formed. Therefore, low interfacial tension and viscosity are desirable for dendrite growth. Surfactants are useful to reduce interfacial tension, and are widely used for metal nanoparticle synthesis. However, I did not use any surfactants. This is because the surfactants attach to particular surfaces of the grown crystals and the crystal shape depends on them, making the system of the crystal growth complicated.

Figure 2.13 shows a shape transition of silver nanostructures among the ratio of the solvents; acetone:water = 193:7, 8:2, 6:4, 0:10, water:glycerol = 10:0, 8:2, 4:6. The ratio acetone : water = 193 : 7 is applied when the concentrations of $AgNO_3$ and LAA are 40 mM and 60 mM respectively. The dendrites can be observed even when the ratio acetone:water is 8:2. On increasing the amount of water, the observed silver crystals become aggregations of plate-like crystals and reach to ball-like shapes. The size of the ball-like crystals becomes small with increasing the amount of glycerol.

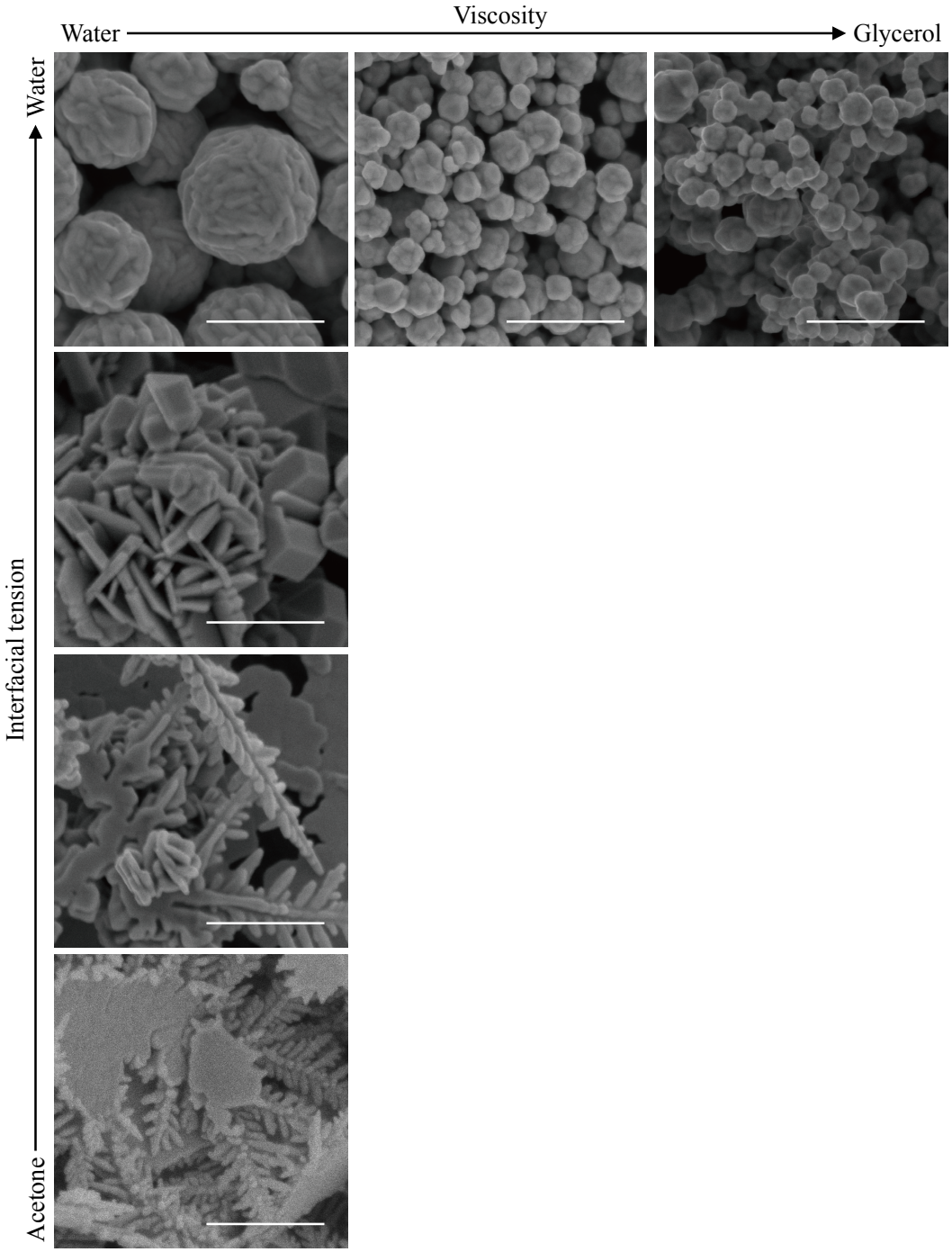

Figure 2.13| SEM images of silver nanostructures among difference of solvents (acetone, water, and glycerol). Scale bars on each image are 1 μm.

Another experiment with ethanol (21.78 mN/m, ~1.1 mPa s at 298 K) instead of acetone also was done. When the ratio ethanol:water = 193:7, the nanodendrites appeared. Ethanol and water protic, whereas acetone is aprotic. This result indicates that electrostatic

characteristics such as proton donor ability do not affect the structural transition, and crumpling of the structures is caused by the interfacial tension. Note that the discussion using Fig. 2.13 is limited in the experimental system of this study: reduction of $AgNO_3$ with LAA and use of light. Inhomogeneity of the concentration gradient is the most important for dendrite growth. If situation is satisfied, dendrites can grow even in water and glycerol as shown in Fig. 2.6.

Suppression of nanodendrite growth at low temperature

The reduction of the silver ion is immediately occurred when the silver ion solution and the reductant solution are mixed, and the silver crystals grow. This means that the silver crystals can grow outside of the irradiation area of the UV light. To avoid the unwanted crystal growth, cooling of the seed-substrate and the droplet of the silver ion/reductant solution is effective. The activation of the silver ion reduction is weakened in low temperature, and the unwanted crystal growth can be suppressed. Here, the tendency of the silver crystal growth along the temperature of the seed-substrate and the solution droplet was studied. The temperature was controlled between 263 K (-10 °C, the lowest temperature of the cooling stage) and 293 K (20 °C, room temperature). UV light was not induced in this experiment.

The result is shown in Fig. 2.14. Silver particles grew on the surface of the seed-substrate at 263 K. However, other silver crystals such as plate-like or dendritic shapes were not observed. The plate-like silver crystals and the dendrites were observed at 268 K (-5 °C) and above 273 K (0 °C) respectively. The lower the temperature of the seed-substrate and the solution droplet is, the stronger the suppression of the silver ion reduction is. Hence, the unwanted silver crystal growth can be avoided. The result shows that the suppression of the silver ion reduction is not perfect and the silver crystals can grow even in the lowest temperature of 263 K. However, growth of the plate-like or dendritic shapes can be avoided.

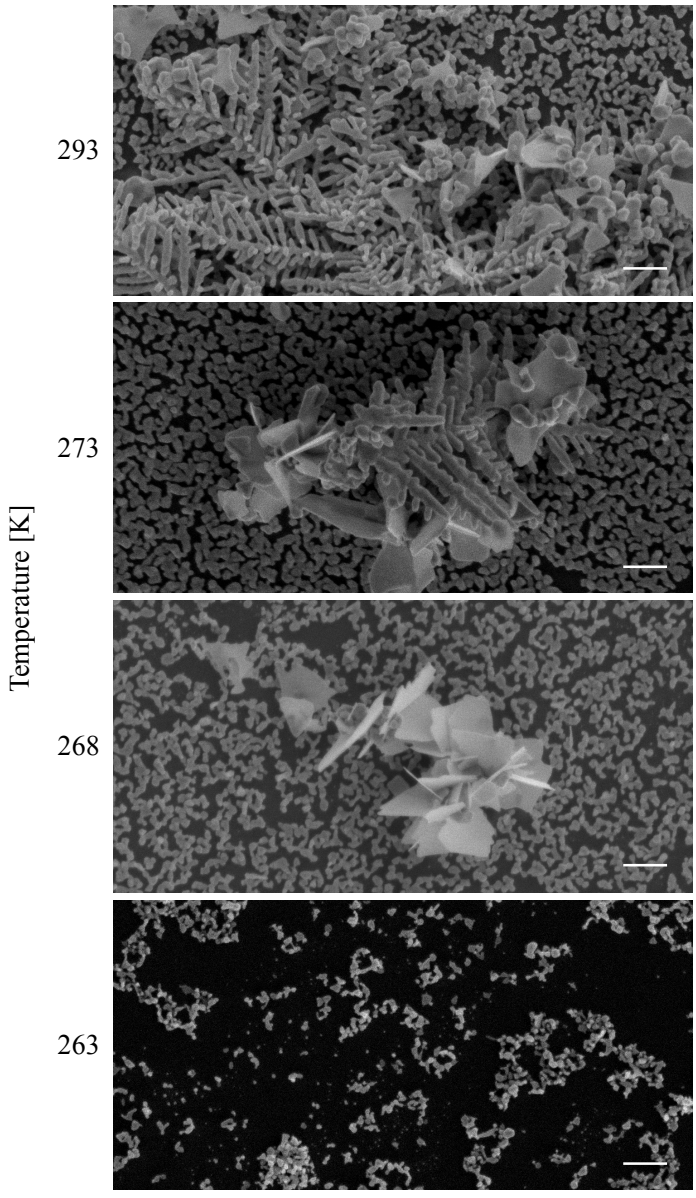

Figure 2.14| SEM images of silver nanostructures synthesized along different temperatures without UV light irradiation. Scale bars on each image are 1 μm.

Structural variation among concentrations of silver ion and reductant

When the concentration of silver atom and the velocity of silver crystal growth are in a balance, the concentration gradient of the silver atom is formed and the dendrites can grow. The silver atom concentration and the velocity of silver crystal growth depend on the velocity of

silver ion reduction. Hence, the concentrations of the silver ion and the reductant are important parameters. The higher the concentrations of the silver ion and the reductant are, the faster the velocity of the silver ion reduction is. When each concentration is low, the plane-like crystals tend to grow. When each concentration is appropriate enough to form the concentration gradient of the silver atom, the dendrites tend to grow.

Here, shape variety of grown silver crystals was studied among the concentrations of the silver ion and the reductant. $AgNO_3$ and LAA were used as the source of the silver ion and the reductant. Each concentration for dendrite growth were confirmed. Adjustment of each concentration was carried out as below. At first, a $AgNO_3$ aqueous solution and a LAA aqueous solutions were prepared with the concentrations of 2 M and 1.2 M respectively. The

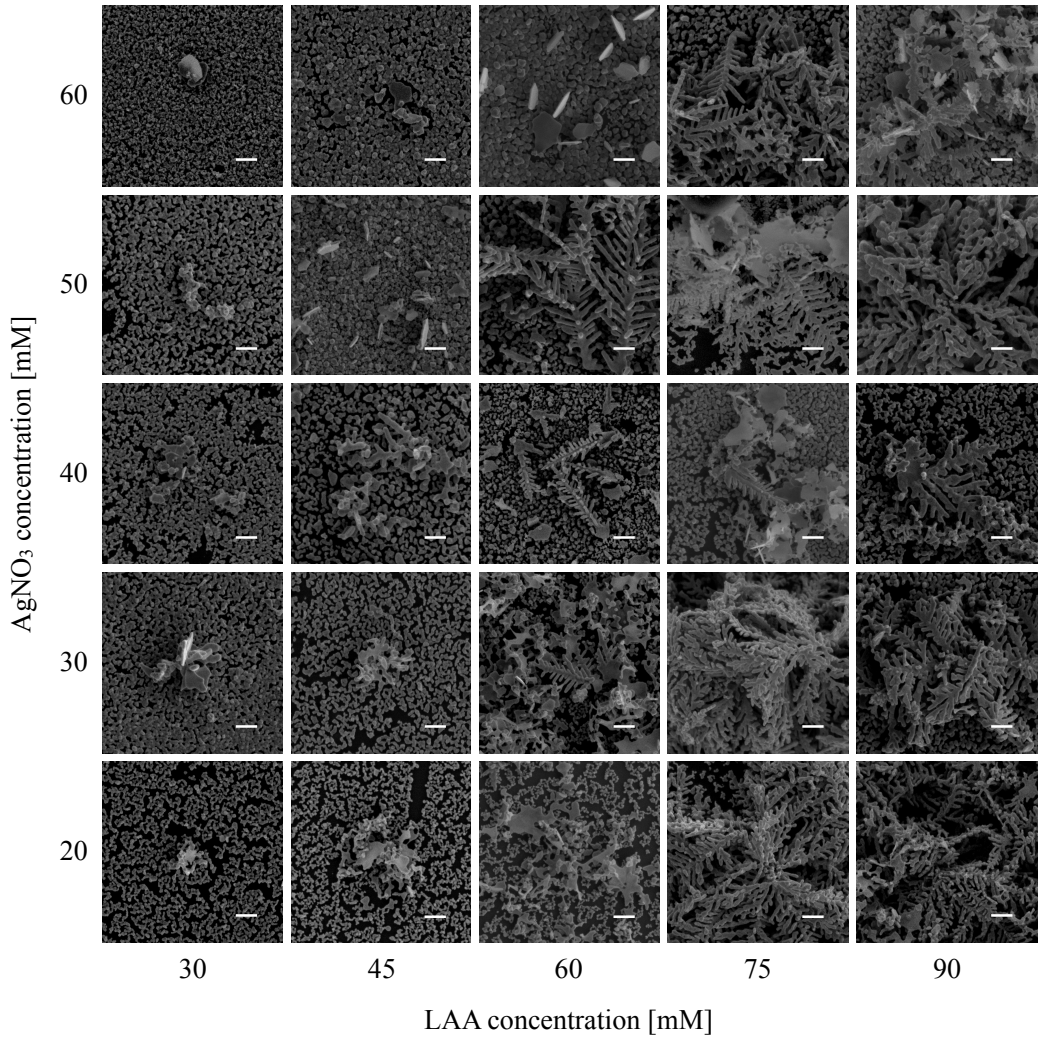

Figure 2.15| SEM images of silver nanostructures among different concentrations of silver nitrate and L-ascorbic acid. Scale bars on each image are 1 μm.

amount of the $AgNO_3$ aqueous solution was measured by a pipette. Then, a $AgNO_3$ acetone/water solution with concentrations between 20-60 mM was prepared by dropping the measured $AgNO_3$ aqueous solution into the acetone. An LAA acetone/water solution with concentrations between 30-90 mM was also prepared with the same method as above. By changing the amount of each aqueous solution, the concentrations of $AgNO_3$ and LAA were varied. The temperature of the seed-substrate and the droplet of these acetone/water solution was maintained to -10 ˚C. The power of UV laser was fixed to 20 mW.

Figure 2.15 shows shape differences of silver crystals grown with different concentrations of $AgNO_3$ and LAA. The dendrites tend to grow when LAA is in a high concentration, mainly 75 mM or above. In contrast, the plate-like crystals tend to grow when the concentration of LAA is low, mainly 45 mM or below. In every concentration of $AgNO_3$, the dendrites appeared. This result indicates that the concentration of LAA more affects to growth of the nanostructures than that of $AgNO_3$. An LAA molecule can give two electrons to silver ion. Hence, the concentration of LAA can more affects to reduction of silver ions per unit time than that of $AgNO_3$, which dominates structural growth. The higher the concentration of $AgNO_3$ is, the larger the amount of grown silver crystals on the surface of the seed-substrate including the dendrites. The silver crystals tend to grow not only on the surface of the seed-substrate but everywhere of the droplet when the concentrations of $AgNO_3$ and LAA is high.

In conclusion, the concentration gradient can be formed and the dendrites can grow when the concentration of LAA is high regardless of the concentration of $AgNO_3$.

2.5 Growth of silver nanodendrites in agarose gel

I have directly proved that the silver nanostructures grew in three-dimension by extracting their structures without destruction. To fabricate 3D bulk materials composed of the nanostructures, I grew the nanostructures inside of agarose gel. In the experiment, the powder of agarose is dissolved in pure water, and agarose gel is immersed in acetone-water solutions of $AgNO_3$ and LAA. This agarose gel containing silver ions is poured into the chamber, into which CO_2 supercritical fluid is injected. Experimental conditions and parameters for extraction with CO_2 supercritical fluid are the same as those explained above with Fig. 2.10. The result is shown in Fig. 2.16. Figures 2.16 (a) and (b) show the SEM images of a silver nanotree grown in agarose gel observed at the viewing angles of 0 and 45 degrees, respectively.

Three-dimensional nano-trees are observed as surrounded and immobilized with fibrous network of agarose. The fibrous network is formed as a result of drying agarose gel with supercritical fluid. Figure 2.16 (c) shows the agarose network without dendrite dried in supercritical fluid (the upper part) and in the air (the lower part), respectively. In the air, agarose fibers aggregates in drying, that would break silver nanostructures (lower part in Fig. 2.16 (c)). Fig. 2.16 (d) shows silver nanostructures in agarose dried in air. It is observable that nanodendrites are not self-standing and lie and overlap each other.

Photopolymerizable resin is another possible matrix to have nanostructures grown inside. There was a report on two-photon metal reduction in gold ion-doped polyvinyl alcohol

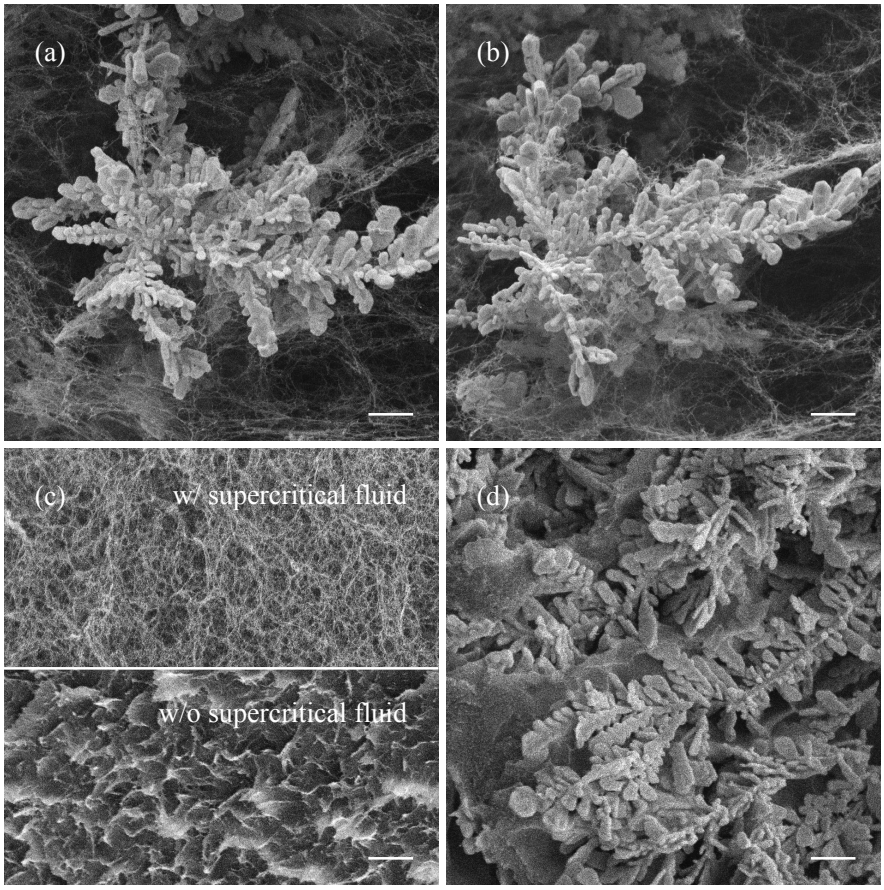

Figure 2.16| Experimental results of silver nanostructures grown in agarose gel. (a) and (b) show SEM images of a nano-tree dried with CO_2 supercritical fluid. The observation angle is 0 degree for (a) and 45 degrees for (b), respectively. Two SEM images of (c) are agarose network without nanodendrites dried in supercritical fluid (the upper part) and in the air (the lower part), respectively. In the air, agarose fibers aggregates in drying. (d) shows silver nanostructures in agarose gel dried in air. The scale bar corresponds to 1 μm for all.

film, although it was not self-growing of nanostructures [33]. Three-dimensional polymer nano/micro structures fabricated with two-photon polymerization or multi-beam interference can also be used as the skeleton-network to immobilize silver nanostructures [34,35].

2.6 Fractal characteristic of silver nanodendrites

Since silver nanodendrites are fractal with self-similarity, to know fractal characteristic of them is interesting. A dendritic structure is characterized by fractal dimension D_f which is a parameter representing the filling factor of the structure in space, and is given by Eq. (1.9) in Chapter 1. In Eq. (1.9), V_d'/V_d is the number of self-similar sub-pieces (branches from the nano-tree stem) required for filling the space of the object (a nano-tree), and ε corresponds to the scale ratio, respectively. D_f can be measured from SEM image through a calculation method called box counting, where n is the number of unit square cells whose size is $l \times l$ (l is the unit length), occupying the object in the SEM image (reference [47] in Chapter 1). With n and l, Eq. (1.9) is expressed as

$$D_f = \frac{\log n}{\log \frac{1}{l}}. \tag{2.15}$$

The fractal dimension of the nanodendrites depends on the geometry of the structure, in particular, the density of the branches. This means the fractal dimension gives us complexity of the structures, and higher value indicates higher complexity. Figure 2.17 shows plots of $\log n$ to $\log(1/l)$ for different nano-trees. D_f is given by the slope. The red-circular and blue-square plots shows D_f of 1.792 and 1.651, respectively. Each plot is obtained from each SEM image of the nano-trees with red and blue flame. The value of D_f is different between these nano-trees, which comes from density difference of the branches. The temperature for structural growth is different between those nano-trees: 310 K for the red-flamed nano-tree and 323 K for blue-flamed one. This result indicates that D_f varies among temperature: higher temperature gives us nano-trees with lower structural density. In the case that crystal growth is slightly more dominant than diffusion, the concentration of reduced silver atoms around crystals under growing becomes smaller. This situation makes growth of new branches hard, resulting in formation of nanodendrites with low structural density [11]. If the

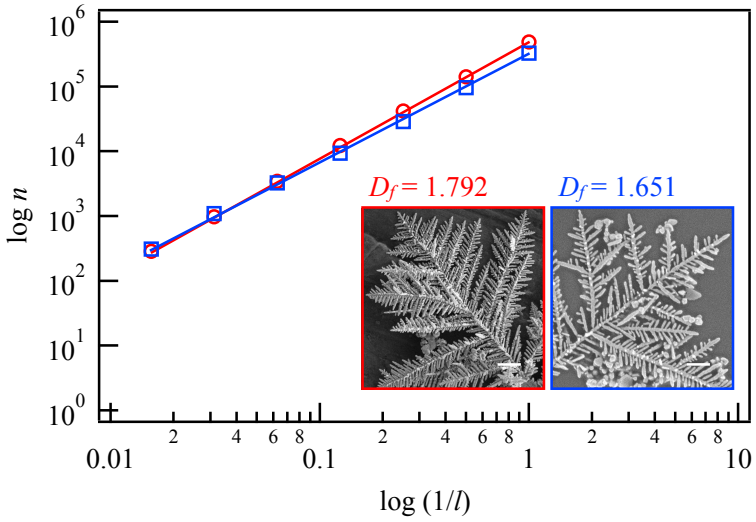

Figure 2.17| Fractal dimensions D_f of silver nanodendrites analyzed with box counting. Red-circular and blue-square plots are obtained from the inset SEM images of nano-trees with red and blue flames, respectively. D_f is given by slope of the lines fitted onto each plot. D_f of the red-flamed nano-tree and the blue-flamed nano-trees is 1.792 and 1.651, respectively. The scale bar in each SEM image is 1 μm.

temperature is in excess, granular crystals seem to appear. As a reference, D_f of "H"-shaped fractal structures shown in Fig. 1.13 is ~1.6. Also, D_f of natural coastal line (the west coast of Britain) is typically ~1.25 (reference [64] in Chapter 1).

2.7 Absorption of silver nanostructures

I attempted to experimentally understand optical characteristics of silver nanodendrites. The nanodendrites are fractal, which means that self-similar nanostructures with various sizes simultaneously exist. Hence, broadband absorption is expected due to plasmon resonance of the nanostructures. Moreover, it is interesting if electromagnetic responses originating in the structure of the nanodendrites itself (the detail is shown in Chapter 3) are experimentally observed. Silver nanodendrites were prepared by reduction of $AgNO_3$ and LAA on a seed-substrate at the temperature ~313 K with supercritical fluid process (Sample A). Another sample (Sample B) also was prepared with the same method except the temperature 263 K and washing with liquid acetone. There are no nanodendrites, but only granular or plate structures on sample 2. Through an aperture with the diameter 3 mm, depolarized light was

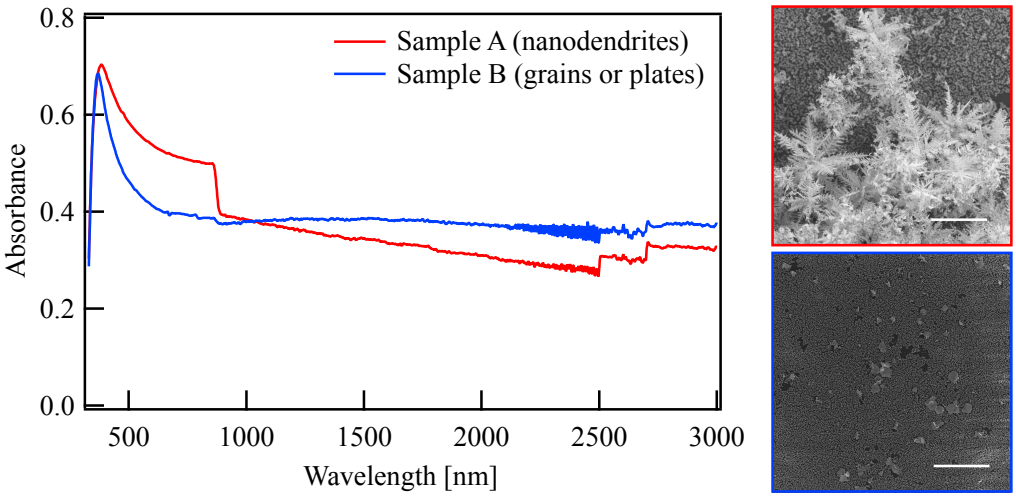

Figure 2.18| Absorption spectra of silver nanostructures. Red line and blue line correspond to Sample A (nanodendrites) and Sample B (grains or plates), respectively. SEM images on the right side of the spectra show silver nanostructures observed on Sample A (red flame) and Sample B (blue flame).

irradiated to each sample and absorbance was measured. By comparing Sample A and Sample B, I attempted evaluating absorption characteristics of the nanodendrites. A seed-substrate was used as a reference.

Figure 2.18 shows measured absorption spectra. Red line and blue line correspond to the spectra of Sample A and Sample B, respectively. SEM images at the right side of the spectra were taken from Sample A (red flame) and Sample B (blue flame), respectively. There are some ramps around 900 nm, 2500 nm, and 2700 nm on the spectra. Those are caused by operations of the spectrophotometer such as transition of detector. Handling of stray light changes at the operations, which bring the ramps. Since the samples used have nonflat surface and the refractive index may vary along the wavelength (the details are discussed in Chapter 3), the stray light is inevitable. There also is interference fringe originating in glass substrate around 2000-2500 nm. In both Sample A and Sample B, the spectra are broadly spanning visible and near infrared region with a resonant peak on 386 nm. Size variation of the nanostructures on each sample can be one of the origin of the broad spanning behavior. The spectrum of Sample A has a slight decreasing curve along increase of wavelength, which seems to be derived from the nanostructures of Sample 1 such as the nanodendrites. Since there are nanostructures other than the nanodendrites such as plates, it is hard to conclude the behavior on the absorption spectrum as a characteristic of the nanodendrites.

Another method is conceivable to understand the optical characteristics of the nanodendrites: observation of scattering light from a nanodendrite. It is interesting if the scattering property changes with incident direction or polarization of light.

Summary

The mechanism of dendrite growth was described. The driving force of crystal growth is the difference of chemical potentials between phases of materials, and proportional to supersaturation. A high driving force enough to overcome an energy wall derived from interface tension is needed to form a crystal nucleus. Thermal fluctuation on concentration gradient of the solute makes bumps on the surface of crystals. The bumps with the size corresponding to critical wavelength where the effects of diffusion field and interfacial tension are in a balance grow further toward directions with small interfacial stiffness, and become needle-like crystals. The same phenomenon occurs around the surface of the needle-like crystals, making them dendritic crystals. The balance between diffusion of the solute and the velocity of crystal growth is important to form the concentration gradient. A method of silver nanodendrite growth from substrates utilizing SPR heating on the surface of silver nanoparticles (seeds) excited by UV light was proposed. Seed-substrates were prepared by fixing the seeds onto the surface of glass substrates via surface modification. The silver nanodendrites were grown from the seeds through reduction of silver ion with a reductant. Nondestructive extraction of three-dimensional silver nanostructures was demonstrated with CO_2 supercritical fluid for washing and drying. We have analyzed laser power dependency on structural characteristics for nondeformed silver nanostructures. Correlation between experimental parameters other than laser power and the shapes of silver nanostructures were studied, and the conditions for nanodendrite growth was uncovered. For practical use of the developed method, we have grown the nanostructures in transparent matrix. We used agarose gel and successfully grew silver nanodendrites in it, and extracted the structures with supercritical fluid drying. Fractal dimension and absorption of the nanodendrites were discussed.

One of future perspectives is enlarging the area of nanostructure growth with plasmonic heating. In-plane area can be expanded as UV illumination area enlarges. To increase the height, stacking layers of nanostructures is effective. With the present method, nanostructures rise until exhausting silver ions in solution. However, lateral growth also occurs, leading to collision with adjacent trees. To prevent the collision, nano-seeds should be sparsely dispersed on the substrate. Other metals rather than silver can be used as the materials of

nanostructures grown with the developed method, while operating frequency range is different from that of silver. Gold and copper have been used for nano-tree growing with electrochemical deposition and chemical de-alloying respectively [36,37]. Another possible application of this large-scale materials with nanostructures would be the perfect absorber in a wide spectral range between UV to IR, with a wide range of viewing angle due to their fractal geometry and three-dimensionality of the structures.

Appendixes

Detail of procedure of silver nanodendrite growth from silver seeds with plasmon heating

1. Silver nitrate ($AgNO_3$) acetone solution and an L-ascorbic acid (LAA) acetone solution were prepared. $AgNO_3$ and LAA actually were difficult to solve in acetone. Hence, a $AgNO_3$ aqueous solution (2 M) and an LAA aqueous solution (1.2 M) were prepared at first. Subsequently, the $AgNO_3$ aqueous solution was mixed in acetone, and the LAA aqueous solution was mixed in acetone. Finally, the $AgNO_3$ acetone solution and the LAA acetone solution were prepared.
2. A seed-substrate prepared in Section 2.2 was placed onto a cooling stage, and its temperature was kept below 0 ℃. A droplet of the $AgNO_3$ acetone solution (2 μL) and the LAA acetone solution (2 μL) were separately put onto the surface of a seed-substrate, and kept for 60 secs to cool them. Finally, these droplets were merged with a micropipet.
3. A UV laser light (λ = 355 nm, CW) was directly conducted onto the surface of the seed-substrate from the bottom without any lenses. The merged droplet was irradiated for 20 secs to process oxidation-reduction reaction. After the irradiation, the remained droplet was washed and dried with CO2 supercritical fluid. In the case of Section 2.4, the droplet was washed with liquid acetone and the deposit of silver nanostructures reduced onto the seed-substrate was dried with air.

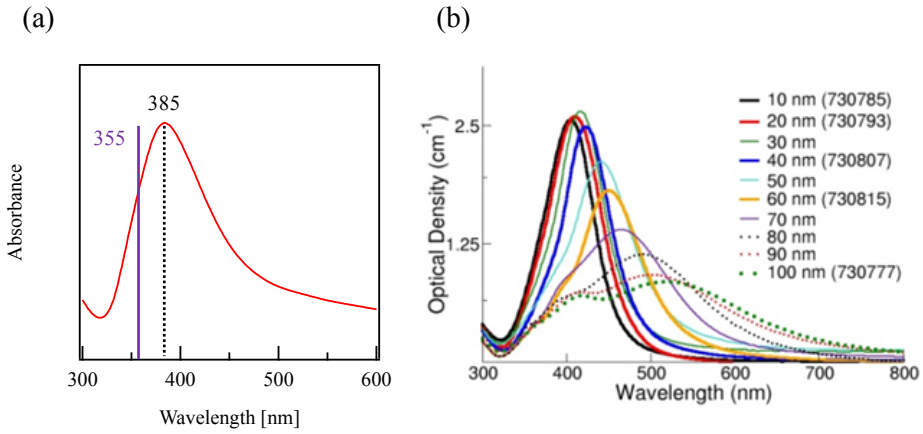

Figure A2.1| (a) The absorption spectrum of the prepared silver seed aqueous solution. The purple line at 355 nm indicates the wavelength of incident laser for SPR of the seeds. (b) A series of absorption spectra of silver nanoparticles along different diameters. Figure (b) referred from [40].

Experimental procedure of silver seed preparation

1. An $AgNO_3$ aqueous solution (0.5 mM, 125 mL), a sodium citrate aqueous solution (0.5 mM, 125 mL), and a sodium borohydride ($NaBH_4$) aqueous solution (1 mM, 12.5 mL) were prepared.
2. The sodium citrate aqueous solution was mixed into the $AgNO_3$ aqueous solution and stirred enough. The $NaBH_4$ aqueous solution was then dropped into the mixed aqueous solution and stirred enough. The prepared silver seed aqueous solution presented dark yellow color. The absorption spectrum of the seed aqueous solution showed that the seeds had an absorption on 385 nm of wavelength (Fig. A2.1 (a)), which indicated that the diameters of the seeds were below 10 nm (Fig. A2.1 (b)) [38].

Experimental procedure of seed-substrate preparation

1. Plasma cleaning (100 mW, 2 min) of the surface of a glass substrate was conducted to expose hydroxyl groups on the surface.

2. 3-aminopropyltrimethoxysilane was mixed into ethanol (1v/v%) and stirred enough. The glass substrate was immersed in the 3-aminopropyltrimethoxysilane ethanol solution for 1 hr, washed enough with ethanol after immersion, and dried with argon gas enough.
3. The substrate was immersed in the seed aqueous solution prepared with the procedure shown above for 6 hrs, washed enough with pure water, and dried with argon gas enough.
4. Plasma cleaning (100 mW, 20 sec) of the surface of the substrate was conducted to remove remained amino groups and expose hydroxyl groups on the surface again.
5. A dichlorodimethylsilane toluene solution (0.01v/v%) was prepared. The substrate was immersed in the solution for 1 hr, washed enough with toluene after immersion, and dried in air enough.

References

[1] 上羽牧夫, 結晶成長のダイナミクスとパターン形成 (培風館, 東京, 2008).
[2] 上羽牧夫, 結晶成長のしくみを探る −その物理学的基礎− (共立出版, 東京, 2002).
[3] Y. Saito, *Crystal Growth*, 4 ed. (Shokabo, Tokyo, 2013).
[4] 黒田登志夫, 結晶は生きている (サイエンス社, 東京, 2010).
[5] Abukawa Lab., http://surfphys.tagen.tohoku.ac.jp/surface_menu/ideal-surface (2011).
[6] C. Yang, X. Cui, Z. Zhang, S. W. Chiang, W. Lin, H. Duan, J. Li, F. Kang, and C.-P. Wong, Nature Communications **6**, 8150 (2015).
[7] L. Wang, H. Li, J. Tian, and X. Sun, ACS Appl. Mater. Interfaces **2**, 2987 (2010).
[8] M. H. Rashid and T. K. Mandal, J. Phys. Chem. C **111**, 16750 (2007).
[9] X. Wen, Y.-T. Xie, W. C. Mak, K. Y. Cheung, X.-Y. Li, R. Renneberg, and S. Yang, Langmuir **22**, 4836 (2006).
[10] X. Zheng, L. Zhu, X. Wang, A. Yan, and Y. Xie, Journal of Crystal Growth **260**, 255 (2004).
[11] W. Liu, T. Yang, J. Liu, P. Che, and Y. Han, Ind. Eng. Chem. Res. **55**, 8319 (2016).
[12] C. L. Liang, K. Zhong, M. Liu, L. Jiang, S. K. Liu, D. D. Xing, H. Y. Li, Y. Na, W. X. Zhao, Y. X. Tong, and P. Liu, Nano-Micro Lett **2**, (2010).
[13] Z. Yi, S. Chen, Y. Chen, J. Luo, W. Wu, Y. Yi, and Y. Tang, Thin Solid Films **520**, 2701 (2012).
[14] H. Xu, M. Shao, T. Chen, Y. Zhao, and S.-T. Lee, J. Raman Spectrosc. **43**, 396 (2011).
[15] S. Xie, X. Zhang, D. Xiao, M. C. Paau, J. Huang, and M. M. F. Choi, J. Phys. Chem. C **115**, 9943 (2011).
[16] H. You, C. Ding, X. Song, B. Ding, and J. Fang, CrystEngComm **13**, 4491 (2011).
[17] J. Fang, H. You, P. Kong, Y. Yi, X. Song, and B. Ding, Crystal Growth & Design **7**, 864 (2007).

[18] J. Fang, H. You, C. Zhu, P. Kong, M. Shi, X. Song, and B. Ding, Chemical Physics Letters **439**, 204 (2007).
[19] J. Fang, X. Ma, H. Cai, X. Song, B. Ding, and Y. Guo, Appl. Phys. Lett. **89**, 173104 (2006).
[20] H. J. Yin, Z. Y. Chen, Y. M. Zhao, M. Y. Lv, C. A. Shi, Z. L. Wu, X. Zhang, L. Liu, M. L. Wang, and H. J. Xu, Nature Publishing Group **5**, 1 (2015).
[21] Y. Fei Chan, C. Xing Zhang, Z. Long Wu, D. Mei Zhao, W. Wang, H. Jun Xu, and X. M. Sun, Appl. Phys. Lett. **102**, 183118 (2013).
[22] W. Ye, C. Shen, J. Tian, C. Wang, C. Hui, and H. Gao, Solid State Sciences **11**, 1088 (2009).
[23] M. N. Nadagouda, T. F. Speth, and R. S. Varma, Acc. Chem. Res. **44**, 469 (2011).
[24] M. Tsuji, M. Hashimoto, Y. Nishizawa, M. Kubokawa, and T. Tsuji, Chem. Eur. J. **11**, 440 (2005).
[25] R. He, X. Qian, J. Yin, and Z. Zhu, Chemical Physics Letters **369**, 454 (2003).
[26] K. A. Homan, J. Chen, A. Schiano, M. Mohamed, K. A. Willets, S. Murugesan, K. J. Stevenson, and S. Emelianov, Adv. Funct. Mater. **21**, 1673 (2011).
[27] Y. Zhou, S. H. Yu, C. Y. Wang, X. G. Li, Y. R. Zhu, and Z. Y. Chen, Adv. Mater. **11**, 850 (1999).
[28] M. R. Langille, M. L. Personick, and C. A. Mirkin, Angew. Chem. Int. Ed. **52**, 13910 (2013).
[29] E. Kondo, in *Supercritical Fluid Technology in MEMS and Semiconductor Processing*, edited by E. Kondo (CORONA Publishing, Tokyo, 2012), pp. 1–39.
[30] K. Tajiri, K. Igarashi, and T. Nishio, J. Non-Cryst. Solids **186**, 83 (1995).
[31] J. J. Jasper, Journal of Physical and Chemical Reference Data **1**, 841 (1972).
[32] E. Heidaryan, T. Hatami, M. Rahimi, and J. Moghadasi, J. Supercrit. Fluids. **56**, 144 (2011).
[33] K. Kaneko, H.-B. Sun, X.-M. Duan, and S. Kawata, Appl. Phys. Lett. **83**, 1426 (2003).
[34] M. M. Hossain and M. Gu, Laser Photonics Rev. **8**, 233 (2014).
[35] S. Shoji, H.-B. Sun, and S. Kawata, Appl. Phys. Lett. **83**, 608 (2003).
[36] T.-H. Lin, C.-W. Lin, H.-H. Liu, J.-T. Sheu, and W.-H. Hung, Chem. Commun. **47**, 2044 (2011).
[37] X. Liu, S.-F. Zhao, Y. Shao, and K.-F. Yao, RSC Adv. **4**, 33362 (2014).
[38] S. J. Oldenburg, https://www.sigmaaldrich.com/technical-documents/articles/materials-science/nanomaterials/silver-nanoparticles.html (2017).

Chapter 3.
Finite-difference time-domain analysis

In this chapter, I discuss electromagnetic responses of silver nanodendrites by simulation. Finite-difference time-domain (FDTD) method was applied. At first, I show characteristic peaks of scattering spectrum of a silver nanodendrite model and corresponding oscillation modes of the nanodendrite. Spectral differences among parameters such as the geometry of the nanodendrite are also discussed. Finally, potentials of the silver nanodendrites as metamaterials are discussed in a context of negative refractive index.

3.1 Scattering spectra of silver nanodendrite model

As with other silver nanoparticles, one can obtain resonance characteristics of silver nanodendrites from scattered light if the dendrites have the resonances with incident light. In this term, I conducted FDTD simulations of the nanodendrites to study optical responses. I especially expected that parts composed by adjacent branches was able to react with magnetic field, because the parts might be able to act as resonators [1]. Lumerical FDTD Solutions was utilized for the simulation.

The simulation model of the silver nanodendrites is described in Fig. 3.1. Each parameter was decided based on an actual silver nanodendrite, and the trunk and branches were approximated as silver nanorods. Although the nanodendrite is self-similar, I considered such a simplified model for the aim to understand fundamental electromagnetic responses of the nanodendrite. Palik's material database was applied as optical constants [2]. The nanodendrite was located in a vacuum. An $x-y-z$ coordination was defined as shown in right bottom of Fig. 3.1, and the center of the nanodendrite model was defined as the origin of the coordinate. We used a mesh with a spatial resolution of 2.5 nm with refinement by conformal variant on the area of the nanodendrite [3]. Total-field scattered-field (TFSF) source, which

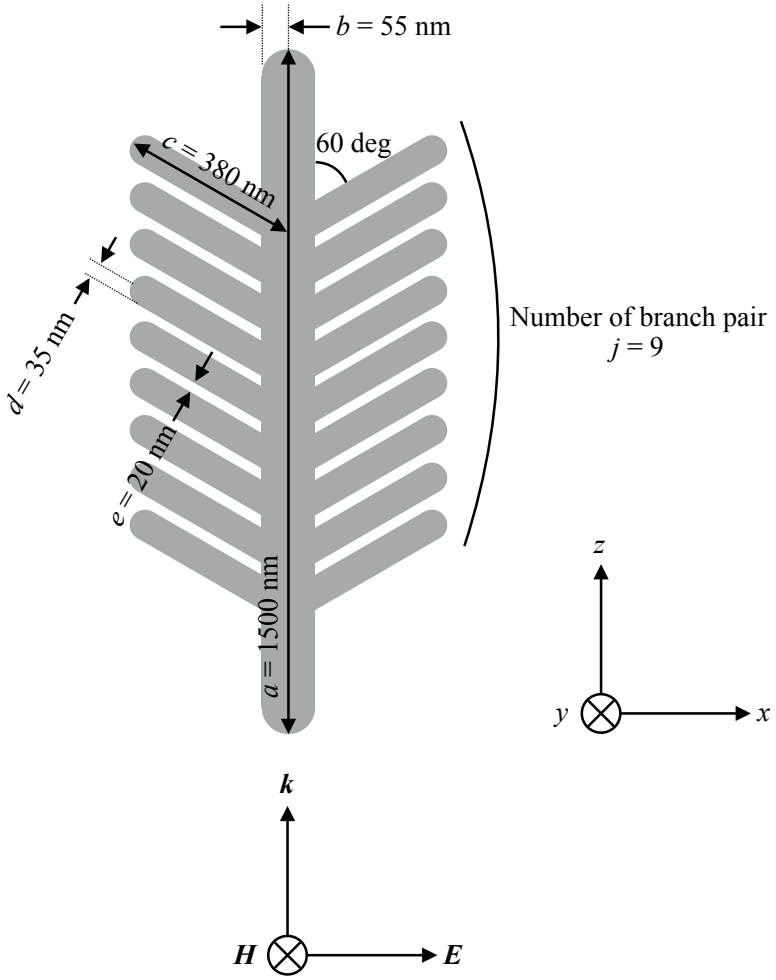

Figure 3.1| A model of silver nanodendrites for FDTD simulation with definition of the $x-y-z$ coordination as shown in the right bottom image.

is used to separate the computation region into a region containing the total field (the sum of the incident field and the scattered field) and another region containing only the scattered field, was applied as the incident field [4]. The incident field was a plane pulse wave, and the range of wavelength and the electric field amplitude were 300-3000 nm and unit respectively. The magnetic field of the incident field directed to y axis. All the scattered fields from the nanodendrite were detected with the surface of a rectangular object surrounding the nanodendrite. The rectangular object was outside of the TFSF source, so the incident field was not detected. Each surface of the rectangular object was separated from the nanodendrite (more than 3000 nm corresponding to the maximum wavelength of the incident field) not to detect near fields of the nanodendrite. Perfect matching layer (PML), which suppressed reflection of electromagnetic fields, was applied as the boundary condition.

Figure 3.2 shows a scattering spectrum from the silver nanodendrite with the incident field entering from the bottom along $+z$ direction. There is a large peak at 2000 nm of wavelength. There are also three small peaks between 300-700 nm of wavelength. The output electric field intensity distribution of the nanodendrite at these peaks are shown in Fig. 3.3. There are strong electric field distributions at apexes of branches and gaps between adjacent branches. The electric field distributions tend to be fine as the wavelength of the incident

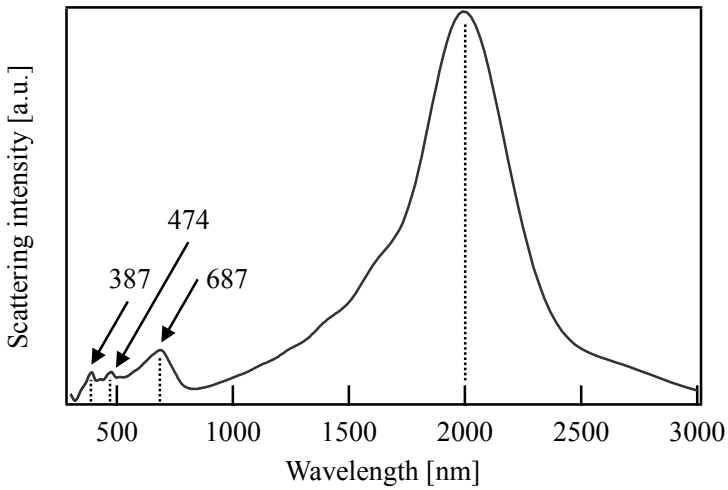

Figure 3.2| A scattering spectrum from the silver nanodendrite model defined in Fig. 3.1.

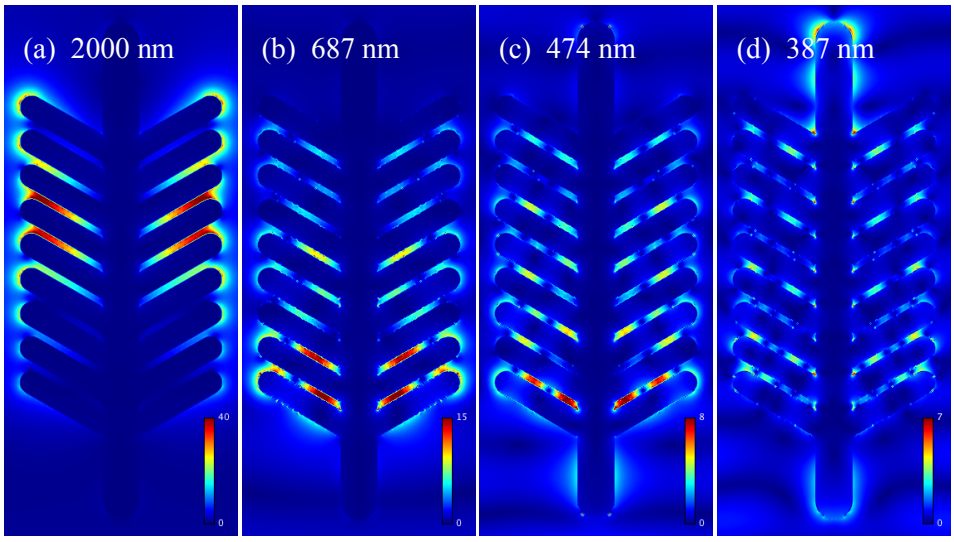

Figure 3.3| Magnitude distributions of output electric field from the silver nanodendrite model corresponding to each peak at 2000 nm (a), 687 nm (b), 474 nm (c), and 387 nm (d) on the scattering spectrum shown in Fig. 3.2.

field is small as seen in Fig. 3.3 (b), (c), and (d). This result indicates that the nanodendrite has high order oscillation modes of 2000 nm of wavelength.

3.2 Magnetic response of silver nanodendrite model

In this section, magnetic responses of the nanodendrite on the oscillation mode of the peak at 2000 nm of wavelength is discussed. At first, output magnetic field distributions of the nanodendrite and the amount of change of the incident magnetic field where on the same area where the nanodendrite is located are shown in Fig. 3.4. The distributions of Figs. 3.4 (a) and (b) are cases of the phase $2n\pi$ and $(2n+1)\pi$ respectively where $n = 0, 1, 2, \cdots$. The magnetic field has the component only along y axis, no component along x and z axes. Colors represent the direction of the magnetic field: red and blue correspond to $+y$ and $-y$ respectively. In both Figs. 3.4 (a) and (b), the directions of the output magnetic field and the incident magnetic field are opposite with each other. Hence, the phase between them differ in π with each other. The output magnetic field in Fig. 3.4 thus seems to be generated by current in the nanodendrite induced by the incident field. It is obvious that electromotive force of electromagnetic induction is proportional to the amount of change of incident magnetic field, and the current flows toward the direction to reduce the amount of change.

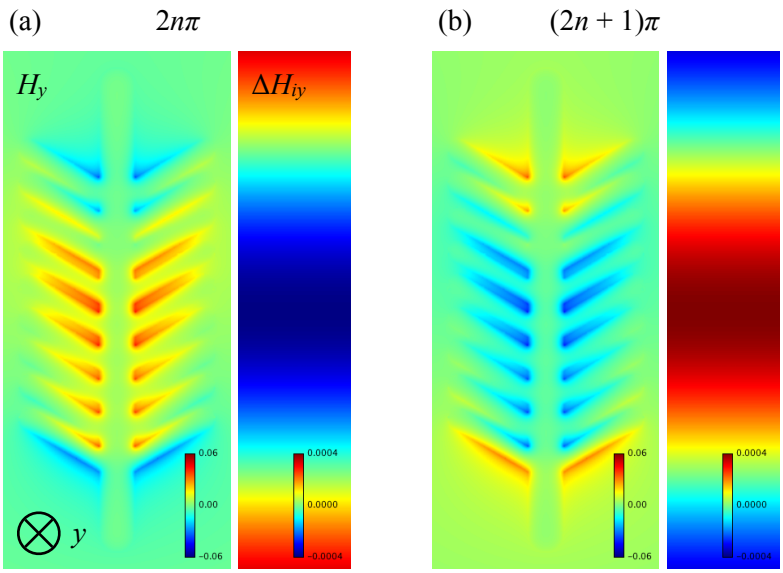

Figure 3.4| Distributions of output magnetic fields H_x and amount of change of incident fields ΔH_{ix} at phases $2n\pi$ (a) and $(2n+1)\pi$ (b).

Which direction of the induced current of the nanodendrite? Figure 3.5 describes distributions of the induced current density generated by the incident field. In this calculation, the silver nanodendrites was regarded as the cloud of free electron [5]. The induced current has components along x and z axes, no component along y axis. Colors represent the direction of the induced current: red and blue correspond to + and – directions respectively regarding x and z axes. As shown in the distribution of $\boldsymbol{J}_x$ of Fig. 3.5, the current does not flow from branches to other branches beyond the trunk. The current also has especially high density at roots of the branches. By combining the distributions of $\boldsymbol{J}_x$ and $\boldsymbol{J}_z$, it can be understood that the current flow between the adjacent branches as described in bottoms of Fig. 3.5 (a) and (b).

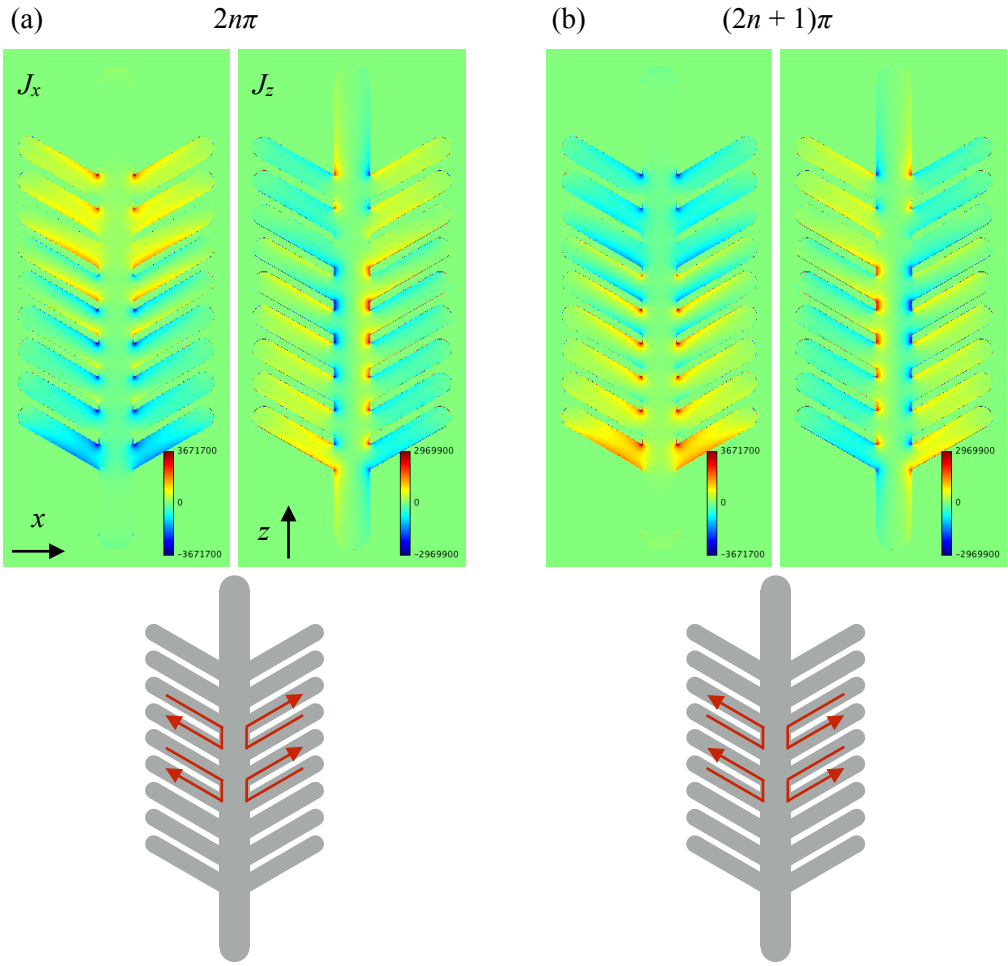

Figure 3.5| Induced current density distributions at phases $2n\pi$ (a) and $(2n+1)\pi$ (b). The current has components $\boldsymbol{J}_x$ and $\boldsymbol{J}_z$ corresponding to x and z axes. Red arrows in schematics at bottom of (a) and (b) indicate the direction of the current at each phase.

The direction of the current is opposite between the cases of $2n\pi$ and $(2n+1)\pi$. The direction of the output magnetic field generated by the current corresponds to that shown in Fig. 3.4. As a result, the induced current flows to suppress the amount of change on the incident magnetic field.

3.3 Permittivity, permeability, and refractive index of silver nanodendrite model

In this chapter, it is proved by FDTD simulation that silver nanodendrites can interact with induced magnetic field. The nanodendrites can also react with induced electric field. Hence, effective permeability, effective permittivity, and refractive index can be changed by the nanodendrites. In this section, these optical properties of a nanodendrite are discussed. From complex reflectance and complex transmittance, those properties are retrieved. Here, I firstly describe the method of the retrieval [6,7].

Retrieval from complex reflectance and transmittance

A slab and two incident waves from each side of the slab are considered in this method as described in Fig. 3.6 (a). The slab is composed by an assemble of a structure interacting with electromagnetic field. The complex reflectance and transmittance from each incident wave are considered. The incident waves a_1, a_2, and the output waves b_1, b_2 are related as below

$$\begin{bmatrix} b_1 \\ b_2 \end{bmatrix} = \begin{bmatrix} S_{11} & S_{12} \\ S_{21} & S_{22} \end{bmatrix} \begin{bmatrix} a_1 \\ a_2 \end{bmatrix}. \tag{3.1}$$

The 2×2 matrix in the middle is called as *S*-parameter which relates incident waves and output waves such as scattered wave and transmitted wave (Fig. 3.6 (b)). Each component of the *S*-parameter is regarded as complex reflectance or complex transmittance. In the case of the left of Fig. 3.6 (b), for example, S_{11} and S_{21} are the complex reflectance and the complex transmittance of the incident a_1 respectively. The *S*-parameter simplifies the relation between the incident waves and the output waves.

There are some important parameters for using the *S*-parameter: the size of the unit cell of the structure, homogeneity and the thickness of the slab. If the size of the unit cell in the slab is smaller enough than the wavelength and the slab is homogeneous, the whole slab can be regarded as an effective medium. Hence, the slab is symmetric along propagation

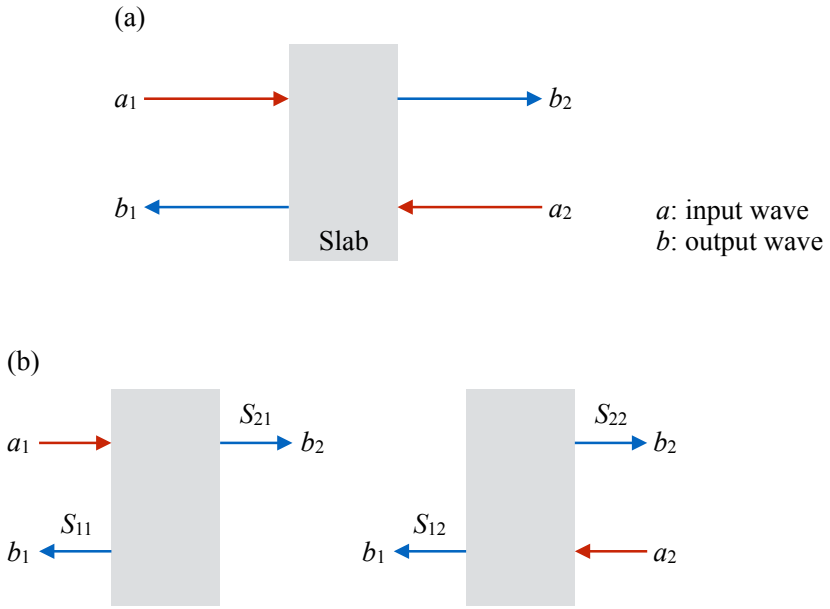

Figure 3.6| (a) A slab and input waves from both sides of the slab. Output waves, reflected and transmitted waves, are also shown. (b) Relations between components of *S*-parameter and input/output waves.

direction of light, which leads to $S_{11} = S_{22}$. When the thickness of the effective-medium slab d is smaller enough than the wavelength, the complex refractive index n and the wave impedance Z of the slab is described with the components of the *S*-parameter as below

$$n = \frac{1}{kd}\cos^{-1}\left\{\frac{1}{2S_{21}}\left(1 - {S_{11}}^2 + {S_{21}}^2\right)\right\} + \frac{2\pi m}{kd}, \tag{3.2}$$

$$Z = \pm\sqrt{\frac{(1+S_{11})^2 - {S_{21}}^2}{(1-S_{11})^2 - {S_{21}}^2}}, \tag{3.3}$$

where k and m are wavenumber of the incident wave and an integer. Existence of the branches $2\pi m/kd$ in Eq. (3.2) bring ambiguity on determination of the real part of the refractive index. If the slab is passive, $\mathrm{Im}(n) > 0$ and $\mathrm{Re}(Z) > 0$ are required. These requirements identify the sign of $\mathrm{Re}(n)$ and Z. If the unit size is not small enough than the wavelength, the slab becomes inhomogeneous for light. If the slab is asymmetric along propagation direction of light, in addition, $S_{11} \neq S_{22}$. In this case, the complex refractive index n and the wave impedance Z of the slab is described as below instead of Eqs. (3.2) and (3.3),

$$n = \frac{1}{kd}\cos^{-1}\left\{\frac{1}{2S_{21}}\left(1 - S_{11}S_{22} + {S_{21}}^2\right)\right\} + \frac{2\pi m}{kd}, \tag{3.4}$$

$$Z = \pm\frac{1}{2T_{21}}\left\{(T_{22}-T_{11}) \mp \sqrt{(T_{22}-T_{11})^2+4T_{12}T_{21}}\right\}, \tag{3.5}$$

where

$$\begin{aligned}
T_{11} &= \frac{1}{2S_{21}}\{(1+S_{11})(1-S_{22})+S_{21}S_{12}\}, \\
T_{12} &= \frac{1}{2S_{21}}\{(1+S_{11})(1+S_{22})-S_{21}S_{12}\}, \\
T_{21} &= \frac{1}{2S_{21}}\{(1-S_{11})(1-S_{22})-S_{21}S_{12}\}, \\
T_{22} &= \frac{1}{2S_{21}}\{(1-S_{11})(1+S_{22})+S_{21}S_{12}\}.
\end{aligned} \tag{3.6}$$

The two roots of Eq. (3.5) correspond to the two directions of wave propagation. The permittivity and the permeability of the slab are retrieved by the relations shown as below

$$\varepsilon = \frac{n}{Z}, \quad \mu = nZ. \tag{3.7}$$

Due to the difference of the sign of the root in Eq. (3.5) along the directions of wave propagation, the permittivity and the permeability of the slab may differ with propagation direction of light when the slab is asymmetric.

Calculation with model of silver nanodendrite

Here, I discuss permittivity, permeability, and refractive index derived from a model of silver nanodendrite. As shown in Fig. 3.7, the nanodendrite model was periodically aligned two-dimensionally in $x-y$ plane with the gaps Δx and Δy between adjacent structures in a vacuum, which formed a slab infinitely spreading in $x-y$ plane. Each dimension of the nanodendrite model was the same as Fig. 3.1. Pulsed-white light with the wavelength 300-3000 nm and the propagation direction of $+z$ was induced from the bottom of the slab. The amplitude and the phase of reflected light and transmitted light from the slab was detected at the $x-y$ planes located with the distance 4000 nm above and below the center of the slab. Then, complex values of the reflectance and transmittance, S_{11} and S_{21}, were obtained. The case of propagation direction $+z$ was also done with the same way to obtain S_{22} and S_{12}. The length of the stem of the structure a is 1500 nm, which is not subwavelength for the induced white light. A subwavelength size should be at least one fourth of the wavelength [8]. Hence, the nanodendrite slab is inhomogeneous and asymmetric due to the structure of

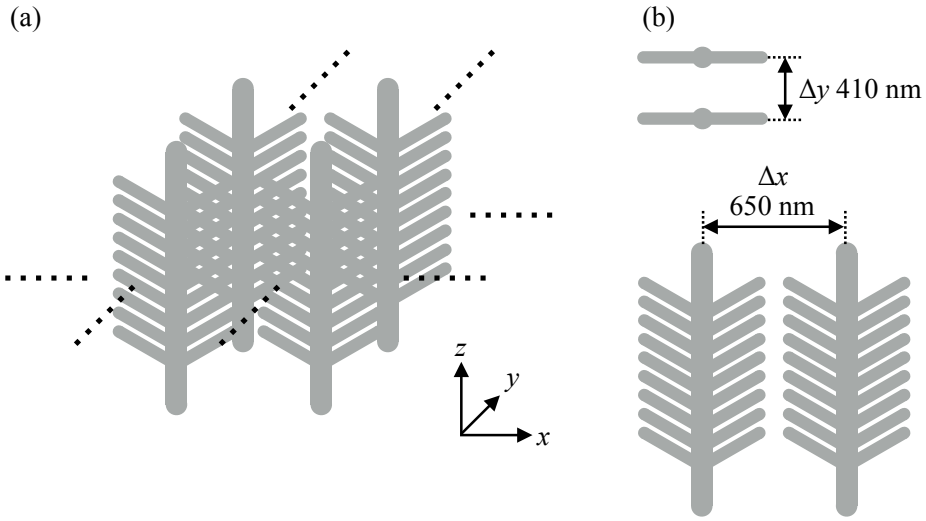

Figure 3.7| A model of slab composed of silver nanodendrites. (a) shows the configuration of the nanodendrites. Structures are periodically aligned along x and y axes indicated at the right-bottom of (a). The pulsed-white light irradiates along $+z$ direction. (b) shows the gaps Δx and Δy between adjacent structures.

the nanodendrite. For this reason, Eqs. (3.4) and (3.5) were chosen to calculate refractive index and wave impedance. Since the nanodendrite model is not subwavelength, diffraction can occur. In this term, only zeroth order diffracted light was extracted the analysis of this section. A discussion regarding the analysis with all the diffracted light appears in Appendixes of this chapter.

Figures 3.8 (a) and (b) show wavelength characteristics of complex values of permeability and permittivity obtained from the nanodendrite slab, respectively. As described above, the permeability and the permittivity may differ along the propagation direction of incident light. Here, only the case of the propagation $+z$ is discussed for simplification, as they consequently are the same in the propagations $+z$ and $-z$. As shown in Fig. 3.8 (a), there is a peak of the imaginary part near 1500 nm and the real part changes up and down around the peak. This behavior shows a magnetic resonance of the nanodendrite structure at the peak. The real part of the permeability has negative values on short-wavelength side of the resonance peak. It should be noted that the wavelength of magnetic response of the nanodendrite slab in Fig. 3.8 (a) and that of a unit-nanodendrite structure shown in the previous section are different with each other. This is because the resonance wavelength varies with the density of the nanodendrite model for composing the slab (see Appendixes of this chapter for the detail). In the case of the permittivity, the sign of the real part changes from positive to neg-

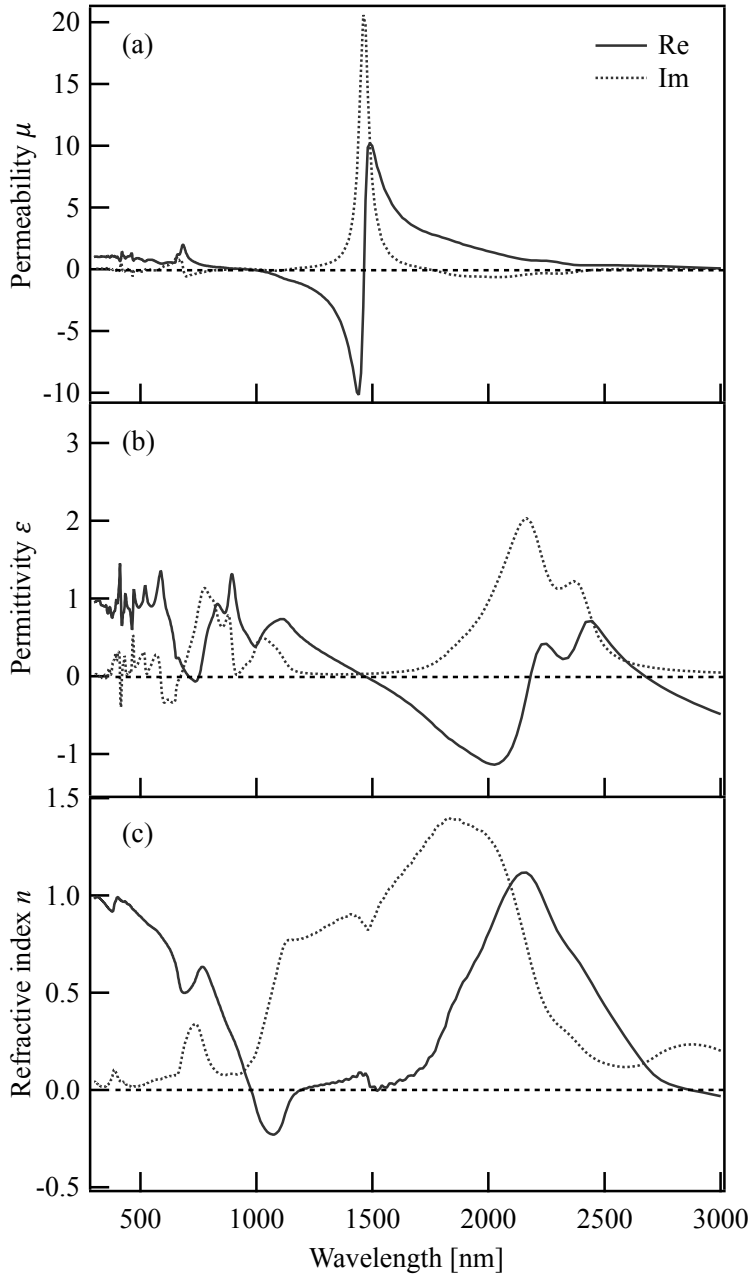

Figure 3.8| Characteristics of permeability (a), permittivity (b), and refractive index (c) of slab composed of silver nanodendrites. The solid line and the dotted line in each figure represent the real part and the imaginary part of those optical parameters, respectively.

ative around 1000-2000 nm as shown in Fig. 3.8 (b). The real value at the peak of the magnetic resonance is ~0.01, and the sign of the value on short-wavelength side of the peak is positive. From Figs. 3.8 (a) and (b), hence, the real parts of the permittivity and permeability of the slab are not negative simultaneously.

Figure 3.8 (c) shows a wavelength characteristic of complex refractive index of the nanodendrite slab. Around the wavelength of the magnetic response, the real part has values near zero. The imaginary part around 1000-2000 nm is larger than the real part, which means relatively higher absorption than other wavelength regions. The real part also has an area of negative value around 1000 nm. This behavior seems to be derived from both the real parts and the imaginary parts of the permeability and permittivity, not only from the real parts of them. The complex refractive index is described as below

$$\begin{aligned} n &= n_1 + in_2 \\ &= \sqrt{(\varepsilon_1\mu_1 - \varepsilon_2\mu_2) + i(\varepsilon_1\mu_2 + \varepsilon_2\mu_1)} \\ &= \left\{(\varepsilon_1\mu_1 - \varepsilon_2\mu_2)^2 + (\varepsilon_1\mu_2 + \varepsilon_2\mu_1)^2\right\}^{\frac{1}{4}} \left\{\cos\left(\frac{\theta}{2} + k\pi\right)\right. \\ &\qquad \left. + i\sin\left(\frac{\theta}{2} + k\pi\right)\right\}, \end{aligned} \tag{3.7}$$

where

$$\begin{gathered} \varepsilon = \varepsilon_1 + i\varepsilon_2\,, \qquad \mu = \mu_1 + i\mu_2\,, \\ \theta = \tan^{-1}\left(\frac{\varepsilon_1\mu_2 + \varepsilon_2\mu_1}{\varepsilon_1\mu_1 - \varepsilon_2\mu_2}\right), \\ 0 \le \theta < 2\pi\,, \\ k = 0, 1\,. \end{gathered} \tag{3.8}$$

The requirement $\mathrm{Im}(n) > 0$ determines the value of k, which determines the sign of $\cos(\theta/2 + k\pi)$. Depending on each component of ε and μ, the real part of the refractive index can be negative. In this case, the real parts of the permeability and the permittivity do not have to be negative simultaneously. The large imaginary part of the refractive index represents high absorption, which is undesirable for negative-index metamaterials. The imaginary part should be near zero as much as possible. To achieve this situation, it is desired that the real parts of the permeability and the permittivity is simultaneously negative and the imaginary parts of those is near zero. However, it is valuable that negative permeability and negative index of the nanodendrite model was unveiled. The branches $2\pi m/kd$ of the refractive index given by Eq. (3.4) were chosen with different integer m along different wavelength regions to make the value of the refractive index continuous along full wavelength 300-3000 nm (see Appendixes of this chapter for the detail).

3.4 Scattering characteristics among geometrical parameters

Transitions of the peak at 2000 nm on the scattering spectra among the geometrical parameters *a*-*e* and *j* of the silver nanodendrite model were studied. Only a parameter was varied from the origin, while the other parameters were kept as original values. The peak at 2000 nm can be derived from the oscillation of the resonator composed of adjacent branches. If the geometry of the resonator is changed, the peak will surely change.

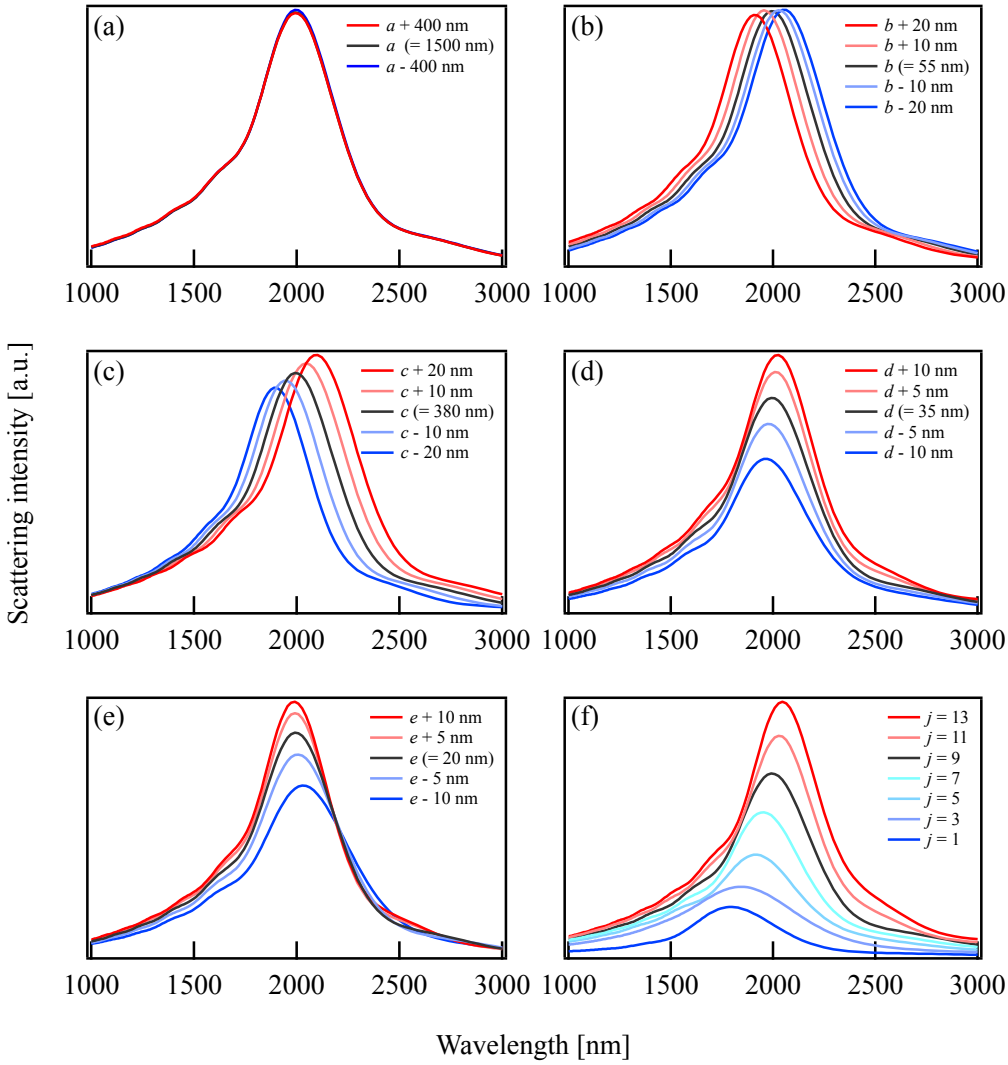

Figure 3.9| Scattering spectra of silver nanodendrite models among various numbers of geometry parameters. The spectra among different numbers of each parameter *a*-*e* and *j* are shown on (a)-(f) respectively.

A series of scattering spectra among the parameter *a*-*e* and *j* with different number are shown in Fig. 3.9. As one can see in Fig. 3.9 (a), there is no change on the spectra. This is because the geometry of the resonator is not changed with the parameter *a*. In Fig. 3.9 (b), on the other hand, the location of the peak varies with the radius of the trunk *b*. The increase of the number of *b* reduce the length of the resonator, making the position of the peak blue shift. In contrast, the decrease of the number of *b* increase the length of the resonator, making the position of the peak red shift.

The radius of the branches *c* also affects the appearance of the peak as shown in Fig. 3.9 (c). On increase of the parameter *c*, the intensity of the peak increases and the position red shifts. On decrease of the parameter *c*, on the other hand, the intensity of the peak decreases and the position blue shifts. The length of the resonator is proportional to the parameter *c*. Hence, it is obvious that the appearance of the peak depends on the parameter *c*. The radius of the branches *d* affects the intensity of the peak rather than its position as shown in Fig. 3.9 (d). Note that the number of the gap between adjacent branches *e* is kept 20 nm. The increase of the parameter *d* increases the peak intensity and slightly red shifts the peak position, while the decrease of the parameter *d* decreases the peak intensity and slightly blue shifts the peak position.

The gap between adjacent branches *e* and the number of branch pair *j* also affects the peak intensity as shown in Figs. 3.9 (e) and (f). On increase of the parameter *e*, the intensity of the peak increases. On decrease of the parameter *e*, the intensity of the peak decreases and the position red shifts. The increase of the parameter *j* makes the peak intensity increase and the peak position red shift, while the decrease of the parameter *j* makes the peak intensity decrease and the peak position blue shift.

In summary, the appearance of the peak depends on the parameters *b*-*e* and *j* which influence the geometry of the resonator composed by the adjacent branches. Since having no influence to the geometry of the resonator, the appearance of the peak is independent of the parameter *a*. The results indicate that the optical response of actual nanodendrites spans broadly, because the geometry widely differs with self-similarity.

3.5 Scattering and oscillation behaviors with different incident direction

As described in Section 3.2, the adjacent branches of the silver nanodendrite model can interact with the incident light and behave as resonators. Here, the same analysis result with

another direction of the incident light was carried out to confirm resonance excitation on the adjacent branches. The incident light had a wavenumber vector toward x axis, and the nanodendrite model was irradiated from the left distant place. The incident magnetic field

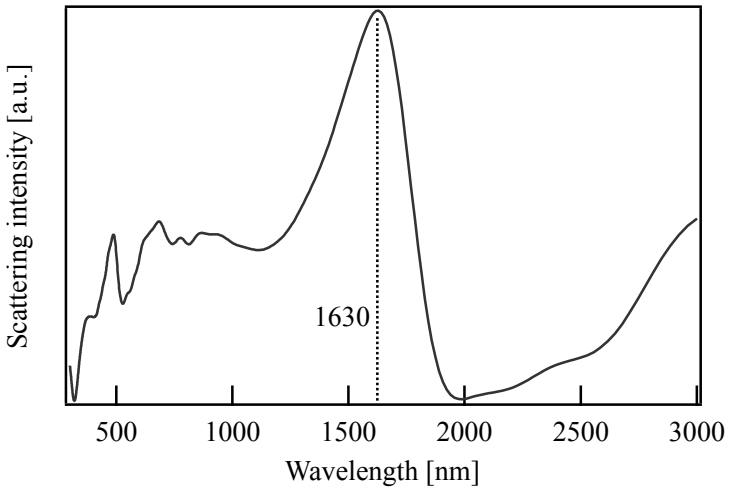

Figure 3.10| A scattering spectrum from the silver nanodendrite with the incident field along x axis.

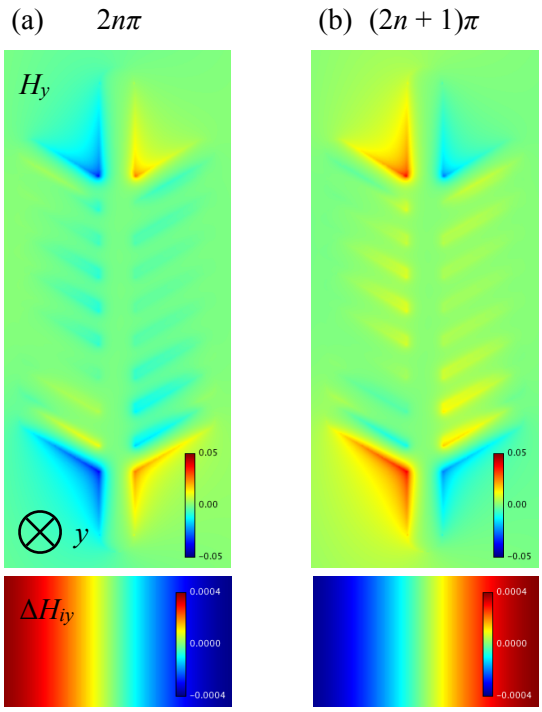

Figure 3.11| Distributions of output magnetic fields H_x and amount of change of incident fields ΔH_{ix} with incident field along x axis at phase $2n\pi$ (a) and $(2n+1)\pi$ (b).

had y component which was normal to the plane of the nanodendrite model. The other parameters were all the same as those described in the first of Section 3.1.

The scattering spectrum obtained with these parameters are shown in Fig. 3.10. There is a peak at wavelength 1630 nm. Output magnetic field distributions of the nanodendrite and the amount of change of the incident magnetic field where on the same area where the nanodendrite is located are shown in Fig. 3.11. The distributions of Figs. 3.11 (a) and (b) are cases of the phase $2n\pi$ and $(2n+1)\pi$ respectively where $n = 0, 1, 2, \cdots$. In this case, the output magnetic field distributions exist on areas which consist of the trunk and the branches located at upper and lower parts rather than the adjacent branches of the nanodendrite model. In the same manner with Fig. 3.4, the directions of the output magnetic field and the incident

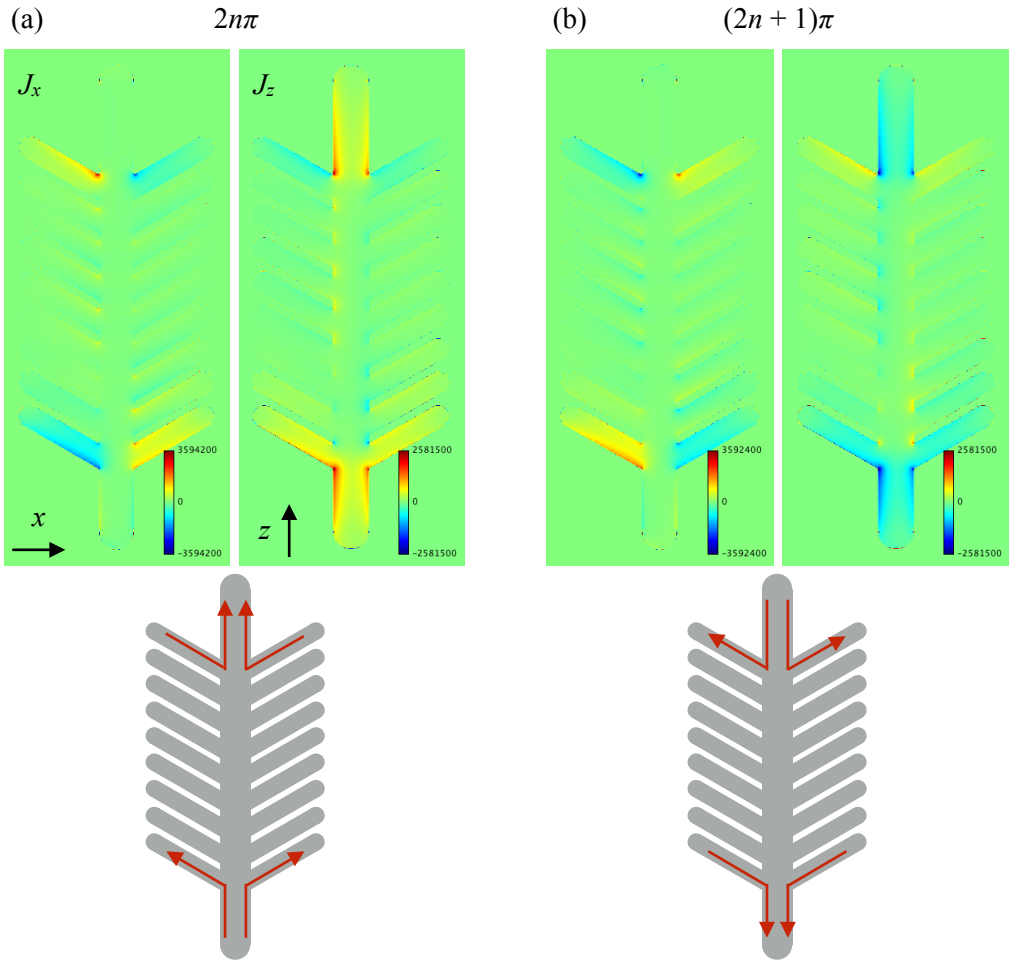

Figure 3.12| Induced current density distributions with incident field along x axis at phases $2n\pi$ (a) and $(2n+1)\pi$ (b). The current has components J_x and J_z corresponding to x and z axes. Red arrows in schematics at bottom of (a) and (b) indicate the direction of the current at each phase.

magnetic field are opposite with each other in both Figs. 3.11 (a) and (b). Hence, the phase between them differ in π with each other. The output magnetic field in Fig. 3.10 thus seems to be generated by current in the nanodendrite induced by the incident field.

Also, Fig. 3.12 shows distributions of the induced current density generated by the incident field. As shown in the distribution of J_x of Fig. 3.12, the current does not flow from branches to other branches beyond the trunk. The current also has especially high density at on upper and lower areas where the output magnetic distributions exist in Fig. 3.11. By combining the distributions of J_x and J_z, it can be understood that the current flow between the adjacent branches as described in bottoms of Figs. 3.12 (a) and (b). The direction of the current is opposite between the cases of $2n\pi$ and $(2n+1)\pi$. The direction of the output magnetic field generated by the current corresponds to that shown in Fig. 3.11. In the case of the light incidence along x axis, therefore, the induced current flows to suppress the amount of change on the incident magnetic field.

Summary

A model of silver nanodendrites for FDTD simulation was constructed based on actual nanodendrites. A scattering spectrum of the nanodendrite model had a peak at 2000 nm of wavelength, and three peaks around 400-700 nm corresponding to higher resonances than the 2000 nm peak. The model exhibited a magnetic response with an incident wave of wavelength 2000 nm. A current density analysis proved that current flew between adjacent branches with a direction which disturbed amplitude change of the incident wave. This result indicates that parts composed of the adjacent branches act as SRRs, and electromagnetic induction occurs on the parts. Permittivity, permeability, and refractive index originated from a nanodendrite model were discussed. These optical parameters were retrieved by analyzing complex values of reflectance and transmittance of a slab composed of periodically aligned nanodendrites. A magnetic resonance was clearly observed on the characteristic of the permeability, and the real part reached to negative near the resonant wavelength. The real part of the permittivity also reached to negative. The permeability and the permittivity, however, are not negative simultaneously. The real part of the refractive index reached to negative even the permeability and permittivity were not negative simultaneously, which was originated from both the real and imaginary parts of the permeability and the permittivity. Since the imaginary part of the refractive index was large at the area of the negative real part, high absorption was indicated. Appearance of the peak at 2000 nm changed among geometrical parameters of the dendrite model. The model showed a different resonance with a different

direction of the incident wave. The electromagnetic induction also occurred with the resonance.

Appendixes

Calculation considering all diffracted lights

Figure A3.1 shows the characteristic of permeability of silver-nanodendrite slab with use of all the diffracted light. Only the case of the propagation $+z$ is shown for simplification. Compared to Fig. 3.8, there is fluctuation on the lines of the permeability in Fig. A3.1. The behavior of magnetic resonance, however, still is observed at 1460 nm. This behavior is the same with propagation direction $-z$. The fluctuation also is observed on permittivity and refractive index. The general behavior of each optical parameter is obtained from the diffracted light of zeroth order.

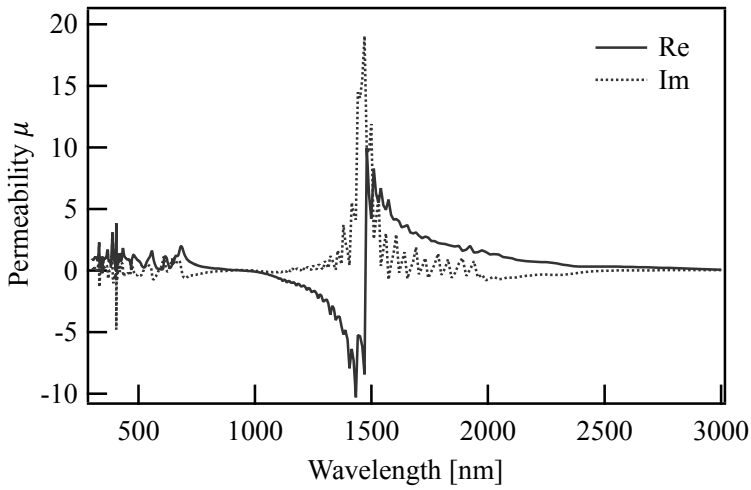

Figure A3.1| A characteristic of permeability retrieved from all diffracted lights of the slab composed of silver nanodendrites. The solid line and the dotted line represent the real part and the imaginary part, respectively.

Shift of optical characteristics along density of silver nanodendrite model

Figure A3.2 (a) shows the amplitude of reflectance and transmittance ($|S_{11}|$ and $|S_{21}|$) along different gaps of adjacent silver nanodendrites. With increase of the gaps Δx and Δy, the characteristic of the reflectance and transmittance becomes narrow, weak, and red-shifts. With sufficient gaps, the characteristic locates around the wavelength 2000 nm which is the same of magnetic response of a nanodendrite model discussed in section 3.1. Figure A3.2 (b) shows complex permeability along different gaps of adjacent silver nanodendrites. As increase of the gaps, the magnetic resonance red-shifts and almost vanishes with sufficient gaps. The results indicate that there is electromagnetic interaction between the nanodendrite models.

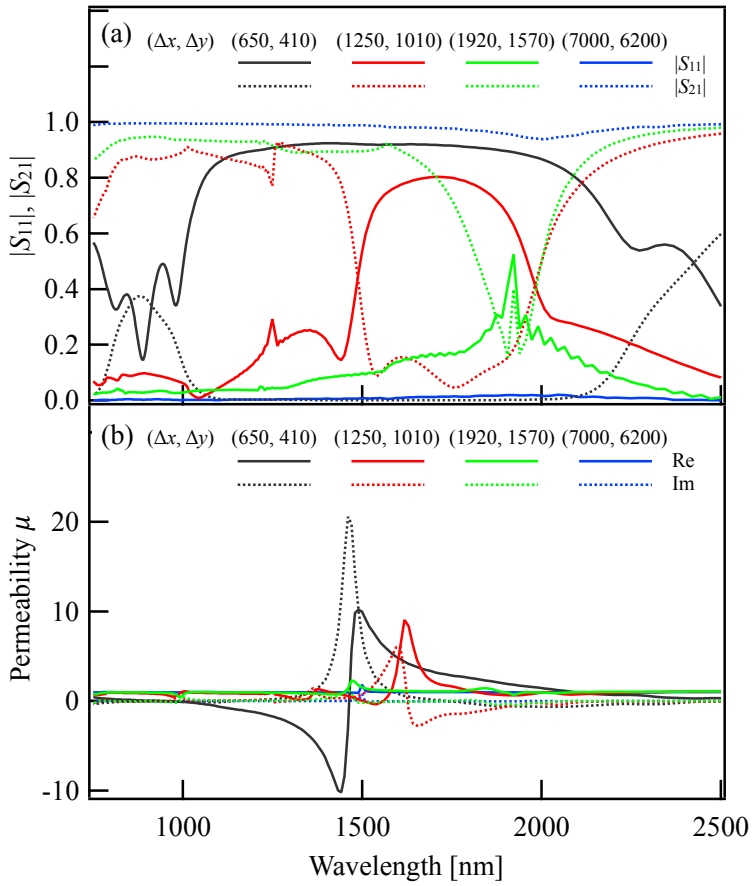

Figure A3.2| Amplitudes of reflectance and transmittance ($|S_{11}|$ and $|S_{21}|$) (a), and characteristics of permeability (b) along different gaps of adjacent silver nanodendrites composing slab. The solid lines and the dotted lines represent the reflectance and the transmittance in (a) respectively, and the real part and the imaginary part of the permeability in (b) respectively.

Determination of branches of refractive index

Figure A3.3 shows a characteristic of the real part of refractive index along different integer m of the term $2\pi m/kd$. The real part of the refractive index often has discontinuities which are physically incorrect if only one branch is chosen. Dotted-vertical lines divide the wavelength range at the wavelength where the discontinuities occur. To make the line of the refractive index continuous, appropriate branch should be chosen on each range of the wavelength [9,10]. In this term, at first, the branch of $m = 5$ at the left-most range in Fig. A3.3 was chosen as the criterion. At the wavelength 300 nm, the value of the branch $m = 5$ is the closest to 1 among the other branches. At 300 nm, silver is dielectric and the majority of the unit cell is vacuum. Hence, I anticipated that the refractive index was close to 1. The branch of the other ranges was chosen to make the line started from the branch $m = 5$ at the left-most range smooth along whole-wavelength region. Colored arrows in Fig. A3.3 point the lines chosen on each wavelength range. As a result, the line of the refractive index shown in Fig. 3.8 (c) was obtained. The refractive index was used for retrieving the permittivity and the permeability shown in Fig. 3.8 (a) and (b) respectively.

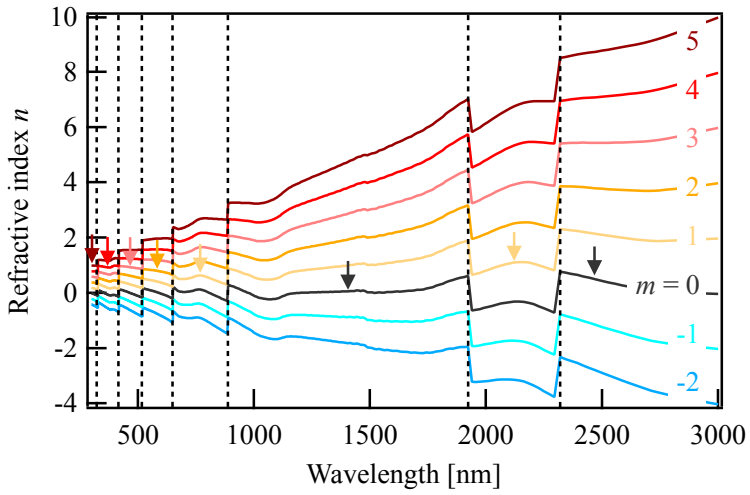

Figure A3.3| Characteristics of real parts of refractive index with different values of integer m of branch. The dotted lines divide the wavelength range at the wavelength where discontinuity of the refractive index occurs. the value shown in the right is the number of the integer m. Colored arrows point the lines chosen at each wavelength range divided with the dotted line.

References

[1] X. Zhou and X. Zhao, Appl. Phys. Lett. **91**, 181908 (2007).

[2] E. D. Palik, *Handbook of Optical Constants of Solids, Five-Volume Set* (Academic Press, Cambridge, 1997).

[3] Lumerical Inc., https://kb.lumerical.com/en/ref_sim_obj_mesh_refinement_options.html (2017).

[4] Lumerical Inc., https://kb.lumerical.com/en/ref_sim_obj_sources_tfsf.html (2017).

[5] Lumerical Inc., https://kb.lumerical.com/en/layout_analysis_charge_current.html (2017).

[6] D. R. Smith, S. Schultz, P. Markoš, and C. M. Soukoulis, Phys. Rev. B **65**, 195104 (2002).

[7] D. R. Smith, D. C. Vier, T. Koschny, and C. M. Soukoulis, Phys. Rev. E **71**, 036617 (2005).

[8] A. Ishikawa, in *Technology and Applications of Metamaterial*, edited by T. Ishihara (CMC Publishing, Tokyo, 2011), pp. 111–123.

[9] J. Zhou, T. Koschny, M. Kafesaki, and C. M. Soukoulis, Phys. Rev. B **80**, 035109 (2009).

[10] S. G. Tikhodeev, in *Technology and Applications of Metamaterial*, edited by T. Ishihara (CMC Publishing, Tokyo, 2011), pp. 90–101.

Chapter 4.
Three-dimensional nanofabrication via two-photon absorption

So far, I discussed a bottom-up optical 3D fabrication of metal nanostructures and their possibilities as metamaterials. On the other hand, top-down approaches are also beneficial to precisely fabricate intended structures. Although mass-fabrication is difficult, the top-down approaches are attractive because of capability of fabrication control. In this chapter, an overview of a top-down optical 3D nanofabrication method is provided. When we fabricate something with light, the fabrication resolution is basically limited due to existence of diffraction limit of light. Exploitation of multi-photon absorption can overcome the diffraction limit. Several materials such as polymers and metals can be used with this 3D nanofabrication. Metamaterials can be also prepared by this method.

4.1 Principle of three-dimensional nanofabrication

There is a 3D nanofabrication method with exploitation of two-photon absorption which is a nonlinear optical effect. Here, in this thesis, I call this method as two-photon fabrication (TPF). In 1997, Kawata and co-workers experimentally confirmed the principle of TPF with photo-curable resins [1]. In 2001, they achieved to fabricate a 3D microstructure with spatial resolution beyond diffraction limit [2]. The TPF realizes arbitrary 3D structural fabrication with spatial resolution beyond diffraction limit. Therefore, the TPF has been regarded as a powerful tool for nano/micro 3D fabrications.

Basically, photo-curable resins are widely used for the TPF. By accelerating polymerization locally with focusing a high-power laser, such a micro/nano fabrication is realized. Because of this characteristic, the TPF is also called as two-photon photo-polymerization fabrication or direct laser writing and so on. Besides the photo-curable resins, Metals [3-6] and

organic/inorganic hybrid materials via sol-gel method [7-9] are also able to be utilized for the TPF.

Two-photon absorption

Two-photon absorption is the key to achieve the nano/micro spatial resolution beyond diffraction limit of the TPF. The two-photon absorption is a nonlinear phenomenon which electrons of materials absorb two photons simultaneously on transition from the ground state to an excited state. The probability of the two-photon absorption is proportional to the second power of light intensity (photon density). The probability is usually very low, so the electrons absorb just one photon whose energy corresponds to the energy gap. Hence, a temporally and spatially high density of photon is needed for the two-photon absorption. Femto second (fs) pulse lasers are thus utilized.

Here, let us consider a liquid photo-curable resin with absorption at UV range. When the liquid resin absorbs energy corresponding to UV, the resin solidifies via polymerization. Now, we consider a fs pulse laser with near infrared wavelength. Since the energy of near infrared light is around the half of UV light, liquid resin basically is not solidified by the near infrared wavelength. When we focus the fs pulse laser onto the liquid resin, however, the two-photon absorption can occur only at the center of the focus spot. By earning the two-photon with energy corresponding to near infrared, the electrons obtain the energy corresponding to UV (Fig. 4.1). The liquid resin then can be solidified only at this area. The solidified area is confined to nanoscale in 3D, which is the reason why the TPF can realize subwavelength 3D fabrication (Fig. 4.2). By scanning the laser spot or the stage where the liquid resin is located, one can fabricate arbitral 3D structures.

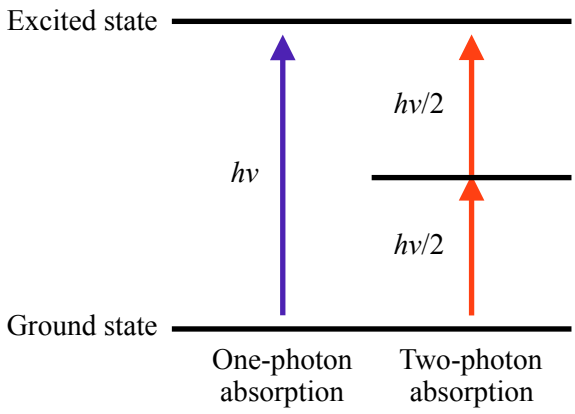

Figure 4.1| An energy diagram of one-photon absorption and two-photon absorption.

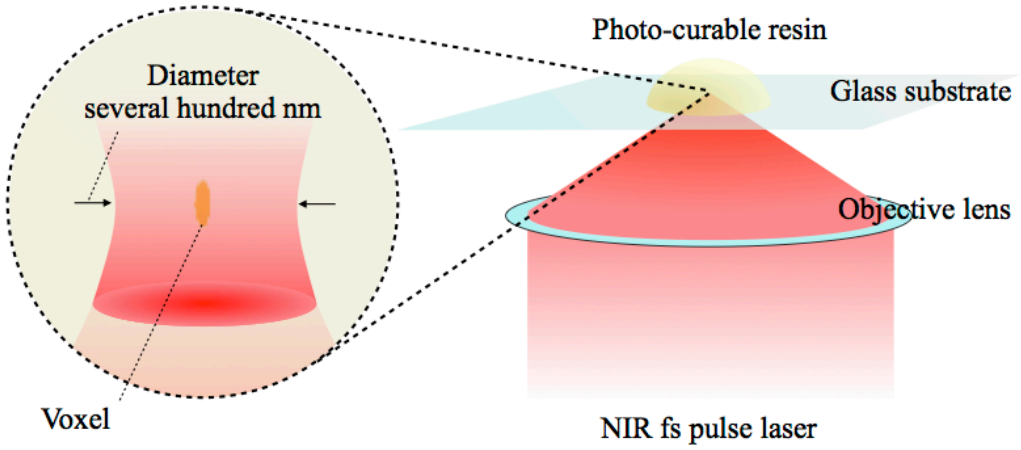

Figure 4.2| A schematic of TPF. A NIR fs pulse laser is focused onto a photo-curable resin located on a glass substrate. A voxel with the size beyond diffraction limit is formed in the focus spot.

Radical photo-polymerization

The liquid resin is solidified through radial photo-polymerization induced by the two-photon absorption. The liquid resin includes a monomer, an initiator, and a sensitizer. The procedure of reaction is described as follows,

$$\begin{aligned} \mathrm{I} &\longrightarrow 2\mathrm{R}\cdot, \\ \mathrm{R}\cdot + \mathrm{M} &\longrightarrow \mathrm{RM}\cdot, \\ \mathrm{RM_n}\cdot + \mathrm{M} &\longrightarrow \mathrm{RM_{n+1}}\cdot, \\ 2\left(\mathrm{RM_{n+1}}\cdot\right) &\longrightarrow \mathrm{RM_{2n}R}, \end{aligned} \tag{4.1}$$

where I, R ·, and M are the initiator, the radical, and the monomer. The initiator first absorbs photons and separates into two radicals. The initiator radical cut a double bond between two carbons of the monomer and make a covalent bond with the monomer. The radicalized monomer affects another monomer continuously, making ramified polymer chains. When the radicals react with each other, the radicals are inactivated and the reaction ceases. Through a series of the radical reactions, the liquid resin is solidified. The sensitizer absorbs the photons earlier than the initiator, and transfers the energy to the initiator.

4.2 Spatial resolution beyond diffraction limit

The spatial resolution of the TPF depends on the size of the resin solidified by the radical photo-polymerization induced by two-photon absorption as shown in Fig. 4.2. The minimum unit of the solidified resin is now called as *voxel*. The size of the voxel also depends on the size of the focus spot of the laser. In Fig. 4.3, a light intensity distribution around a focus spot with a wavelength 780 nm and an objective lens NA = 1.4 is shown [10]. On the focal plane and along the depth direction, the distribution of the two-photon absorption is proportional to the square of the light intensity. Hence, the size of the voxel on the two-photon absorption can be smaller than the size of the focus spot.

There is also a threshold on the light intensity for solidification of the liquid resin (Fig. 4.4). When the light intensity distribution of the two-photon excitation is larger than the threshold, the resin can be solidified and make the voxel. Also by adjusting other parameters such as the intensity of the laser and the width of the pulse, the size of the voxel can be reduced beyond 100 nm [11]. Recently, the idea of stimulated emission depletion (STED) microscopy [12-14] has been applied to the TPF [15,16]. A light illumination which induce STED to the excited initiator is applied with a donut shape around the focus spot of the TPF. The radicalized initiator via two-photon absorption is thus deactivated by the depletion light via STED before reaching the monomer. The radical photo-polymerization is deactivated on the STED area, thus allowing us to form smaller voxel compared to the normal TPF. Gu and coworkers exploited this technique in 2013 [17]. They succeeded to form a polymer wire with the diameter 9 nm (Fig. 4.5 (a)), and confirmed the spatial resolution 52 nm with a gap between two polymer wires (Figs. 4.5 (b) and (c)).

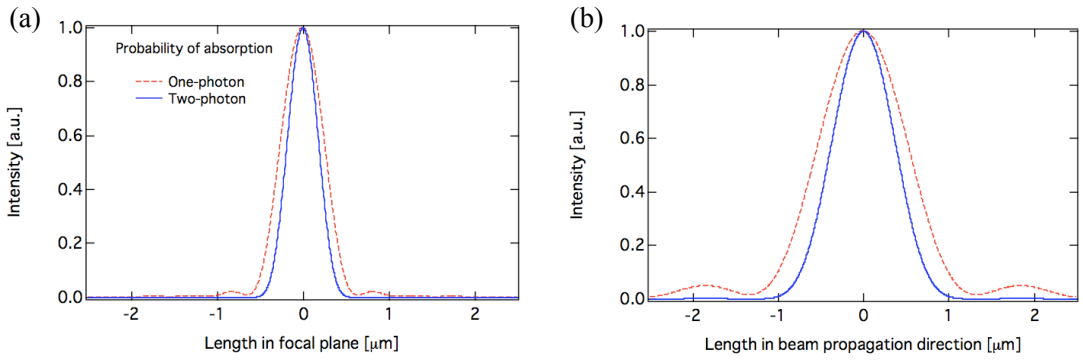

Figure 4.3| Probability of one-photon and two-photon absorption on a focal plane (a) and along propagation direction (b). Wavelength 780 nm, NA = 1.4. Figure referred from [10].

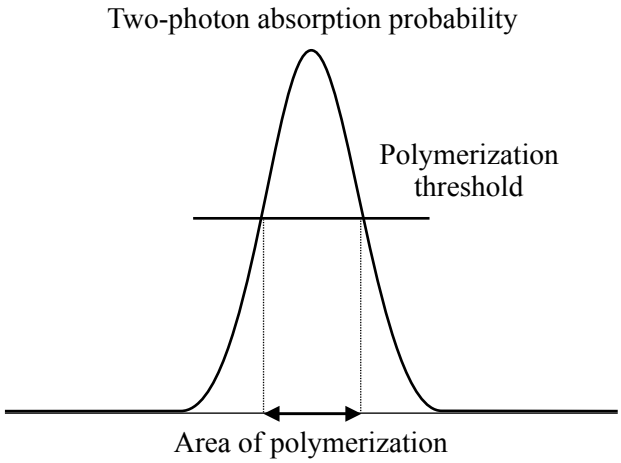

Figure 4.4| A schematic indicating a relation between the two-photon absorption probability and the polymerization threshold. The photo-polymerization occur on the area with the probability above the threshold.

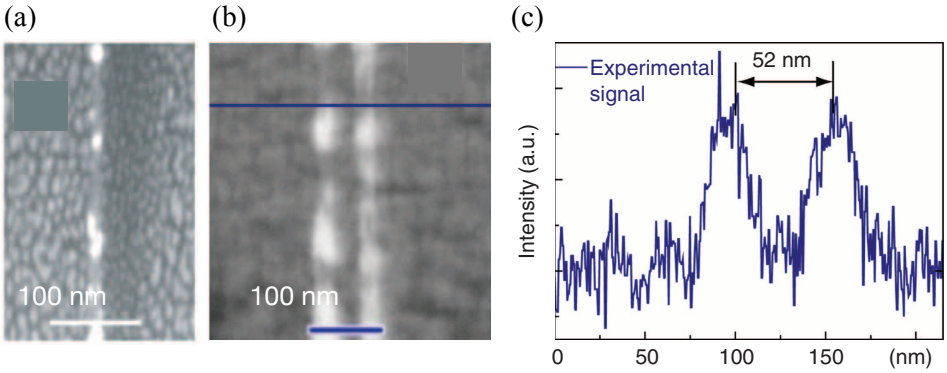

Figure 4.5| (a) A polymer wire with the diameter 9 nm, (b) adjacent polymer wires, and (c) a line profile of them. Those wires were formed by the TPF with STED. Figure referred from [17].

4.3 Applications of three-dimensional nanofabrication via two-photon absorption

TPF realizes arbitrary 3D structural fabrication with spatial resolution beyond diffraction limit. Therefore, the TPF has been regarded as a powerful tool for nano/micro 3D fabrications. Not only static structures, structures which have mechanical motions can be also fabricated

by the TPF. Some mechanical structures such as micro-gears and micro-tweezers as have been developed to date by the TPF (Figs. 4.6 (a) and (b) [18-21].

Metamaterials are one of the important applications of the TPF [3,6]. In this case, silver and gold are mainly applied instead of the resin. When the focused laser beam illuminates a silver ion solution, these metal ions absorb two photons simultaneously and they are reduced to metals. By scanning the laser spot or the stage, we can obtain arbitrary metal structures. Surfactants have been successfully applied to reduce the roughness of the structures and improve the spatial resolution around 100 nm. The metamaterials such as SRRs can be thus fabricated by this two-photon metal reduction (Figs. 4.6 (c) and (d)). This technique also allows us to stack the SRRs in 3D, which realizes a 3D metamaterial.

For the field of medical, the TPF has been applied to make a novel medical device such as microneedles (Fig. 4.6 (e)) [8,9]. Organic/inorganic hybrid materials have been used as the materials of the TPF. The Organic/inorganic materials are formed via sol-gel formation induced by TPF. The Organic/inorganic materials have higher physical strength than polymer because of their organic-inorganic covalent bonds, which is beneficial for micro medical devices. The young's modulus of an organic/inorganic material (Ormocer) is around 7.0 GPa [8], while that of poly(methyl methacrylate) is around 2.7 GPa [25].

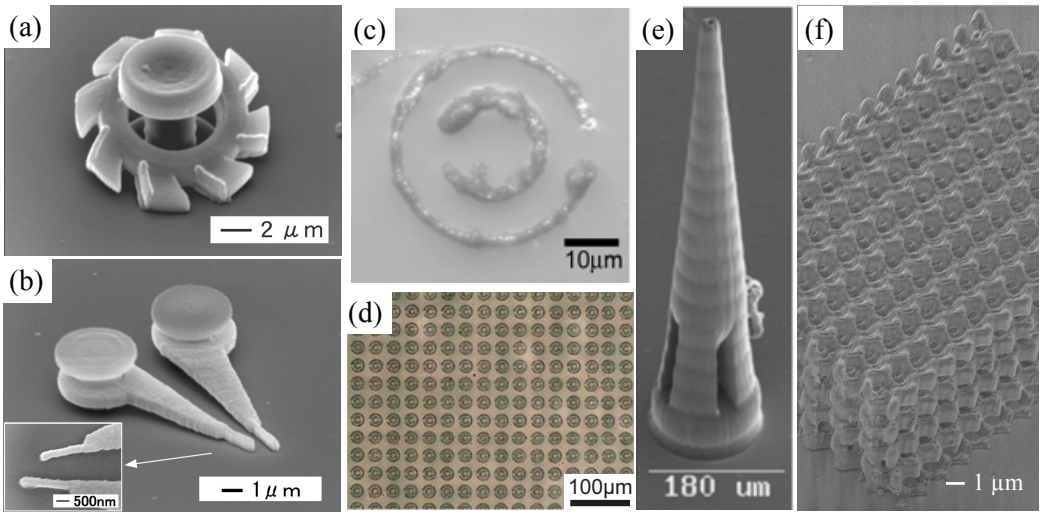

Figure 4.6| Applications of TPF. (a) a micro-gear and (b) a micro-tweezer as mechanical structures. (c) a silver SRR on a glass substrate and (d) a periodic gold SRRs assisted in poly(methyl methacrylate) as a host formed by two-photon induced reduction. (e) a microneedle made of an organic/inorganic hybrid ceramic. (f) a 3D photonic crystal. Figure (a)-(f) referred from [18,21,6,3,9,22] respectively.

Since the TPF is a universal technique for 3D micro/nano fabrication, it can be applied for various fields other than the above. Photonic crystals have been successfully developed by the TPF (Fig. 4.6 (f)) [22]. Optical memories with the TPF have been also studied [23,24].

Summary

In this chapter, I introduced fundamentals of a top-down 3D nanofabrication with two-photon absorption, TPF. Two-photon absorption can occur at the center of focus spot of fs pulse laser. Through radical photo-polymerization induced by the two-photon absorption, liquid resins are solidified only at the center of the focus spot. The two-photon absorption and existence of polymerization threshold realize fabrication resolution beyond diffraction limit, and STED technique can be applied to improve the resolution. The TPF can be applied in various fields which need nanofabrication. Metamaterials are one of the typical applications. SRRs with silver and gold can be fabricated via two-photon reduction.

References

[1] S. Maruo, O. Nakamura, and S. Kawata, Opt. Lett. (1997).
[2] S. Kawata, H.-B. Sun, T. Tanaka, and K. Takada, Nature **412**, 697 (2001).
[3] A. Ishikawa, A. Ishikawa, and T. Tanaka, IEEE J. Select. Topics Quantum Electron. **19**, 4700110 (2013).
[4] Y.-Y. Cao, X.-Z. Dong, N. Takeyasu, T. Tanaka, Z.-S. Zhao, X.-M. Duan, and S. Kawata, Appl. Phys. A **96**, 453 (2009).
[5] Y.-Y. Cao, N. Takeyasu, T. Tanaka, X.-M. Duan, and S. Kawata, Small NA (2009).
[6] T. Tanaka, J of Laser Micro/Nanoengineering **3**, 152 (2008).
[7] A. Ovsianikov, J. Viertl, B. Chichkov, M. Oubaha, B. MacCraith, I. Sakellari, A. Giakoumaki, D. Gray, M. Vamvakaki, M. Farsari, and C. Fotakis, ACS Nano **2**, 2257 (2008).
[8] A. Ovsianikov, B. Chichkov, P. Mente, N. A. Monteiro-Riviere, A. Doraiswamy, and R. J. Narayan, Int. J. Appl. Ceram. Technol. **4**, 22 (2007).
[9] A. Doraiswamy, C. Jin, R. J. Narayan, P. Mageswaran, P. Mente, R. Modi, R. Auyeung, D. Chrisey, A. Ovsianikov, and B. Chichkov, Acta Biomaterialia **2**, 267 (2006).
[10] S. Nakanishi, Two-Photon Fabrication of Polymer Nano-Device and Property Evaluation, 2007.
[11] D. Tan, Y. Li, F. Qi, H. Yang, Q. Gong, X.-Z. Dong, X. Dong, X.-M. Duan, and X. Duan, Appl. Phys. Lett. **90**, 071106 (2007).
[12] L. Schermelleh, R. Heintzmann, and H. Leonhardt, Journal of Cell Biology **190**, 165 (2010).

[13] S. W. HELL and J. WICHMANN, Opt. Lett. **19**, 780 (1994).
[14] T. A. Klar, S. Jakobs, M. Dyba, A. Egner, and S. W. HELL, Proceedings of the National Academy of Sciences of the United States of America **97**, 8206 (2000).
[15] L. Li, R. R. Gattass, E. Gershgoren, H. Hwang, and J. T. Fourkas, Science **324**, 910 (2009).
[16] J. Fischer and M. Wegener, Laser & Photonics Reviews **7**, 22 (2013).
[17] Z. Gan, Y. Cao, R. A. Evans, and M. Gu, Nature Communications **4**, 2061 (2013).
[18] S. Maruo, K. Ikuta, H. Korogi, and H. Korogi, J. Microelectromech. Syst. **12**, 533 (2003).
[19] S. Maruo and J. T. Fourkas, Laser & Photon. Rev. **2**, 100 (2008).
[20] S. Maruo, T. Hasegawa, and N. Yoshimura, Jpn. J. Appl. Phys. **48**, 06FH05 (2009).
[21] S. Maruo, K. Ikuta, and H. Korogi, Appl. Phys. Lett. **82**, 133 (2003).
[22] K. Kaneko, H.-B. Sun, X.-M. Duan, and S. Kawata, Appl. Phys. Lett. **83**, 2091 (2003).
[23] T. Tanaka and S. Kawata, Ieee Transactions on Magnetics **43**, 828 (2007).
[24] Y. Kawata, H. Ishitobi, and S. Kawata, Opt. Lett. **23**, 756 (1998).
[25] PMMAアクリル樹脂（物性表1）, http://www.kda1969.com/materials/pla_mate_pmma2.htm, (2016).

Chapter 5.
Three-dimensional polymer nanostructures formed by two-photon polymerization

Arbitrary 3D nanostructures can be fabricated by TPF. On the other hand, physical properties of nanosize polymers have still remains unclear. Some properties such as elastic moduli, which are one of material constants and should be independent of size, possess size dependence. This is because morphology of the polymer molecules can change due to spatial confinement. In this chapter, I discuss size dependent physical properties of polymer nanosprings consist of polymer nanowires formed by TPF. I also show size dependency of molecular orientation of the polymer nanowires. Then, I discuss correlation between the physical properties and the molecular orientation.

5.1 Size dependent elasticity of polymer nanosprings

In contrast to the progress on the TPF and its applications as I mentioned in Chapter 4, however, fundamental characteristics such as mechanical properties of nanosized polymer materials still have not understood in detail. Here, I discuss the mechanics of cross-linked poly(methyl methacrylate) (PMMA) nanowires formed into coil springs by the TPF. Hereafter, I refer the structures as polymer nanosprings. PMMA has been one of the most widely used polymers. There are some studies about the mechanical properties of PMMA of submicron size [1,2].

Fabrication of polymer nanosprings

Polymer nanosprings, at first, were formed by the TPF. Figure 5.1 (a) shows the dimensions of the structure. The coil radius, *R*, pitch, *P*, length of the spring, *L*, and the number of turns, *N*, are 2.5 μm, 2.0 μm, 13 μm, and 4, respectively. A bead with the radius 1.0 μm is attached at one end of the spring. Figure 5.1 (b) and (c) show a spring with the wire width 400 nm. The spring often deform when the wire width is narrower than 420 nm. Thus, an additional support was introduced as shown in Fig. 5.1 (d) to prevent the springs from deforming. With the additional support, nanosprings with a lateral wire width 188 nm at the thinnest point were fabricated. After fabrication, the supports were ablated with either a fs pulsed near-infrared (NIR) laser beam or a focused ion beam (FIB). The nanosprings were free-standing even

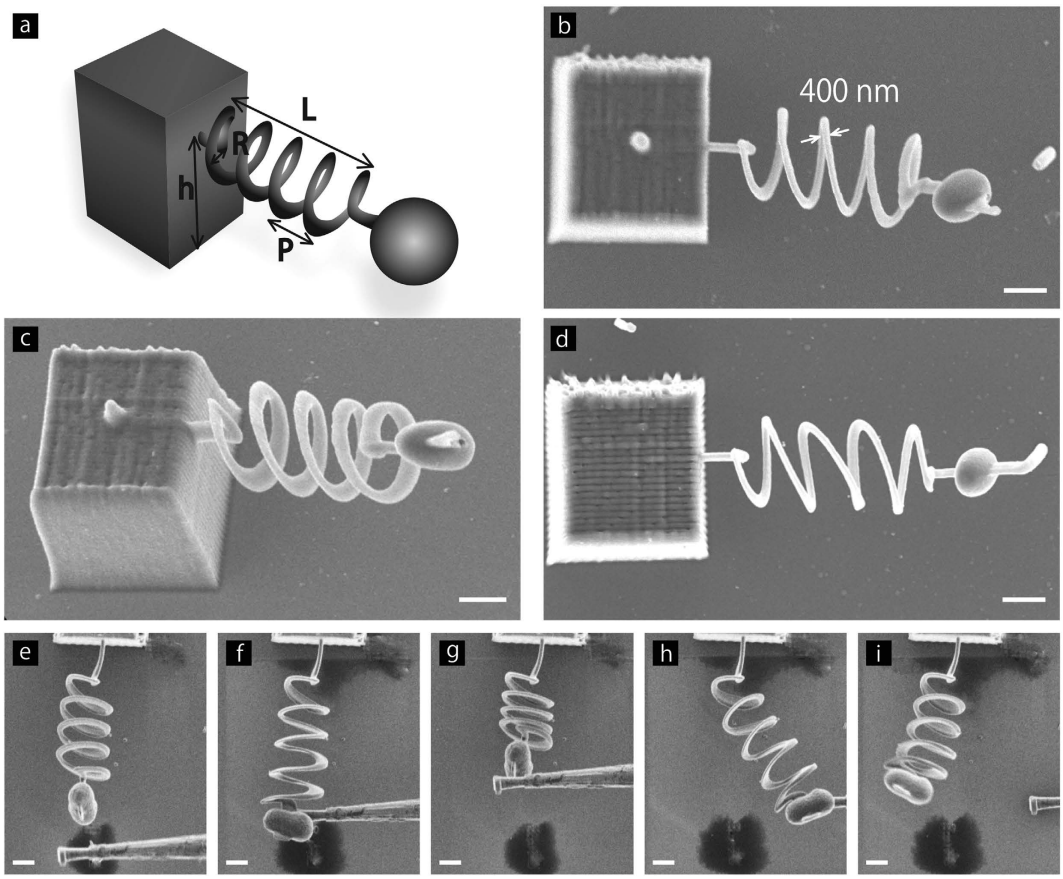

Figure 5.1| Polymer nanosprings fabricated by TPF. (a) A schematic showing the dimensions of the polymer nanosprings. (b), (c) Top and perspective SEM images of a polymer nanosprings, respectively. (d) SEM image of a nanospring with an additional support at the right side of a bead. (e)-(i) FIB images of the nanospring before loaded (e), stretched (f), compressed (g), bent (h), and recovered (i). All scale bars are 2μm.

after the removal of the supports, as shown in Figs. 5.1 (a)-(c). They showed properties of stretch, compress, bend, and recover against forces applied through a manipulator, which indicates that the spring behaves as a conventional spring (Figs. 5.1 (e)-(i)).

Compression of polymer nanosprings

To understand mechanical properties of polymer nanosprings, compression experiments of the springs were conducted. Vertically standing springs were prepared with the sizes as described above (the details appear in Appendix of this chapter). Figure 5.2 (a) shows a nanospring that stably and vertically stands without distortion and destruction. An atomic force microscope (AFM) were utilized for the compression experiments. Figure 5.2 (b) shows the procedure of the compression (see also Appendix). Note that the flat surface of the cantilever was used for pressing the nanosprings, not with the tip apex to put a force uniaxially to the spring and to avoid deformation of the bead. Figure 5.2 (c) shows a force curve that records the applied force on the cantilever with respect to the cantilever position. The force curve shows two slopes: (i) moderate slope in the range of z = 0 (initial position) to -840 nm where the cantilever contacts the spring alone (Fig. 5.2 (c), inset), and (ii) steep slope in the range of z = -840 to -1600 nm where the cantilever contacts both the spring and the glass substrate. There is no hysteresis on the moderate slope, which indicates no plastic deformation of the spring during the experiments. The moderate slope also indicates that the nanospring follows a linear response against the applied force, which also indicates that the nanospring obeys Hooke's law. In this moderate slope region, therefore, the system can be regarded as a series of two springs (Fig. 5.2 (d)). The spring constant of the nanospring k_s is given by the next equation

$$k_s = \left(\frac{1}{k} - \frac{1}{k_c} \right)^{-1}, \tag{5.1}$$

where k is an equivalent spring constant of the two springs. k is calculated as 0.10 N/m by fitting the moderate slope with a linear function. k_c is a spring constant of the AFM cantilever 13 N/m. By repeating compression tests on the same spring for more than 10 times, the

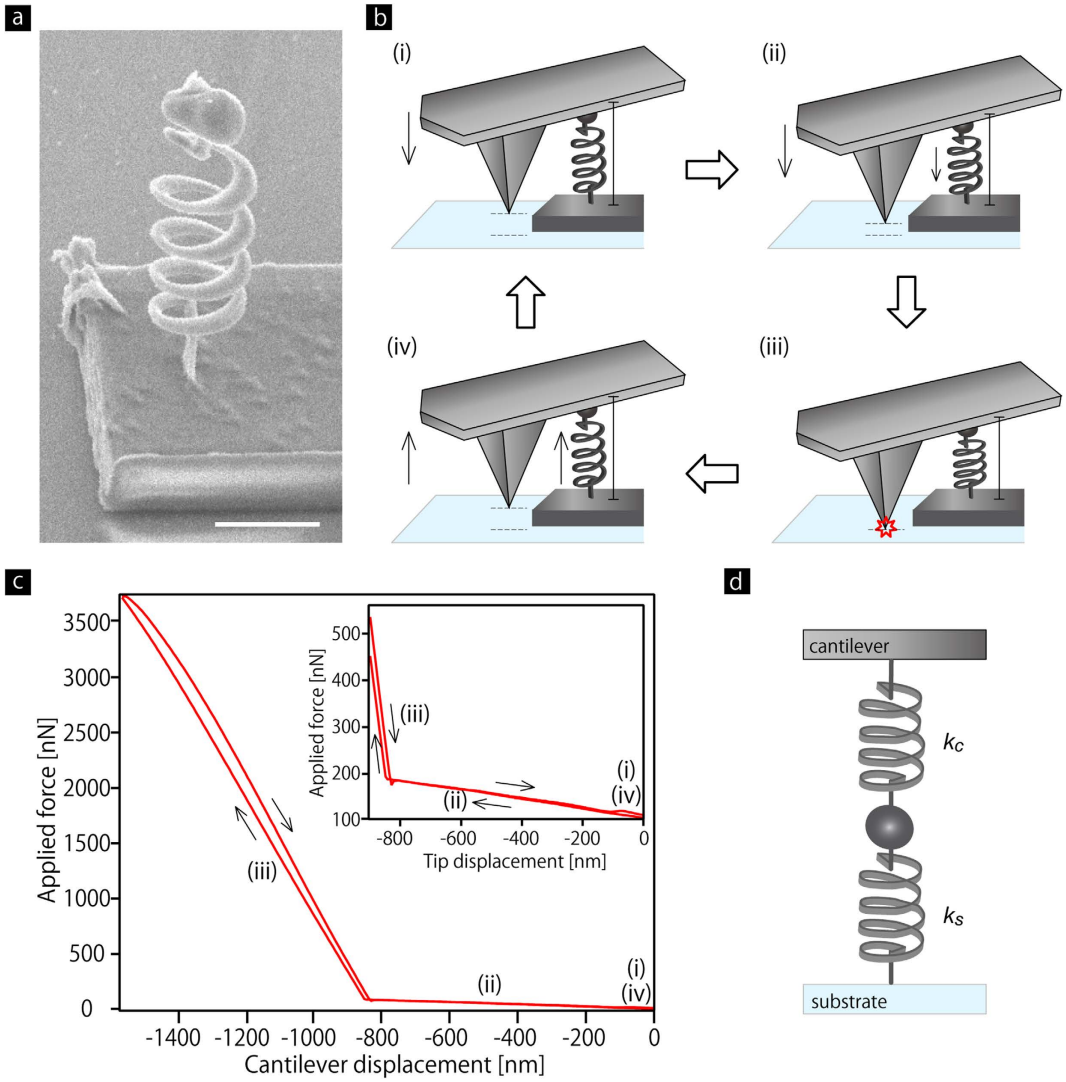

Figure 5.2| Compression experiments of polymer nanosprings with AFM. (a) A SEM image of a vertically free-standing polymer nanospring. The scale bar is 5 μm. (b) The procedure of compression using the AFM. (c) A force curve obtained from a spring showing the applied force on the cantilever with respect to the position. The annotations in the graph correspond to the schematic of (b). The inset in (c) is an enlarged graph in the region of 0 to -800 nm showing a moderate slope. (d) A schematic showing the system regarded as a series of two springs. k_s and k_c are the spring constant of the polymer spring and that of the AFM cantilever, respectively.

average spring constant with the standard deviation was obtained. Since there is no plastic deformation of the spring, the compression tests are reproducible.

Size effect on elastic modulus of polymer nanosprings

The spring constant k_s with different wire radius r was investigated to deeply understand the physical properties of polymer nanosprings. r is defined as $r = \sqrt{r_l r_v}$, where r_l and r_v are lateral and vertical radii. These were measured from SEM images of a set of straight nanowires (Figs. 5.3 (a) and (b)). By fabricating nanowires with different laser intensity, r as a function of the laser intensity was obtained (Fig. 5.3 (c)). The error bars describe non-uniformity of wire width, and the solid lines are fitting curves [3]. The compression experiments were carried out with several coil springs with different r in the range of 350 to 550 nm. Figure 5.3 (d) shows k_s as a function of r, showing that k_s increases as r decreases. The spring constant is theoretically described as follow

$$k_s = \frac{Gr^4}{4NR^3}, \tag{5.2}$$

where G is the shear modulus of the material, and the coil radius R = 2.5 μm, the number of turns N = 4, respectively [4]. Using Eq. (5.2) with the value of G of bulk cross-linked PMMA (0.29 GPa, see Appendix), the theoretical spring constant also is available in Fig. 5.3 (d). The error bars in vertical axis describe standard deviation of measurements for each spring. There is a gap between the experimental results and the theoretical curve, which derives from the size effect on G. To calculate G of the polymer nanowires, the size-dependent spring constant was substituted to the Eq. (5.2) with the parameters R = 2.5 μm and N = 4. Figure 5.3 (e) shows G as a function of r and an exponential fitting curve. The shear modulus G increases as decreasing in wire radius r. Note that relatively wider nanowires around 500 nm still exhibit a greater value of G compared to bulk systems.

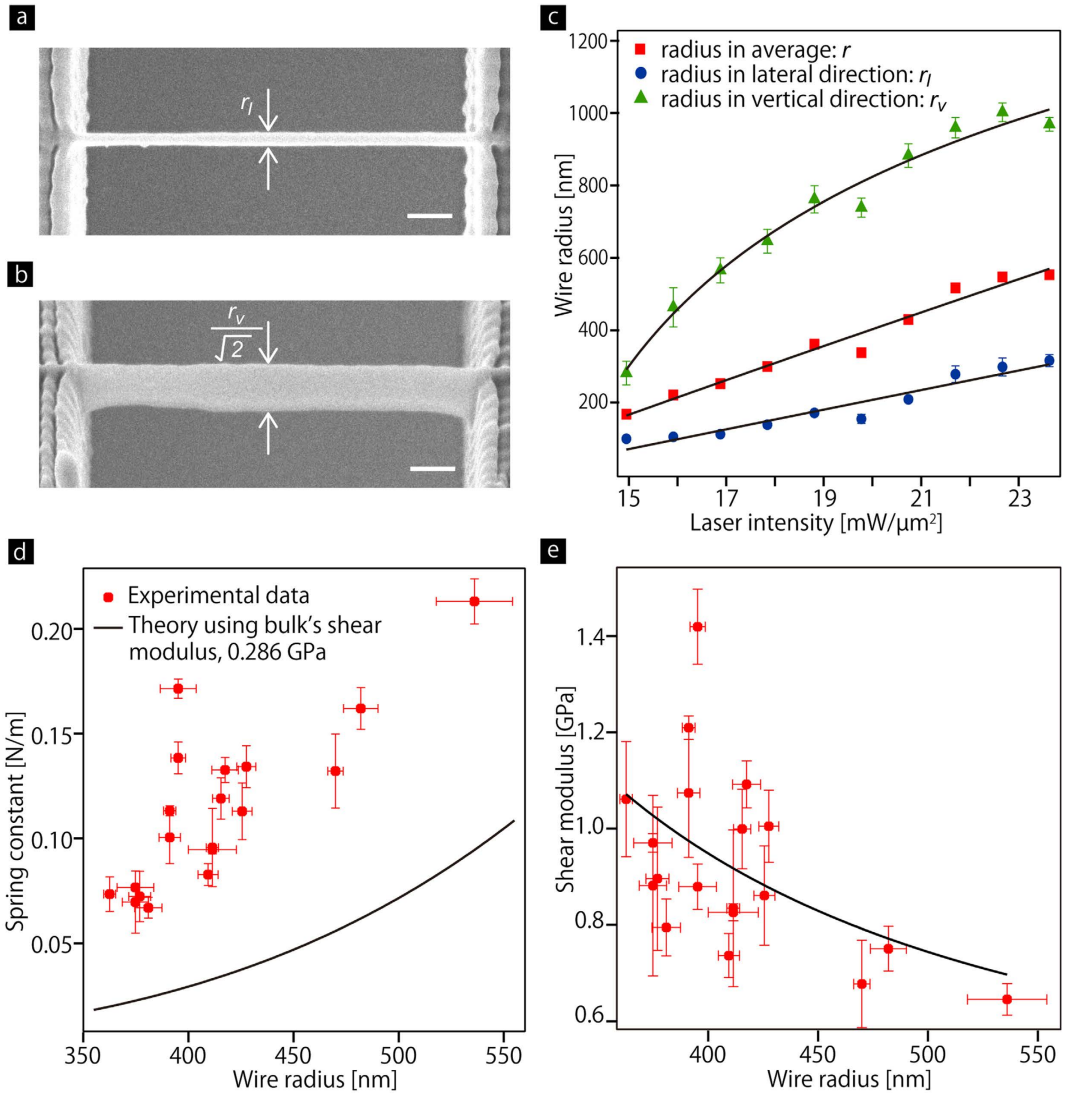

Figure 5.3| Size dependent elasticity of polymer nanosprings. (a), (b) SEM images of a nanowire from top (a) and tilted (45 degrees) views (b). Wire radii in lateral r_l and in vertical r_v are measured through SEM observation. Scale bars are 1 μm. (c) Wire radius r (red), r_l (blue), and r_v (green) as a function of laser intensity. (d) Spring constant k_s as a function of r measured (red symbols) and theory using bulk shear modulus (solid line). (e) G of polymer nanowires in coil springs as a function of r.

5.2 Raman analysis of polymer nanowires

Actually, the same trend of the size dependence has been found in many polymer nanowires other than PMMA: polystyrene [5], nylon 6.6 nanofibers [6], polyacrylonitrile nanofibers [7],

polypyrrole nanotubes [8], poly(2-acrylamido-2-methyl-1-propanesulfonic acid) nanofibers [9], and polyvinyl alcohol fibers [10]. There are several possible mechanisms of the size dependence: surface chain orientations [5], core/densely-packed-shell formation [10], and supramolecular structure formation [6].

As a possible factor for the size-dependence, I investigated alignment of polymer chain networks in cantilevered nanowires with different wire radii r using polarized micro-Raman spectroscopy (the details appear in Appendix). Polarized Raman spectra were measured with a different polarization angle θ between the polarization of the Raman excitation laser beam and the wire axis. Figure 5.4 (a) shows a Raman spectrum taken from a cantilevered nanowire whose wire radius r_1 is 356 nm (Fig. 5.4 (b)) with a polarization angle $\theta = 0°$. The liquid resin for the TPF includes four materials: methyl methacrylate (MMA) as a monomer, a cross-linker (CL), a photo-initiator (PI), and a photo-sensitizer (PS) (the detail described in Appendixes). Raman spectra from these materials are also shown in Appendixes. A peak at 545 cm^{-1} from PMMA can be assigned to C-C-C skeletal in-plane deformation oscillation mode [11-15]. I applied this peak for evaluation of molecular orientation in polymer wires. In fact, however, another broad peak from the CL overlaps on the peak of C-C-C skeletal oscillation of PMMA. I thus took average peak intensity of the peak between 535-

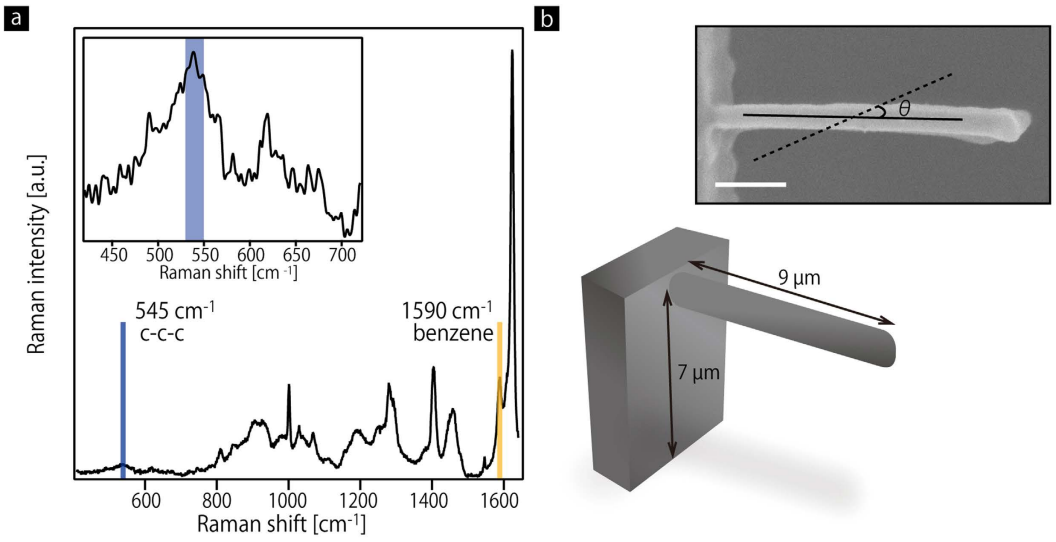

Figure 5.4| (a) Raman spectrum of a nanowire, whose wire radius is 356 nm. The inset to (a) is a magnified Raman spectrum around the peak at 545 cm^{-1}. (b) A cantilevered nanowire on the polymer wall. The inset to (b) is a top view of a cantilevered nanowire. θ is defined as an angle between the polarization of the Raman excitation laser beam and the wire axis. Scale bar is 1 µm.

555 cm^{-1} on behalf of Lorentzian fitting analysis at 545 cm^{-1}. Before this analysis of the peak at 545 cm^{-1}, this peak was normalized by a peak at 1590 cm^{-1} assigned to stretch oscillation mode of C=C in benzene circle which was included in the PI or the PS.

Polarization angular dependence of C-C-C skeletal peak

The peak intensity of C-C-C skeletal in-plane deformation oscillation mode in PMMA at 545 cm^{-1} has dependence on polarization angle of incident light. When PMMA C-C-C chains in polymer wires have particular orientations, the peak intensity should have particular polarization angular dependence. On the other hand, if not have particular orientations meaning that C-C-C chains have random orientation in the wires, the peak intensity should be independent on polarization angle. In this research, therefore, I investigated polarization angular dependence of the peak intensity from C-C-C skeletal oscillation mode. I also compared the polarization angular dependence along wire radii. The peak intensity from benzene circle at 1590 cm^{-1} I utilized to normalize the peak intensity from C-C-C chain in PMMA was independent on polarization angle.

As a result, a polarization angular dependence was appeared on the normalized peak intensity of PMMA C-C-C skeletal chain at 545 cm^{-1} when the radius of polymer wire was relatively small. On the other hand, the polarization angular dependence became to be relatively weak as the radius increased. Moreover, the polymer support wall as a bulk reference did not show polarization angular dependence on the peak intensity (Fig. 5.5).

This behavior of the polarization angular dependence can be described by a theoretical function shown as below [16]

$$I_{zz}(\theta) = I_0(I_{zz0} + I_{zz2}\cos 2\theta + I_{zz4}\cos 4\theta)\,. \qquad (5.3)$$

By fitting analysis of those experimental results shown in Fig. 5.5 with this theoretical function, information about molecular orientations in polymer wires can be obtained. The detail of the theoretical approach is described from the next section.

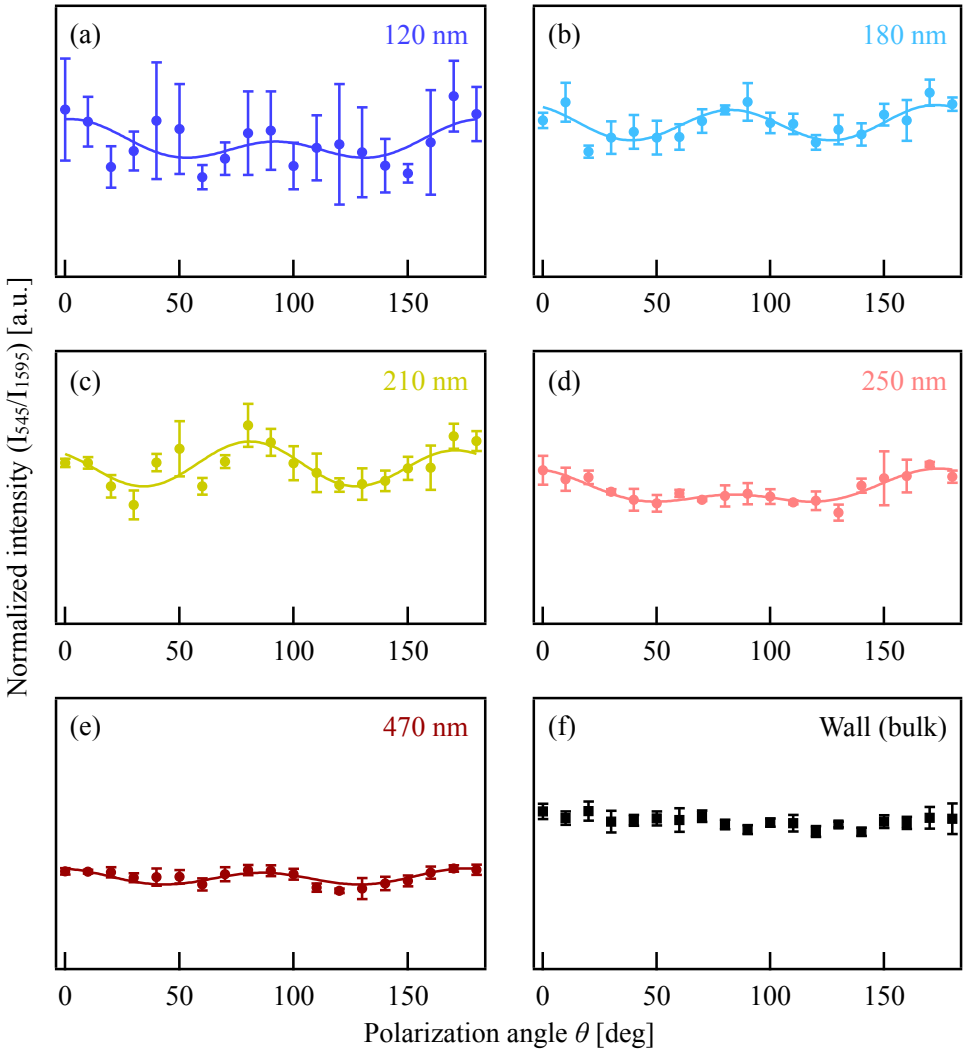

Figure 5.5| Normalized intensity of 532 cm^{-1} peak along polarization angle obtained from polymer nanowires with radii 120 nm (a), 180 nm (b), 210 nm (c), 250 nm (d), 470 nm (e), and wall (f) as a reference. Each plot and error bar describe average intensity and standard deviation of accumulation at 3 or 5 times. Results of fitting analysis are shown by solid lines. The range of vertical axis is fixed to 0.4.

5.3 Molecular orientation analysis of polymer nanowires

From here, derivation and physical meanings of the theoretical fitting function described as Eq. (5.3) will be explained. Basically, the theoretical function can be derived from coordinate transformation of second rank tensor.

Derivation of theoretical fitting function

Before deriving the theoretical function, I explain some assumptions regarding formation of molecules of polymer wires. (ⅰ) All the molecules should have homogeneous distribution in polymer wires [16,17]. (ⅱ) Orientation distribution of all the molecular structural units have orthotropic symmetry, uniaxial symmetry or isotropic, which means polymer wires are orthotropic, uniaxial with an axis to longitudinal direction, or isotropic. In this research, I assume that the structural units have uniaxial symmetrical orientation distribution or isotropic orientation distribution. This is because cross-linked PMMA is non-crystalline, hence the structural units are individual chain segments and surely have random orientation around longitudinal direction of the wires [16]. (ⅲ) Axes of Raman tensor should be coincident with axes of structural unit. In fact, the axes of Raman tensor do not necessarily coincide with those of structural unit. Therefore, another coordinate system for Raman tensor is needed against that for structural unit, and these two coordinate systems are related by Euler angle. However, in practice, most of the previous studies assume that the Raman tensor axes are coincident with the structural unit axes to reduce the number of parameters [16,18-20].

In the case of non-resonant Raman scattering (Placzek's approximation of polarizability), Raman tensor (or polarizability tensor) is regarded as second rank real symmetric tensor [21,22]. Therefore, such a second rank tensor $\boldsymbol{a}$ can be diagonalized with three unit eigenvectors $\boldsymbol{e}_{x'}$, $\boldsymbol{e}_{y'}$, $\boldsymbol{e}_{z'}$ which are orthogonal with each other, and three corresponding eigenvalues $\alpha_{x'}$, $\alpha_{y'}$, $\alpha_{z'}$ described as below,

$$\begin{aligned} \boldsymbol{a}\boldsymbol{e}_{x'} &= \alpha_{x'}\boldsymbol{e}_{x'} , \\ \boldsymbol{a}\boldsymbol{e}_{y'} &= \alpha_{y'}\boldsymbol{e}_{y'} , \\ \boldsymbol{a}\boldsymbol{e}_{z'} &= \alpha_{z'}\boldsymbol{e}_{z'} , \end{aligned} \tag{5.4}$$

$$\boldsymbol{E}^{-1}\boldsymbol{a}\boldsymbol{E} = \begin{bmatrix} \alpha_{x'} & 0 & 0 \\ 0 & \alpha_{y'} & 0 \\ 0 & 0 & \alpha_{z'} \end{bmatrix} , \tag{5.5}$$

here

$$\boldsymbol{a} = \begin{bmatrix} \alpha_{xx} & \alpha_{xy} & \alpha_{xz} \\ \alpha_{yx} & \alpha_{yy} & \alpha_{yz} \\ \alpha_{zx} & \alpha_{zy} & \alpha_{zz} \end{bmatrix} , \quad \alpha_{xy} = \alpha_{yx} , \quad \alpha_{xz} = \alpha_{zx} , \quad \alpha_{yz} = \alpha_{zy} , \tag{5.6}$$

$$\begin{aligned} \boldsymbol{E} &= [\boldsymbol{e}_{x'} \quad \boldsymbol{e}_{y'} \quad \boldsymbol{e}_{z'}] , \\ |\boldsymbol{e}_{x'}| &= |\boldsymbol{e}_{y'}| = |\boldsymbol{e}_{z'}| = 1 , \quad \boldsymbol{e}_{x'} \perp \boldsymbol{e}_{y'} \perp \boldsymbol{e}_{z'} . \end{aligned} \tag{5.7}$$

When these orthogonal eigenvectors are set as a rectangular coordinate system, the eigenvalues can be regarded as components of the diagonalized tensor along each axis. Furthermore, such a second rank tensor has orthotropic symmetry ($\alpha_{x'} \neq \alpha_{y'} \neq \alpha_{z'}$), uniaxial symmetry ($\alpha_{x'} = \alpha_{y'}, \alpha_{y'} \neq \alpha_{z'}$), or spherical symmetry ($\alpha_{x'} = \alpha_{y'} = \alpha_{z'}$).

From here, I explain the experimental system of polarized micro-Raman spectroscopy I used. As shown in Fig. 5.6, a rectangular coordinate system $x - y - z$ is defined. Longitudinal axis of polymer wire is located in $y - z$ plane. Furthermore, another rectangular coordinate system $x' - y' - z'$ which corresponds to three orthogonal eigenvectors $\boldsymbol{e}_{x'}$, $\boldsymbol{e}_{y'}$, $\boldsymbol{e}_{z'}$ of the second rank tensor $\boldsymbol{a}$ is defined with regard to the wire. $x' - y' - z'$ system can rotate around x' (x) axis and $0 - z'$ makes a variable angle θ with $0 - z'$ (Actually I rotated polarization of incident and scattered light, not the sample. However, this work is equivalent to sample rotation.). Incident light and scattered light pass along $0 - x'$ ($0 - x$) axis.

On an irradiated area of incident light, under the assumption (i) and (ii), the average of Raman tensor from a molecular oscillation can be described on $x' - y' - z'$ system as below,

$$\overline{\boldsymbol{a}_{x'-y'-z'}} = \begin{bmatrix} \overline{\alpha_{x'}} & 0 & 0 \\ 0 & \overline{\alpha_{y'}} & 0 \\ 0 & 0 & \overline{\alpha_{z'}} \end{bmatrix}, \tag{5.8}$$

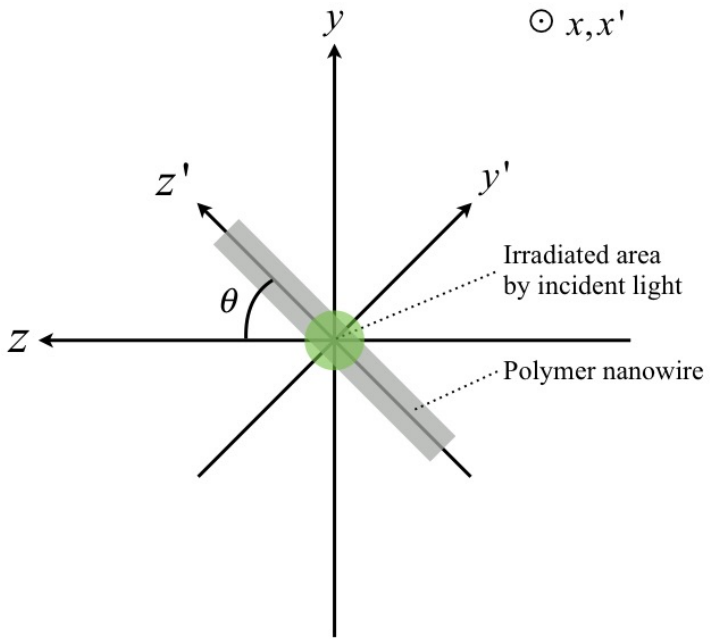

Figure 5.6| The definition of a rectangular coordinate system regarding polymer wires.

where $\overline{\alpha_{x'}}$ is equal to $\overline{\alpha_{y'}}$ because the wires are assumed to be uniaxial or isotropic. In this experimental system, the components of $x-y-z$ system regarding $\overline{\boldsymbol{a}_{x'-y'-z'}}$ is given with a rotation matrix around x' axis $\boldsymbol{R}_{x'}$ by the next equation

$$\begin{aligned}\overline{\boldsymbol{a}_{x-y-z}} &= \boldsymbol{R}_{x'}\overline{\boldsymbol{a}_{x'-y'-z'}}\boldsymbol{R}_{x'}^{T}\,,\\ \boldsymbol{R}_{x'} &= \begin{bmatrix}1 & 0 & 0\\ 0 & \cos\theta & -\sin\theta\\ 0 & \sin\theta & \cos\theta\end{bmatrix}.\end{aligned} \tag{5.9}$$

Equation (5.9) is a definition of coordinate transformation of second rank tensor. Here the amplitude of Raman scattering corresponding to components of the tensor α_{ij} is described as below,

$$E_i(\omega) = const\sum_{j=x}^{z}\alpha_{ij}\,E_j^0(\omega_0)\cos(\omega t+\delta)\,. \tag{5.10}$$

where $E_i(\omega)$ is the ith component of the electric vector of the scattered light, and $E_j^0(\omega_0)$ is the maximum value of the jth component of the electric vector of the incident light. It is assumed that Raman scattering is incoherent, so the phase angle δ is assumed to be random. From Eq. (6), Raman scattering intensity I_s is given by the following equation in consideration of the polarization directions of the incident and scattered light,

$$\begin{aligned}I_s &= I_0\left|\boldsymbol{l}_s\overline{\boldsymbol{a}_{x-y-z}}\boldsymbol{l}_i\right|^2,\\ \boldsymbol{l}_s &= \boldsymbol{l}_i = (0,0,1)\ \text{(polarized in } z \text{ axis)}\,,\end{aligned} \tag{5.11}$$

where I_0 is a constant depending on instrumental factors and the incident light intensity. $\boldsymbol{l}_s$ and $\boldsymbol{l}_i$ describe the polarization direction of scattered and incident light, and both directions take z axis in this experimental system. From Eq. (5.9) and Eq. (5.11), the theoretical fitting function can be derived as below

$$I_{zz}(\theta) = I_0(I_{zz0}+I_{zz2}\cos 2\theta + I_{zz4}\cos 4\theta)\,, \tag{5.3}$$

$$\begin{aligned}I_{zz0} &= \frac{1}{8}\left(3\overline{\alpha_{y'}}^2+\overline{\alpha_{y'}}\,\overline{\alpha_{z'}}+3\overline{\alpha_{z'}}^2\right),\\ I_{zz2} &= \frac{1}{2}\left(\overline{\alpha_{z'}}^2-\overline{\alpha_{y'}}^2\right),\\ I_{zz4} &= \frac{1}{8}\left(\overline{\alpha_{y'}}-\overline{\alpha_{z'}}\right)^2.\end{aligned} \tag{5.13}$$

Molecular orientation analysis of polymer nanowires

The theoretical fitting function was derived as Eq. (5.3) in the last section, and each parameter I_{zz0}, I_{zz2}, and I_{zz4} is related to components of the average of Raman tensor $\overline{\boldsymbol{a}_{x'-y'-z'}}$. I focused on the equation of I_{zz4}, and deformed it as below,

$$\overline{\alpha_{z'}} - \overline{\alpha_{y'}} = 2\sqrt{2I_{zz4}}\,, \quad \left(\because \overline{\alpha_{z'}} \geq \overline{\alpha_{y'}}\right). \tag{5.14}$$

Equation (5.14) describes the difference of magnitude between $\overline{\alpha_{y'}}$ and $\overline{\alpha_{z'}}$. When the right side is not 0, $\overline{\boldsymbol{a}_{x'-y'-z'}}$ is uniaxial symmetry because $\overline{\alpha_{x'}}$ is equal to $\overline{\alpha_{y'}}$. When the right side goes to 0, on the other hand, $\overline{\boldsymbol{a}_{x'-y'-z'}}$ is isotropic. When there is uniaxial molecular orientation distribution in polymer wires, in other words, the right side is not 0. Whereas if the molecules have random distribution, the right side is to 0.

By fitting analysis of the experimental results with Eq. (5.3) described in the last section, the value I_{zz4} in the case of the peak form C-C-C skeletal oscillation of PMMA was obtained per each polymer wire. The value $\overline{\alpha_{z'}} - \overline{\alpha_{y'}}$ in the case of the C-C-C skeletal oscillation of PMMA was thus compared along wire radius (Fig. 5.7). Looking down in Fig. 5.7, it can be found that the value $\overline{\alpha_{z'}} - \overline{\alpha_{y'}}$ tends to increase as wire radius decreases. In regard to the support wall as a bulk reference, fitting analysis was not able to be conducted correctly, because the peak intensity is almost independent on polarization angle as shown in Fig. 5.5.

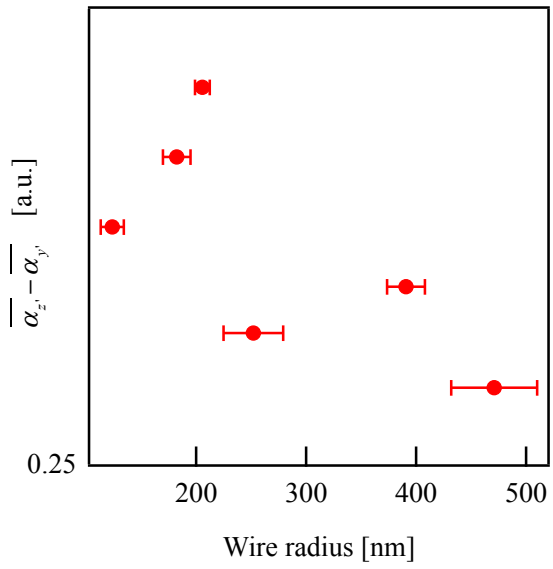

Figure 5.7| The value $\overline{\alpha_{z'}} - \overline{\alpha_{y'}}$ of the average of Raman tensor regarding C-C-C skeletal oscillation of PMMA against the radius of polymer wire.

The value $\overline{\alpha_{z'}} - \overline{\alpha_{y'}}$ in the case of the support wall, therefore, was not able to be obtained, but the value must be close to 0.

As a result, stronger uniaxial molecular orientation exists in the case of polymer wires with smaller radii. However, it should be noted that the value $\overline{\alpha_{z'}} - \overline{\alpha_{y'}}$ in the case of perfect uniaxial molecular orientation has not been known yet. Therefore, molecular orientation degree was not able to quantitatively obtained in this study.

Summary

Polymer nanosprings consist of polymer nanowires were formed by TPF. The nanosprings behaved as conventional spring. Force curve of the springs was measured with AFM cantilever. Spring constant and elastic modulus of the springs along radius of the nanowires. The elastic modulus depended on the wire radius. Molecular orientation of the nanowires was studied with polarized micro-Raman analysis. Intensity of a peak derived from C-C-C oscillation of PMMA had a dependence upon polarization angle. The wires with small radii had the dependence clearly. An analysis of averaged Raman tensor of the C-C-C oscillation indicated that stronger uniaxial molecular orientation existed in the wires with smaller radii. The molecular orientation can be one of origins of the size dependent physical properties of the nanosprings.

Appendixes

UV curable resin preparation

Methyl methacrylate (MMA) (Wako), cross-linker (DPE-6A) (Kyoeisha Chemical Co., Ltd.), photo-initiator (Benzil) (Wako), and photo-sensitizer (2-benzyl-2-(dimethylamino)-4′-morpholinobutyrophenon) (Aldrich) were mixed with a ratio of 49:49:1:1 wt% respectively (Tab. A5.1). The resin exhibited strong absorption in the UV region, but no absorption in the visible or NIR regions (Fig. A5.1).

Table A5.1| Chemical structure and recipe of materials.

	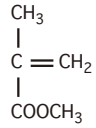 Monomer (MMA)	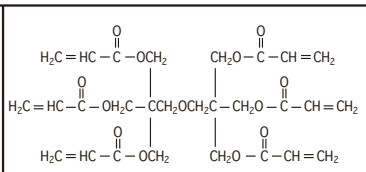 Cross-linker (DPE-6A)	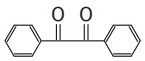 Photo-initiator (Benzil)	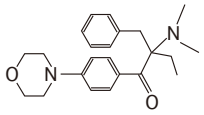 Photo-sensitizer
wt%	49	49	1	1

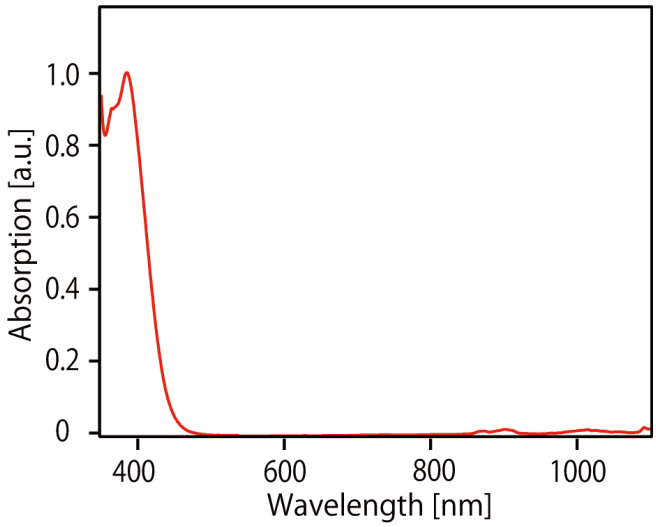

Figure A5.1| Absorption spectrum of prepared UV-curable resin.

Polymer nanospring fabrication

Figure A5.2 shows the optical setup for TPF. A Ti:sapphire femtosecond pulse laser (center wavelength 780 nm, pulse width 100 fs, repetition rate 82MHz) (Tsunami, Spectra-Physics) was used as the light source. The laser beam was focused through an oil-immersion objective lens (100×, NA 1.4) (Zeiss) onto the UV-curable resin casted on a glass substrate which was placed on a three dimensional piezoelectric stage. The stage moved the resin relative to the focus spot according to preprogrammed patterns. The typical laser intensity used in this study was 21 mW/μm^2, and the exposure time was kept constant at 4 msecs at each step. The wire widths were controlled by laser intensity. After the structures were fabricated, unsolidified

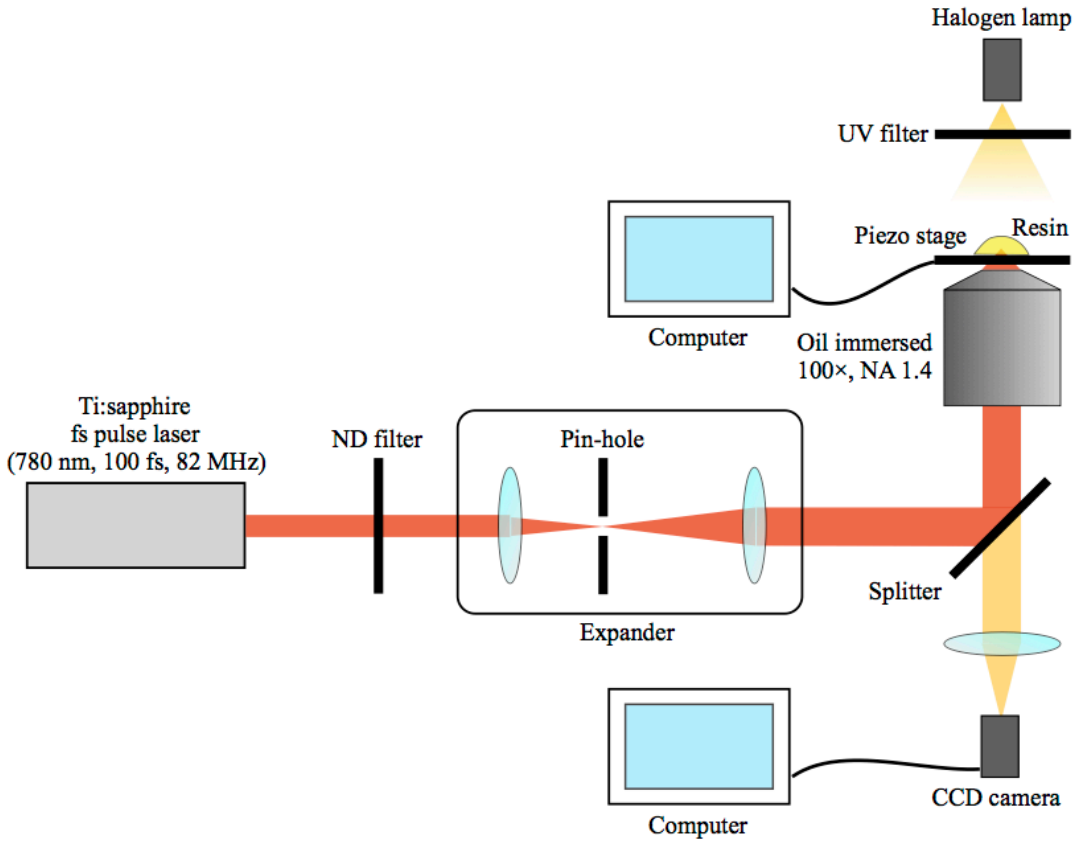

Figure A5.2| Optical setup of TPF.

resin was washed away using ethanol. The ethanol also was further replaced with supercritical CO_2 fluid and then dried in Supercritical Rinser & Dryer (SCRD4, Rexxam Co., Ltd.), preventing the structures from collapsing during the dry process. Ablation of additional supports was carried out using either a NIR femtosecond pulsed laser or a FIB (FB2200, Hitachi High-Tech).

Vertically standing coil springs were obtained as follows. The springs, which are the same dimensions as Fig. 5.1 (a), were fabricated on a polymer wall of 50μm length, 2.8μm thickness, and 15μm height. The wall was subsequently pushed down using a manipulator in FIB, and fixed onto the glass substrate by carbon deposition. The springs stably stood in vertical direction without any distortion and bend.

Compression with AFM

Compression tests on the vertically standing springs were conducted using an AFM (SPA-400, SII NanoTechnology Inc.) and an AFM cantilever (15 N/m, SI-DF20, SII NanoTechnology Inc.). The procedure of the compression test is shown in Fig. 5.2 (b). (i) the cantilever is initially set so that the cantilever was in contact with the bead of the spring. (ii) the cantilever compresses the spring but the cantilever tip does not contact the substrate. (iii) the tip contacts the glass substrate, and (iv) the cantilever returns to the initial position. The effective length of the cantilever, where the bead was in contact with the cantilever, was ~195 μm, while the total length of the cantilever was 225μm. This results in calibration of the spring constant to be 13 N/m. The cantilever moved downward for 1600 nm, exerting monotonically increasing compression on the spring, and then back to the initial position (Fig. 5.2 (b)). A force curve was recorded during the cycle with a measurement duration of a few seconds (Fig. 5.2 (c)).

Tensile tests on bulk sized cross-linked PMMA

Cross-linked PMMA films were prepared from the same UV-curable resin described above under UV lamp illumination. The tensile tests, which were conducted in Japan Chemical Innovation and Inspection Institute, measured the Young's modulus E and Poisson's ratio ν as 813 MPa and 0.42 respectively. Therefore, the bulk shear modulus G is obtained as 0.29 GPa with the next equation

$$G = \frac{E}{2(1+\nu)}. \tag{5.14}$$

This value was used for discussion.

Polarized micro-Raman analysis

A set of cantilevered nanowires with wire radius between 120 to 470 nm were fabricated on polymer walls. Alignment of polymer chain networks in the wires were investigated with polarized micro-Raman spectroscopy using a Raman microscope (Raman-11, Nanophoton Corp.). Figure A5.3 shows the optical setup of the Raman microscope. The excitation laser beam with a wavelength of 532 nm was linearly polarized with a polarizer, and focused onto the wires through an objective lens (100×, NA 0.9, Nikon). The polarization direction was

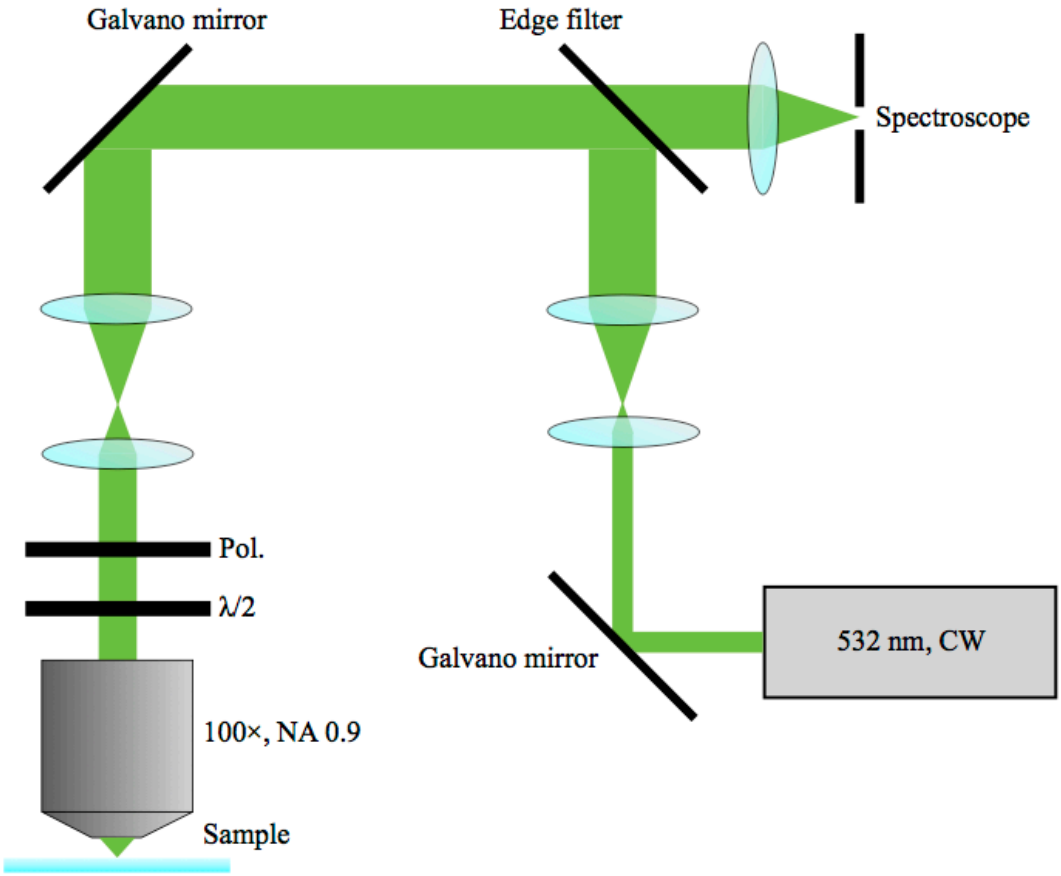

Figure A5.3| Optical setup of Polarized micro-Raman analysis.

controlled with a half-wave plate placed between the objective lens and the polarizer. Raman scattering was collected by the same objective lens, and the polarization direction was rotated to be the same direction as that of the incident light after passing through the half-wave plate. Background signal of each Raman spectrum was subtracted with fifth polynomial function fitting [23-25].

Raman spectrum of polymer materials

Raman spectra of materials for the UV curable resin is shown in Fig. A5.4. A peak of PMMA at 545 cm^{-1} is assigned to the C-C-C skeletal mode in PMMA, and a peak at 1595 cm^{-1} is assigned to stretch oscillation mode of C=C in benzene circle in the PI and PS [11-15].

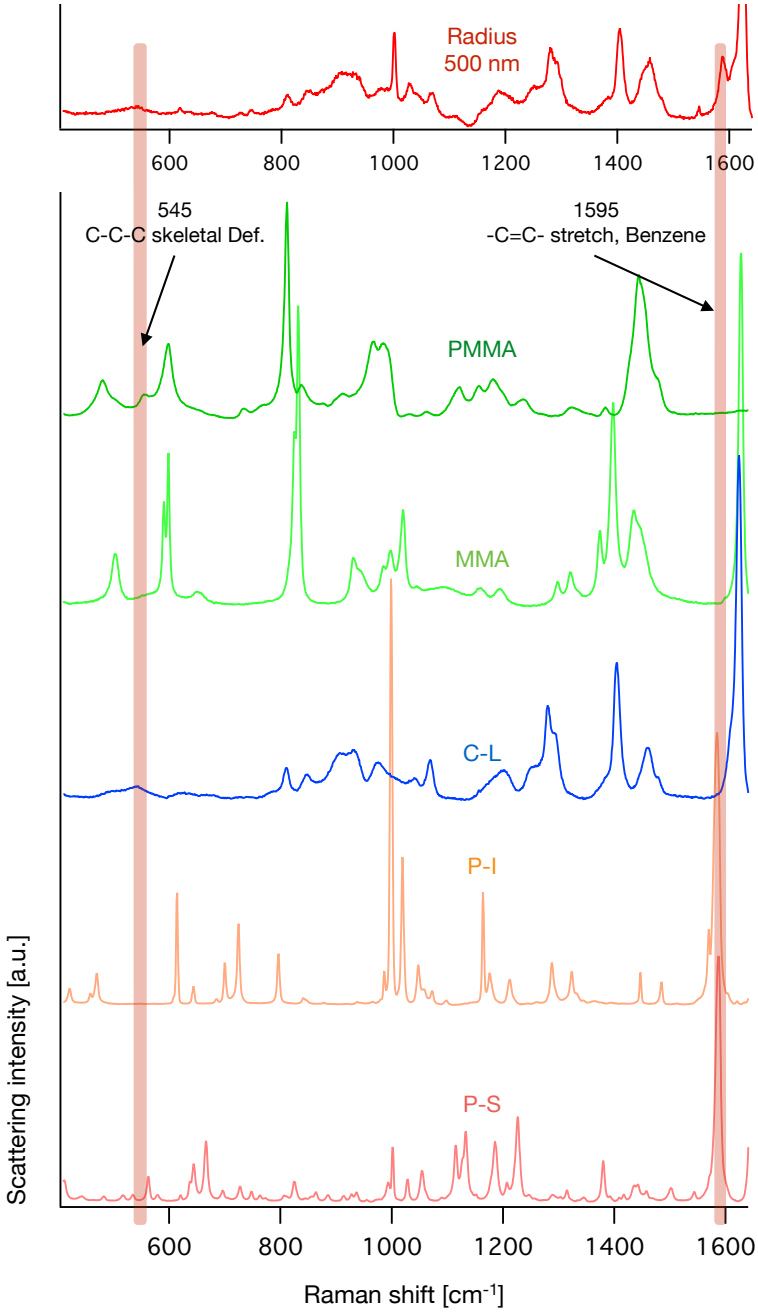

Figure A5.4| Raman spectrum of each material for UV curable resin: PMMA, MMA, CL, PI, and PS.

References

[1] S. Nakanishi, H. Yoshikawa, S. Shoji, Z. Sekkat, and S. Kawata, J. Phys. Chem. B **112**, 3586 (2008).

[2] S. Nakanishi, S. Shoji, S. Kawata, and H.-B. Sun, Appl. Phys. Lett. **91**, 063112 (2007).

[3] K.-S. Lee, D.-Y. Yang, S. H. Park, and R. H. Kim, Polym. Adv. Technol. **17**, 72 (2006).

[4] D. W. Van Krevelen and K. te Nijenhuis, *Properties of Polymers* (Elsevier, 2009).

[5] Y. Ji, C. Li, G. Wang, J. Koo, S. Ge, B. Li, J. Jiang, B. Herzberg, T. Klein, S. Chen, J. C. Sokolov, and M. H. Rafailovich, Europhys. Lett. **84**, 56002 (2008).

[6] A. Arinstein, M. Burman, O. Gendelman, and E. Zussman, Nature Nanotech **2**, 59 (2007).

[7] D. Papkov, Y. Zou, M. N. Andalib, A. Goponenko, S. Z. D. Cheng, and Y. A. Dzenis, ACS Nano **7**, 3324 (2013).

[8] S. Cuenot, S. Demoustier-Champagne, and B. Nysten, Phys. Rev. Lett. **85**, 1690 (2000).

[9] M. K. Shin, S. I. Kim, S. J. Kim, S.-K. Kim, H. Lee, and G. M. Spinks, Appl. Phys. Lett. **89**, 231929 (2006).

[10] U. Stachewicz, R. J. Bailey, W. Wang, and A. H. Barber, Polymer **53**, 5132 (2012).

[11] C. Huang, J. T. Mason, and I. W. Levin, *Raman Spectroscopic Study of Saturated Mixed-Chain Phosphatidylcholine Multilamellar Dispersions* (Biochemistry, 1983).

[12] S. George, *Infrared and Raman Characteristic Group Frequencies-Tables and Charts* (Wiley, 2001).

[13] H. Kuzmany, Phys. Stat. Sol. (B) **97**, 521 (1980).

[14] H. A. Willis, V. J. I. Zichy, and P. J. Hendra, Polymer **10**, 737 (1969).

[15] J. S. Stephens, D. B. Chase, and J. F. Rabolt, Macromolecules **37**, 877 (2004).

[16] J. Purvis and D. I. Bower, Polymer **15**, 645 (1974).

[17] D. I. Bower, J. Polym. Sci. B Polym. Phys. **10**, 2135 (1972).

[18] M. Tanaka and R. J. Young, J Mater Sci **41**, 963 (2006).

[19] R.-J. Roe, J. Appl. Phys. **36**, 2024 (1965).

[20] C. Sourisseau, Chem. Rev. **104**, 3851 (2004).

[21] 濱口宏夫, 平川暁子, ラマン分光法 (学会出版センター, 東京, 1988).

[22] 今野豊彦, 物質の対称性と群論 (共立出版, 東京, 2001).

[23] J. Zhao, H. Lui, D. I. McLean, and H. Zeng, Appl Spectrosc **61**, 1225 (2007).

[24] C. A. Lieber and A. Mahadevan-Jansen, Appl Spectrosc **57**, 1363 (2003).

[25] 浜田啓作, ラマン散乱による細胞内分子分析イメージング, 2008.

Conclusion

Through this thesis, I discussed a bottom-up optical 3D production of silver nanodendrites as a subwavelength structure and possibility of them as a metamaterial. I also discussed a top-down optical 3D nanofabrication which was contrasting to the bottom-up method, and physical properties of polymer nanostructures fabricated by the top-down method.

In Chapter 1, I defined a metamaterial as an assembly of intendedly produced subwavelength structures which simultaneously respond with both electric and magnetic fields. Then, I provided an overview of the metamaterials: principles, a brief history, applications, and production methods especially with bottom-up approaches. After that, I explained possibility of the silver nanodendrites as a bottom-up metamaterial operating in broad areas around optical region. I also showed some precedents of the metamaterials with dendritic structures.

In Chapter 2, I explained a principle of dendrite growth based on statistical thermodynamics. Inhomogeneity of concentration gradient of solutes is the essence for the dendrite growth. Balance between diffusion of the solutes and velocity of crystal growth is important for the concentration gradient formation. I also provided an overview of precedents regarding silver nanodendrites. Then, I described a method of optical 3D growth of the silver nanodendrites via plasmon resonance heating which I developed. I also described nondestructive extraction of the structure of the nanodendrites with results. I also discussed structural characteristics among experimental parameters: laser power, interfacial tension and viscosity of solvents, cooling temperature, and concentration of silver ion and a reductant. These parameters were able to be optimized for the dendrite growth.

In Chapter 3, I discussed electromagnetic responses of silver nanodendrites with FDTD analysis. A model of the dendrites showed a peak in infrared region on its scattering spectrum. Parts composed of adjacent branches of the dendrites were able to act as SRRs, allowing them to have electromagnetic induction at the peak. Permittivity, permeability, and refractive index originated from a nanodendrite model were discussed. Negative permeability and negative refractive index appeared. Appearance of the peak differed among geometry

parameters of the model. Also, electromagnetic response of the model differed with incident directions.

In Chapter 4, I introduced a top-down fabrication method of 3D nanostructures via two-photon absorption; TPF. The TPF realizes arbitrary 3D structural fabrication with spatial resolution beyond diffraction limit because of two-photon absorption and existence of polymerization threshold. Therefore, The TPF can be applied in various fields which need nanofabrication including metamaterials.

In Chapter 5, I discussed physical properties of polymer nanostructures formed by TPF. Elastic modulus of polymer nanosprings composed of polymer nanosprings, which was measured by an AFM cantilever, showed size dependency. The elastic modulus increased against decrease of wire radius. To prove origins of this size dependency, I conducted molecular orientation evaluation of the polymer nanowires by polarized micro-Raman analysis. This analysis showed that uniaxial molecular orientation along length direction of the wires tended to occur on thin wires. The result indicates that the molecular orientation correlates the size dependency of the elastic modulus.

As future perspectives, enlarging the area of nanostructure growth is important. In-plane area can be expanded as UV illumination area enlarges. To increase the height, stacking layers of nanostructures is effective. Besides vertical growth of the nanostructures, lateral growth also occurs which leads to collision of adjacent structures. To prevent the collision, decreasing the density of nano-seeds is effective. Resin is an alternative matrix other than agarose for silver nanostructure growth. By using other metals, such as gold or copper, for nanostructure growth, operating frequency range shifts. It surely is interesting to analyze electromagnetic responses of the dendrites with higher levels of branches. FDTD analysis with different polarization and another incident direction is needed to deeply understand the electromagnetic responses of the dendrites. Note that actual silver nanodendrites grow randomly. Only perpendicular growth from the substrate never exists. Therefore, it is great if simulations taking account of the randomness of structure and growth direction of the dendrites are available. It is great if refractive index of grown silver nanodendrites can be measured.

Silver nanodendrites have two benefits on metamaterials: bottom-up production via crystal growth and capability of wide area operation around optical region originated from fractal. Production and wide frequency operation are main problems of the metamaterials. Approaching to these issues is the significance of this research. Through this research, I

achieved fabrication of three-dimensional silver nanostructures with self-growing. I also discovered that the nanostructures could be applied to the metamaterials. I hope this research contributes to realization of bulk metamaterials with three-dimensional subwavelength structures.

List of publications

Original papers

1. Natsuo Taguchi, Nobuyuki Takeyasu, and Satoshi Kawata, "Extraction of three-dimensional silver nanostructures with supercritical fluid", Appl. Phys. Express, Vol. 11, 025201 (2018).
2. Nobuyuki Takeyasu, Natsuo Taguchi, Naoki Nishimura, Bo-Han Cheng, and Satoshi Kawata, "Plasmonic growth of patterned metamaterials with fractal geometry", APL Photonics, Vol. 1, pp. 050801 (2016).
3. Shota Ushiba, Kyoko Masui, Natsuo Taguchi, Tomoki Hamano, Satoshi Kawata, and Satoru Shoji, "Size dependent nanomechanics of coil spring shaped polymer nanowires", Sci. Rep., Vol. 5**,** 17152 (2015).

International conferences

1. Shota Ushiba, Kyoko Masui, Natsuo Taguchi, Satoru Shoji, and Satoshi Kawata, "Nanomechanics of polymer nanocoil springs", Nanophotonics in Asia 2015, Osaka, Japan, December 2015.
2. Natsuo Taguchi, Satoru Shoji, Shota Ushiba, Kyoko Masui, and Satoshi Kawata, "Molecular orientation in polymer wires with nanosized radii unveiled by polarized micro-Raman spectroscopy", IONS-Asia 5 Hokkaido, Hokkaido, Japan, September 2014.
3. Natsuo Taguchi, Satoru Shoji, Shota Ushiba, Kyoko Masui, and Satoshi Kawata, "Molecular orientation in polymer wires with nanosized radii unveiled by polarized micro-Raman spectroscopy", Asia Student Photonics Conference 2014, Kolkata, India, July 2014.
4. Natsuo Taguchi, Satoru Shoji, Shota Ushiba, Kyoko Masui, and Satoshi Kawata, "Raman micro-spectroscopy on cross-linked polymer nanowires formed by 2-photon fabrication", SPIE Photonics West, Paper 8974-2, San Francisco, USA, February 2014.
5. Natsuo Taguchi, Satoru Shoji, Shota Ushiba, Kyoko Masui, and Satoshi Kawata, "3D micro sculptures made of single wall carbon nanotube/polymer composites fabricated by two photon polymerization lithography", Asia Student Photonics Conference 2013, Osaka, Japan, July 2013.

6. Shota Ushiba, Satoru Shoji, Kyoko Masui, Natsuo Taguchi, and Satoshi Kawata, “Superresolution 3D micro/nano fabrication by means of nonlinear optical effect”, Taiwan-Japan Workshop on Nano Devices, P-6, Taiwan, March 2013.
7. Shota Ushiba, Natsuo Taguchi, Kyoko Masui, Satoru Shoji, and Satoshi Kawata, “Coil springs made of polymer nanowires fabricated by two photon polymerization”, Asia Student Photonics Conference 2012, Osaka, Japan, September 2012.

Domestic conferences

1. 田口夏生、武安伸幸、河田聡、“光成長する銀ナノデンドライト：成長環境の最適化とメタマテリアルへの応用”、第 64 回応用物理学会春季学術講演会、15p-F202-9、神奈川、2017 年 3 月。
2. 田口夏生、庄司暁、牛場翔太、増井恭子、河田聡、“2 光子加工作製された架橋ポリマーナノワイヤーの偏光顕微ラマン分光による分子配向評価”、平成 25 年度第 3 回講演会 関西からのフォトニクスとカーボン研究イノベーション、大阪、2014 年 2 月。
3. 田口夏生、庄司暁、牛場翔太、河田聡、“２光子加工法で作製した架橋 PMMA ナノワイヤーの顕微ラマン分光”、第 60 回応用物理学会春季学術講演、29p-D2-7、神奈川、2013 年 3 月。
4. 庄司暁、牛場翔太、増井恭子、田口夏生、河田聡、“架橋 PMMA ナノワイヤーコイルばねの２光子加工作製と力学特性”、第 60 回応用物理学会春季学術講演会、30p-D2-7、神奈川、2013 年 3 月。

Abstract

Nanofabrication nowadays has been utilized in every field of science and technology without doubt. Mainstreams of nanofabrication such as lithography with light, e-beam, ion-beam etc., however, are basically methods of two-dimensional fabrication. Two-photon fabrication (TPF) realizes three-dimensional (3D) nanostructure fabrication by utilizing light with high intensity. Two-photon process of materials excited by focusing pulse lasers is applied. Arbitrary 3D nanostructures with subwavelength resolution can be formed with polymers, metals etc. by TPF. On the other hand, TPF is categorized in top-down approaches of nanofabrication. The top-down approaches are unsuitable for mass fabrication of nanostructures. Bottom-up approaches such as crystal growth are effective for the mass fabrication of the structures. In this thesis, I discuss a bottom-up optical fabrication approach of 3D nanostructures. I also discuss potentials of the 3D nanostructures for metamaterials. The metamaterials are subwavelength 3D structures interacting with electromagnetic field, realizing refractive index control. Furthermore, I discuss TPF as a top-down fabrication approach of 3D nanostructures and size dependent physical properties of the fabricated 3D nanostructures.

A method of bottom-up optical fabrication of tree-like silver nanostructures (silver nanodendrites) was developed. Heat generation due to plasmon resonance of silver nanoparticles (seeds) excited by UV laser was utilized for reinforcement of silver ion reduction around the seeds. Seeds were chemically fixed onto glass substrates, and the silver nanodendrites grew from the seeds. Growth of the silver nanodendrites requires concentration gradient of reduced silver atom. Interfacial tension and viscosity of solvents, temperature, power of the laser, and concentrations of silver ion and a reductant are important parameters to form the concentration gradient. Shape differences of silver crystals among those parameters thus were studied. Although the nanodendrites grew in three dimensions, structures were deformed or destructed when they were extracted from solution. The use of supercritical carbon dioxide fluid was discussed for non-destructive extraction of the nanodendrites. Another experiment was done for nanostructure growth inside agarose gel as a matrix. The silver nanodendrites were immobilized without damage in agarose skeleton-network.

Electromagnetic field responses of silver nanodendrites were studied with finite-difference time-domain method to evaluate potentials as metamaterials. Scattering spectra of the silver nanodendrites were analyzed. Magnetic responses on oscillation modes at peaks of the scattering spectra were confirmed. Peak shifts of the scattering spectra among parameters of geometry of the silver nanodendrites and incident angle were studied. Permittivity, permeability, and refractive index of the silver nanodendrites were discussed.

Elasticity and molecular orientation of polymer 3D nanostructures formed by TPF were evaluated. Polymer nanosprings, which consist of polymer wires with radii of several hundred nm, were prepared. Size dependent elasticity of the polymer nanosprings along wire radii was evaluated with spring constants measured by an atomic force microscope. Size dependent molecular orientation of polymer nanowires along wire radii also was evaluated by polarized micro-Raman spectroscopy. Correlations of the size dependent characteristics between the elasticity and the molecular orientation were discussed.

Acknowledgement

This research was done under supports by the Laboratory for Scientific Instrumentation and Engineering (LaSIE), Department of Applied Physics, Osaka University. Here, I express my deep appreciation.

Prof. Satoshi Kawata for his supremely courteous supports as the supervisor of this research. Catching up with him was really tough for me. However, I was not able to be what I am today without his guides. His way of thinking was always essential and witty, which made me realized the core of things. I was able to realize fun and hardship of creation. The most valuable thing was that I was able to be aware of how I should be as a member of society. Moreover, he gave me a number of opportunities for growing such as student chapter activities. The experience of my doctoral course will definitely one of the biggest foundation for the future. I could not thank to him enough.

Prof. Junichi Takahara for his warm supports for writing this dissertation and preparing for the defense as the chief examiner, even I was originally not in his group. Through his feedbacks and advices, I was able to dramatically improve the dissertation and the presentation for the defense. I appreciate his effective supports.

Prof. Nobuyuki Takeyasu (Okayama University) as the main advisor of this research. I was able to discuss all aspects regarding this research with him many a time: from the significance to technical details, and deepen insights and understanding of this research. I received a number of valuable advices from him. Without his supports, it was impossible for me to proceed this research.

Prof. Katsumasa Fujita for courteous supports regarding the whole of this research. Although the research group was different, I was able to learn many things and enjoy my research life through discussions and daily conversations with him. He also gave me a lot of meaningful feedbacks as one of the vise-examiners of this dissertation, which greatly improved this dissertation.

Dr. Takuo Tanaka (RIKEN) and Prof. Tsuyoshi Sekitani for meaningful discussions and advices as the vise-examiners of this dissertation. Although I spent one more year, I was able to greatly proceed this research.

Prof. Atsushi Taguchi and Dr. Zhiqiang Zhang for courteous supports to my research activity. I was able to freely consult various issues regarding research execution, and received many effective solutions. Thanks to their supports, I was able to smoothly carry out experiments and simulations.

Prof. Satoru Shoji (The University of Electro-Communications) as the supervisor of my research in master course, and Dr.[2] Kyoko Masui and Dr. Shota Ushiba as the seniors who helped and supported me the most. I was inspired by their attitude of enjoying science freely. When I started research in LaSIE from master course and did not know anything, they courteously guided me everything of research from scratch. I learned various important things such as the ways of research and story building of report and presentation. Discussion with them was always interesting and insightful, and their advices were always effective.

Prof. Prabhat Verma, Prof. Yuika Saito (Gakushuin University), Prof. Yasushi Inoue, Prof. Hidekazu Ishitobi, and Prof. Nicolas I. Smith for valuable discussions and feedbacks through activities in LaSIE such as paper review and progress review. I was able to deepen my insight of science, and improve my presentation skill through their supports.

My seniors in Fujita group: Dr. Kentaro Mochizuki, Dr. Kozue Watanabe, Dr. Yasuo Yonemaru, Dr. Kazuki Bando, Dr. Hiroyuki Kawagoe, and the seniors in LaSIE: Dr. Toshihiro Mino, Prof. Takayuki Umakoshi, Yoshiro Ohashi, Dr. Yosuke Ueba, and Dr. Masashi Miyata. Thanks to them, I was able to have a fulfilling research life. I was motivated by their sincere and intense attitude for science. I enjoyed various daily activities including student chapter.

My classmates: Dr. Ryosuke Oketani, Haruka Suda, Dr. Aya Hashimoto, Dr. Yuki Inoue, Yun Zheng, Dr. Shu Jiang, Naoki Nishimura, and Ryuji Shimomura. Because of them, I was able to reach a Ph.D. Here, I just thank to all of them. Especially, I greatly referred Nishimura's master thesis when I started to do this research, and comprehended important points. Zheng courteously supported my life in doctoral course. Through the life, I was able to mature as a person. I hope her everything goes well in the future.

My colleagues in M group: Daigo Oue, Yuta Kaseyama, Ken Ito, Akihiro Okuno, and Dr. Susan Skelton. Through daily meetings and conversation with them, I was able to know and share various knowledges of science. Their fundamental questions made me deepen understanding of my research.

My juniors in Fujita group and LaSIE: Yau Chuen Yiu, Toshiki Kubo, Sho Nitta, Kentaro Nishida, Kota Koike, Masahiro Yagyu, Wataru Kamo, Den Ka, Taeho Lee, Yuta Kunihisa, Kumiko Uegaki, Kana Kobayashi, Mai Higuchi, Jumpei Hirohata, Yusuke Nagasaki, So Fujiwara, Takumasa Sekiya, Takayuki Kobayashi, Ryo Kato, and Shun Igarashi. I was able to enjoy my research life thanks to their supports on every aspect. They also greatly supported me when I carried out student chapter activities.

Secretaries: Nobune Toba, Kana Takagi, Haruna Tagashira, Yumiko Fujioka, and Tomomi Sakai, and staffs of Photonics Advanced Research Center (PARC): Tae Otono and Saori Kurata. Their warm supports made my research life comfortable and easy.

I also express my appreciation to all the members in Fujita group, Verma group, Inoue group, Takahara group, Smith group, PARC, student chapters of OSA/SPIE/JSAP, Kagakusha-ishin-juku, and friends I met in Japan and abroad. Thanks to all of them, I was able to grew greatly as a scientist and as a person.

For Yusuke Mizuno, Shun Kinoshita, Chie Yamato, and Akira Yamasaki. Talking with them with delicious foods and alcohols was a good relaxation of my research life.

研究生活の費用を拠出し、精神的に支えてくれた両親に、心から感謝します。

Finally, I thank to Jesus.
From now on, I will give and contribute.

Natsuo Taguchi
Osaka, December 2017